Available online at www.sciencedirect.com
SCIENCE DIRECT®
Physics Reports 392 (2004) 321–424
PHYSICS REPORTS
www.elsevier.com/locate/physrep

Effects of noise in excitable systems

B. Lindner[a], J. García-Ojalvo[b,c], A. Neiman[d,e], L. Schimansky-Geier[e,f,*]

[a] *Physics Department, University of Ottawa, 150 Louis Pasteur, Ottawa, Ont., Canada K1N 6N5*
[b] *Departament de Física i Enginyeria Nuclear, Universitat Politècnica de Catalunya, Colom 11, E-08222 Terrassa, Spain*
[c] *Center for Applied Mathematics, Cornell University, Ithaca, NY 14853, USA*
[d] *Center for Neurodynamics. University of Missouri at St. Louis, St. Louis, MO 63121, USA*
[e] *Department of Physics and Astronomy, Ohio University, Athens, OH 45701, USA*
[f] *Institut für Physik, Humboldt–Universität zu Berlin, Newtonstr. 15, D-124889 Berlin, Germany*

Accepted 8 October 2003
editor: I. Procaccia

Abstract

We review the behavior of theoretical models of excitable systems driven by Gaussian white noise. We focus mainly on those general properties of such systems that are due to noise, and present several applications of our findings in biophysics and lasers.

As prototypes of excitable stochastic dynamics we consider the FitzHugh–Nagumo and the leaky integrate-and-fire model, as well as cellular automata and phase models. In these systems, taken as individual units or as networks of globally or locally coupled elements, we study various phenomena due to noise, such as noise-induced oscillations, stochastic resonance, stochastic synchronization, noise-induced phase transitions and noise-induced pulse and spiral dynamics.

Our approach is based on stochastic differential equations and their corresponding Fokker–Planck equations, treated by both analytical calculations and/or numerical simulations. We calculate and/or measure the rate and diffusion coefficient of the excitation process, as well as spectral quantities like power spectra and degree of coherence. Combined with a multiparametric bifurcation analysis of the corresponding cumulant equations, these approaches provide a comprehensive picture of the multifaceted dynamical behaviour of noisy excitable systems.

PACS: 05.10.−a; 05.10.Gg; 05.40.Ca; 05.40.Jc; 05.45.Xt; 42.65.Sf; 42.55.Px; 82.20.Pm; 82.40.Ck; 83.10.Mj; 87.16.Ac; 87.16.Uv

* Corresponding author. Applied Stochastic Processes, Institute of Physics, Newtonstrasse 15, D-12489 Berlin, Germany. Tel.: +49-2093-7624; fax: +49-2093-7638.
E-mail addresses: lindner.benjamin@science.uottawa.ca (B. Lindner), jordi.g.ojalvo@upc.es (J. García-Ojalvo), neiman@ohio.edu (A. Neiman), alsg@physik.hu-berlin.de (L. Schimansky-Geier).

0370-1573/$ - see front matter
doi:10.1016/j.physrep.2003.10.015

Keywords: Stochastic dynamics; Excitable dynamics; FitzHugh–Nagumo system; Leaky integrate-and-fire model; Active phase rotators; Stochastic cellular automata; Firing rate; Coefficient of variation; Spike count diffusion; Brownian motion in periodic potentials; Phase synchronization; Noise induced phase transition; Noisy pattern formation; Laser dynamics; Ion-channel clusters

Contents

1. Introduction

Excitability is observed in a wide range of natural systems. A list of examples includes lasers, chemical reactions, ion channels, neural systems, cardiovascular tissues and climate dynamics, to mention only the most important fields of research [1–16]. Common to all excitable systems is the existence of a "rest" state, an "excited" (or "firing") state, and a "refractory" (or "recovery") state. If unperturbed, the system resides in the rest state; small perturbations result only in a small-amplitude linear response of the system (cf. Fig. 1a). For a sufficiently strong perturbation, however, the system can leave the rest state, going through the firing and refractory states before it comes back to rest again (Fig. 1b and c). This response is strongly nonlinear and accompanied by a large excursion of the system's variables through phase space, which corresponds to a spike. The system is refractory after such a spike, which means that it takes a certain recovery time before another excitation can evoke a second spike (Fig. 1d and e).

There is a rich literature on *deterministic* (i.e. noiseless) excitable systems. Excitability in deterministic systems is well understood, especially in applications to chemistry and biology, where several excellent reviews and books exist [1–4]. Excitability is a typical dynamic phenomenon of systems far from equilibrium [17]. Such nonequilibrium situations can be maintained by several conditions, depending on the physical system under consideration. In the case of lasers it is the external energy pumping, in the case of chemical reactions it is a permanent flow of matter, and in neurons it is associated with a potential difference across the cell membrane originated by ion pumps and, hence, by ATPase.

In addition to being out of equilibrium, excitable systems require an additional feedback mechanism. In case of neurons, for instance, this feedback is mediated by ion channels with a nonlinear voltage-dependent conductance. In the seminal paper by Hodgkin and Huxley [18], it was shown that this excitability mechanism (for the specific case of the giant squid axon) can be very

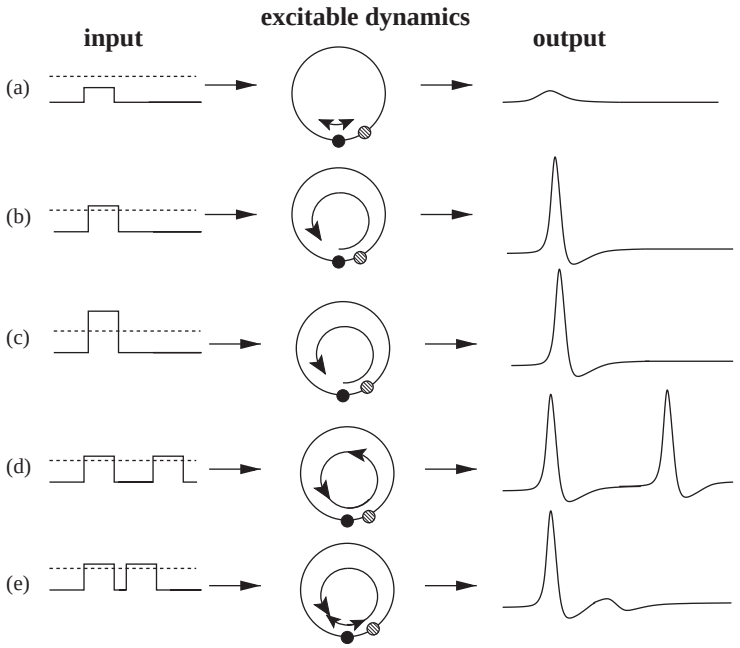

Fig. 1. Features of excitability: different kinds of inputs (left column) cause different kinds of responses (right column) of the excitable dynamics (middle column). (a) An input below threshold (dashed line) results in a small amplitude motion around the system's stable state (full circle in middle-column plot); (b) an input exceeding the threshold leads to an escape over a quasi-separatrix or an unstable point (empty circle in middle-column plot) and to a large-amplitude excursion of the system's variables (spike); (c) further increase of the input's amplitude does not change the shape of the spike significantly; (d) two well separated input pulses result in two spikes; (d) if the pulses are too close, the system does not respond noticeably to the second perturbation because of refractory effects.

successfully modeled by a four-dimensional nonlinear dynamical system. As shown later by FitzHugh [19] and others, two nonlinear autonomous differential equations suffice for a qualitative study and understanding of excitability. In such a two-dimensional system, self-sustained oscillations beyond a Hopf or a homoclinic bifurcation are possible [20,21]. We note that models of excitability can be even simpler than two-dimensional one. For instance, one-dimensional systems with a reset rule (e.g. integrate-and-fire models) and phase models are frequently used to study specific aspects of excitability.

Besides having an interesting temporal behavior, when a large number of excitable systems are coupled to one another they exhibit a rich variety of interesting spatio-temporal behaviors, depending on the strength and topology of the coupling between the excitable elements. Phenomena such as pulse and spiral wave propagation, scroll waves, localized spots, periodic patterns in space and/or in time, and spatio-temporal chaos have been reported in different areas of physics, chemistry and the life sciences [22–24]. Other topics of interest are the effects of spatial inhomogeneity, of feedback, and of time-dependent driving. In perspective, one of the most remarkable properties of excitable systems is their ability to synchronize, both among themselves or to external periodic (or more complex) signals [25–36].

Noise is inevitably present in systems far from equilibrium [37–39]. In excitable systems, the origins of noise can be as diverse as the physical basis of excitability itself. In chemical reactions noise results from finite-size effects, in lasers quantum fluctuations are the dominant noise source, while in climate dynamics changes due to the annual and other cycles might be looked upon as rapid fluctuations on the time scales that are relevant for long-term dynamics (e.g. ice ages). In neurons, noise arises from many different sources, such as the quasi-random release of neurotransmitter by the synapses, the random switching of ion channels, and most importantly random synaptic input from other neurons. Besides internal noise sources, it is also common practice nowadays to apply noise externally in experiments, and to include external noise sources in theoretical models. In this way, important parameters like intensity and correlation time of the noise can be controlled and hence the role of noise can be systematically explored.

Our review is dedicated to the problem of how noise affects excitable systems. Most of this review is based on work by the authors; we refer to work of many other groups in this field. However, due to the broadness of this topic and its applicability in many different fields of science, we cannot ensure completeness of the cited literature. Our presentation summarizes the main effects of random perturbations in single excitable systems, in globally connected networks of such systems and in reaction–diffusion systems. We focus on the distinct characteristics of stochastic models in comparison to the deterministic ones. Such characteristics are found in two situations:

- In the first case, noise acts inhomogeneously on different states of the system. This is a situation found quite often in nonlinear dynamics. Processes in different regions of the state space are amplified or dampened by noise in different ways. Hence, the characteristic time scales of the associated motion in phase space becomes noise-dependent, and the dynamics is modified depending on the intensity of the perturbations. A simple and evident example for such a situation is a system driven by multiplicative noise [141].
- The second case is connected with the existence of thresholds, separatrices and saddles in dynamical systems. When noise comes into play, these unstable barriers can be passed with finite probability. In contrast to the first case, here purely noise-induced processes are excited which are absent in the deterministic model. The new controlling time scale grows unbounded if noise vanishes. Pure additive noise is sufficient to model these processes [142].

Here we review both situations in various models. We show how phenomena encountered in deterministic systems such as synchronization, resonant behavior, and pattern formation are influenced and modified by noise. For this purpose, we elaborate methods and define measures to quantify phenomena in a broad class of stochastic excitable systems and media.

One of the most remarkable effects discovered in stochastic excitable dynamics is the occurrence of oscillatory behavior due to noise perturbations [40–46]. In other words, excitable systems driven by noise possess a noise-induced eigenfrequency, and thus are able to exhibit stochastic oscillations that correspond to a so-called stochastic limit cycle in phase space. These noise-sustained oscillations are often accompanied by the phenomenon of coherence resonance (CR) [47,148,48–51], which corresponds to the existence of an optimal noise intensity at which noise-induced oscillations are most coherent. Coherence resonance can be found in neural models including the FitzHugh–Nagumo model [52–55], the leaky integrate-and-fire model [56,57], phase models [58,59], the Plant and Hindmarsh–Rose models [60,61], the Morris–Lecar model [62] and the Hodgkin-Huxley model

[63–67], as well as models of neural networks [68,69]. Outside the neuronal context, CR was observed in laser models [70,71], in models of excitable biomembranes [72] and in climate models [16]. Applications of this effect can be found in Refs. [73,74,319,75–77]. It is worth mentioning that CR is not only encountered in excitable systems but also in other systems that are close to a dynamical bifurcation (for diverse examples, see [50,78–99]). Other studies have focused on the role of possible correlations of the noise (neglected in most of the above work), using e.g. colored Ornstein–Uhlenbeck [100] or harmonic noise [101] as a source of fluctuations in the FitzHugh–Nagumo and the Hindmarsh–Rose models, respectively.

Noise also affects strongly the transmission of periodic signals by nonlinear systems. As it was shown for bistable and simple threshold devices [102,103], the transmission of subthreshold signals is enhanced by the presence of non-vanishing noise (stochastic resonance). Due to the existence of a threshold or quasi-separatrix in excitable dynamics, the same effect is found in excitable systems [104–108] (see also [109] for further references). However, bistable or simple threshold devices amplify low-frequency periodic signals the strongest, whereas the excitable system displays optimal transmission at a finite frequency. The latter effect can be understood as a classic resonance with respect to the frequency of stochastic oscillations, i.e. with the noise-induced eigenfrequency [110–112]. The nonmonotonous dependence of transmission measures (e.g. the spectral power amplification) on either noise intensity and driving frequency has also been termed stochastic double resonance [113].

Noise influences and enhances synchronization and pattern formation in excitable systems. The degree of coherence in networks and regions of inhomogeneous states in reaction–diffusion systems is a nontrivial function of the noise parameters, i.e. noise intensity and noise correlation time. As a consequence, synchronization and pattern formation can be controlled by noise. For example, adding noise can be beneficial to attain synchronization among coupled excitable systems [114–122]. Noise can play the role of control parameter changing the frequencies of coupled excitable elements [123–125]. Synchronization of large ensembles of biological objects with excitable dynamics, such as ion channels and heart cells, have been investigated by stochastic methods [126–129]. Besides synchronization, other effects can be observed in locally coupled systems under pattern-forming conditions, where noise strongly influences wave propagation, spiral dynamics and pacemaking [130–140] (for reviews see also [141,142]). CR-like effects in spatially extended systems have also been studied [143–147].

Experimental studies have shown the important role of noise in many bistable systems (for reviews see [109,142] and references therein). There is also substantial experimental evidence of nontrivial noise-induced phenomena in excitable systems. The first experimental observation of coherence resonance was reported by means of electronic circuits [149–152], laser diodes [153–156], excitable chemical reactions [157–164], optically trapped atoms [165], and the cat's neural system [166]. Stochastic resonance has been observed experimentally in several types of peripheral mechanoreceptors, including mechanoreceptive hairs on the tail fan of crayfish when sensing weak water waves [167,168], mechanoreceptors on the tail of crickets when sensing vibrations and air currents [169], tactile receptors in the skin of rats [170], auditory hair cells of frogs [171], neocortical pyramidal neurons [172], during human perception [173], in mammalian neuronal networks [174] and in the human brain's visual processing area [175]. Stochastic resonance was also found in chemical reactions [176–180] and on the molecular level of ion channels [181], as well as in feeding behavior of the paddlefish [182–184]. Paddlefish electroreceptors also demonstrate noise-induced bursting and

synchronization regimes [185]. Noise-induced synchronization has also been shown in networks of electronic circuits [186] and chemical reactions [187–189]. Noise-sustained waves have been observed in the light-sensitive Belousov–Zhabotinsky reaction [190,191] and in cultures of glial cell networks [192,193]. Enhanced wave propagation and spiral dynamics, and generation of pacemakers by noise have also been reported [194–199].

The main message of this review is that a moderate amount of noise leads to enhanced order in excitable systems, manifesting itself in a nearly periodic spiking of single excitable systems, enhancement of synchronized oscillations in coupled systems, and noise-induced stability of spatial patterns in reaction–diffusion systems.

This paper is organized as follows. In the next section we explain the main features of excitability in different fields and introduce the models we shall work with. Section 3 reviews coherence and stochastic resonance in homogeneous excitable systems and how these effects can be characterized, focusing in particular on analytical methods. In Section 4 we study two applications, clusters of ion channels and laser systems. Turning to spatially extended systems, we first explore in Sections 5 and 6 the effects of noise in globally coupled excitable units. Finally, Noise-induced spatio-temporal structures such as spirals and propagating pulses are discussed in Section 7.

2. Excitability and minimal models

2.1. Models of excitability

As mentioned above, excitable systems possess a single stable rest state. This rest state can be simply an equilibrium (or fixed) point or a small-amplitude (subthreshold) limit cycle. The large excursions of the system's variables produced by strong enough perturbations of this state are often called spikes, and their occurrence is referred to as a firing. This terminology is borrowed from neuroscience—the electrical discharge of a nerve cell's membrane potential is commonly called an action potential or a firing of a spike.

One may look upon the generation of a spike as a one-way passage through a sequence of stable and unstable states. The *resting* state, being dynamically stable, can be left only by a sufficiently strong external activation. The *firing* and the following *refractory* states are unstable in the sense that the system escapes from them even in the absence of external perturbations. While the escape from the resting state strongly depends on the external input, the passage through the firing and refractory states possesses only a weak dependence on the external driving.

This dynamical behavior can be modeled in several ways. A suitable autonomous system must have at least two variables obeying a nonlinear dynamics, since the occurrence of stable spiking trajectories requires a dynamical system close to a bifurcation toward an oscillatory (limit-cycle) regime. Models exhibiting this property were first proposed for neuronal spike generation. In the FitzHugh–Nagumo [19,200] and the Morris–Lecar model [201], a fast variable (in this case the membrane voltage) is driven by an external input above a threshold level. After that it keeps growing and approaching a second metastable state due to a nonlinear dynamics: the system is excited, i.e. in the firing state. Another variable, the recovery variable, acting on a slower time scale, destabilizes the excited state of the fast voltage variable, bringing it back to its rest state by means of a negative feedback. Afterwards, the initial state is reestablished when the recovery variable relaxes. In the

two-dimensional phase plane, the entire process is seen as a round-trip or large-amplitude excursion that does not depend much on the details of the external input. If that input is a stationary noise, the excursions will repeatedly occur at random times; in other words, the state point of the system moves along a *stochastic limit cycle*.

A closer look at the two-dimensional models reveals two different kinds of excitability known for a long time in neuroscience [5,25], namely type I and type II excitability. The underlying mathematical difference between these two regimes is the bifurcation from quiescent to repetitive firing that occurs if a control parameter is increased:

(i) Type I neurons, like those described by the Morris–Lecar model, undergo a saddle-node bifurcation; close to the bifurcation point their spike rate can become arbitrarily low.
(ii) Type II neurons, like those described by the FitzHugh–Nagumo system, show a supercritical Hopf bifurcation that is associated with the onset of a finite-frequency oscillation.

A phenomenological distinction between the two types of excitability in a number of real neurons was already made by Hodgkin [202] in 1948.

Multidimensional, in particular two-dimensional, nonlinear models are hard to tackle analytically. Therefore, it is advantageous to describe excitable dynamics by means of more tractable one-dimensional systems. There are three ways to model excitable behavior:

- First, one can impose a threshold-and-reset condition on a one-dimensional dynamics. In this case, crossing a given threshold value is associated with a spike and the reset is explicitly realized by a reset rule instead of a second dynamical variable. The leaky integrate-and-fire neuron is a common example for this kind of system. A linear dynamics is often used for the state variable.
- Second, the motion along a stochastic limit cycle may be described by a single phase variable obeying a periodic dynamics. These approaches ignore deviations transverse to the limit cycle. The Adler equation, described below, is the simplest model for type I excitability [5] and a prominent example of this approach.
- Third, one may explicitly model three discrete states which are visited by the system consecutively, and prescribe probabilities with which these states are left at a given time.

In the rest of this section we introduce the FitzHugh–Nagumo model as an example for a two-dimensional system, and the leaky integrate-and-fire neuron and the noisy Adler equation as one-dimensional systems. Discrete dynamics are introduced in Section 5. We focus on the excitable regime of these models and discuss how they are affected by white-noise driving and additional periodic forcing. For various spatially extended versions of these models, see Sections 5–7.

2.2. The FitzHugh–Nagumo dynamics

The FitzHugh–Nagumo (FN) model [19,200], also called the Van der Pol–Bonhoeffer model [203–205], is a simple example of a two-dimensional excitable dynamics. It was proposed in Refs. [19,200] as a simplification of the famous model by Hodgkin and Huxley [18]. It describes (qualitatively rather than quantitatively) the response of a type II excitable nerve membrane to external current stimuli. Important features, also found in experiments on real neurons, are the inclusion of a recovery

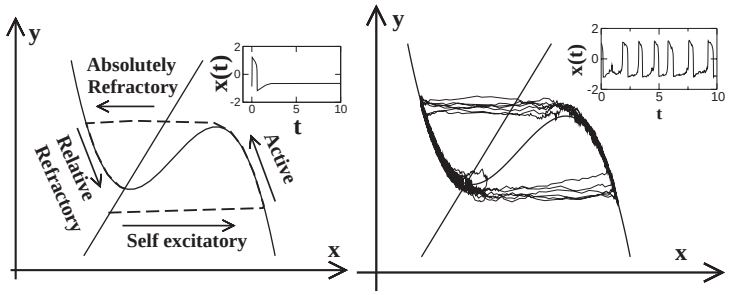

Fig. 2. Left: nullclines of the FN system (thin solid lines) and a deterministic trajectory ($D = 0, s(t) \equiv 0$) in the phase plane. Particular states of the system are indicated following Ref. [19]. The inset shows the time evolution of the x variable. Right: a stochastic realization for $D = 0.1$, $s(t) \equiv 0$. Noise-driven excursions through the phase plane imply a spike train in the variable $x(t)$, resembling the spontaneous electric activity of a neuron. For both panels $b = 0.6$, $\gamma = 1.5$, $\epsilon_t = 0.01$ and Eq. (2) with $a = 1$ were used.

mechanism and the existence of different refractory states after excitation, as well as states of enhanced and depressed excitability depending on the time course of external stimulation.

In its one-dimensional spatially extended version, with diffusion in the fast voltage variable, the model displays traveling pulses, thus reproducing the propagation of an action potential (spike) down the neuronal axon [206]. These equations also found applications in early theoretical investigations of the Belousov–Zhabotinsky reaction [207], explaining spiral dynamics and scroll waves in two and three spatial dimensions, respectively.

A stochastic version of the FitzHugh–Nagumo model was studied for the first time by Treutlein and Schulten [40]. There the notion of noise-induced limit cycles was introduced in this model (for the occurrence of this phenomenon in other models see [41,42]). Driving the FN model by white noise and a (periodic or aperiodic) signal became popular during the 1990s in the context of stochastic resonance [110,104,105,208–211,106,212–215]. Furthermore, its spatially extended version has also attracted much attention as a noisy excitable medium in the last decade (see, e.g. [192,118,143,144]).

One common representation of the stochastic FN model is given by

$$\epsilon_t \dot{x} = f(x) - y \ ,$$

$$\dot{y} = \gamma x - \beta y + b - s(t) + \sqrt{2D}\xi(t) \ . \tag{1}$$

The two non-dimensional variables x and y are a voltage-like and a recovery-like variable, or—in the terminology of physical chemistry and semiconductor physics—an activator and an inhibitor variable, respectively. $s(t)$ is a periodic signal and $\sqrt{2D}\xi(t)$ is a white Gaussian noise with intensity D. In neuronal models, the time scale ratio ϵ_t is much smaller than one ($\epsilon_t \approx 10^{-2}$), implying that $x(t)$ is the fast and $y(t)$ is the slow variable. The nonlinear function $f(x)$ (shaped like an inverted N, as shown in Fig. 2) is one of the nullclines of the deterministic system; a common choice for this function is

$$f(x) = x - ax^3 \ , \tag{2}$$

where the parameter a is either 1 or 1/3. In the excitable regime of the FN model this nullcline intersects only once with the linear nullcline of the y dynamics ($y = \gamma x + b$ in the absence of signal and

noise, see again Fig. 2). The intersection point is a stable fixed point on the left branch of the cubic nullcline—the resting state of the system. Sufficiently strong perturbations (either in x or in y) result in a far reaching excursion in phase space along the right branch of $f(x)$ ("firing" of the neuron), and back along the upper left branch ("neuronal refractory state") into the rest state. In Fig. 2 (left) this trajectory is shown for the deterministic system started at an appropriate initial condition, caused, for instance by an external stimulation. Following FitzHugh [19], the aforementioned physiological states of the neuron are indicated. In $x(t)$ (inset of Fig. 2, left) the excursion in the phase plane appears as a spike.

Even in the deterministic and autonomous case ($D=0,\ s(t)\equiv 0$), the FN model possesses a rather complex bifurcation behavior with multiple fixed points and limit cycles. The parameters b and γ determine the position of the fixed points; for $a=1$ a single fixed point is realized if $(\gamma-1)^3/27+b^2/4>0$. For our purposes, we focus on this regime with small ϵ_t. If $4\epsilon_t\gamma>(\epsilon_t+1-3x_0^2)$, this fixed point at x_0 possesses complex eigenvalues and undergoes an Andronov–Hopf bifurcation when $3x_0^2+\epsilon_t-1$ changes sign. In the case of small $\epsilon_t\ll 1$, the parameter region of complex eigenvalues is rather small. Additionally, the generated limit cycle approaches quickly large amplitudes after the Hopf-bifurcation. The limit cycle runs along the stable branches of the cubic nullcline and switches between the branches at the local minimum and maximum of $f(x)$.

The excitation process that was in the deterministic case due to the initial condition, occurs repeatedly if noise is present ($D>0$). This is demonstrated in Fig. 2 (right), which shows a stochastic trajectory in phase space and the corresponding time series $x(t)$ (inset). The random force occasionally kicks the phase point out of the vicinity of the stable fixed point towards the region labeled "self-excitatory" in Fig. 2 (left). The sequence of action potentials resembles the spontaneous activity of a neuron.

When an additional signal is present ($s(t)=\epsilon\cos(\omega t)$), the occurrence of spikes will be correlated with this signal. In the case of a weak signal, addressed in this review, this correlation is only seen at finite noise since the weak signal alone cannot evoke a spike. In the presence of noise, the signal just increases the probability to fire at certain instances. For instance, a very slow signal can be seen just as a modification of the y nullcline with $b\to b-s(t)$ shifting the fixed point away from (if $s(t)<0$) or closer to (if $s(t)>0$) the effective threshold. Consequently, firing is more likely at the maxima of the signal.

We note that the stochastic term in Eq. (1) stands for channel noise and other intrinsic noise sources. Several researchers have also considered a noisy driving in the dynamics of the voltage variable [104,209,106] (which would represent synaptic input from other neurons) or a stochastic forcing in both equations [40,43,216]. Regarding the periodic signal, we note that situations where it acts directly on the dynamics of the voltage-like variable (or on both variables) can be also described by Eq. (1) by means of a linear transformation in y (see for instance [110]).

During an action potential, the voltage variable of a real neuron varies between roughly -80 mV and 20 mV, while its duration is about 1 or 2 ms [13]. These numbers allow one to estimate the factors by which the variables x and t have to be rescaled in order to compare simulation results of the FN model to a spike train of a specific neuron. Other parameters like γ and b have to be determined by fitting procedures that use the shape of the action potential and/or the input–output relation (firing rate vs parameter b). The input noise levels can be inferred from the variability of the voltage variable or of the spike train. The latter depends also substantially on the other parameters (γ,ϵ_t and b), though; hence, any reasonable parameter fit to real data remains a nontrivial task.

Since different versions of the model Eq. (1) are used in the literature, some further technical details are indicated. In most studies the parameter β is either 1 or 0. The latter choice considerably simplifies the analysis, since in that case only one fixed point is possible in all regimes. This model exhibits a Hopf bifurcation to limit cycles. With $\beta = 1$, the dynamics also allows to study the transition to bistable behavior. Besides these options, other choices of Eq. (2) have been made. For instance, the Barkley model [217], defined by a function $f = f(x, y)$ polynomial in x and y, was proposed for computational convenience (see Section 7). Another computationally efficient version that is also more tractable analytically is given by a piecewise linear function $f(x, y)$ [218–220] such as

$$f(x) = \begin{cases} -1 - x & \text{if } x \leqslant -1/2\ , \\ x & \text{if } -1/2 < x < 1/2\ , \\ +1 - x & \text{if } x \geqslant 1/2\ . \end{cases} \tag{3}$$

Unless stated otherwise, we use in what follows the symmetric cubic function Eq. (2) with $a = 1$ and $\beta = 1$, leaving b, γ and D as free parameters.

Although the FN model is easy to simulate on a computer, there is no general way to tackle the problem analytically and to determine measures that characterize coherence and stochastic resonance. Even the solution of the stationary Fokker–Planck equation corresponding to the Langevin equations Eq. (1) is an unsolved problem, not to mention second order statistics that quantify the regularity of spiking (see Section 3).

2.3. Stationary probability density of the FN dynamics

One way to deal with stochastic systems is to describe them by their stationary probability density [17,221,222]. For model (1) in the time-independent long-time limit $t - t_0 \to \infty$, the transition probability density $P(x, y, t|x_0, y_0, t_0)$ obeys the Fokker–Planck equation (FPE) [142]

$$\frac{\partial P}{\partial t} = -\frac{1}{\epsilon_t}\frac{\partial}{\partial x}(x - x^3 - y)P - \frac{\partial}{\partial y}(\gamma x - y + b)P + D\frac{\partial^2 P}{\partial y^2}\ . \tag{4}$$

In particular, we have taken $a = 1$, $\beta = 1$ and $s(t) \equiv 0$. Due to ergodicity and stationarity of the FN dynamics, the density $P(x, t|x_0, t_0)$ tends to a unique stationary solution $P^0(x, y)$ of Eq. (4). This is found if one solves this equation with vanishing left-hand-side, i.e. $\partial P^0/\partial t = 0$.

We note that, with the exception of a singular parameter combination, the stationary FPE is not tractable analytically [223,216]. The FN with additive noise is an example where additive noise changes strongly the stationary density and, correspondingly, the dynamical behavior. These phenomena have been called noise-induced transitions, either due to state-dependent noise [224], breaking of detailed balance [223] or colored noise [225,226].

In the 1980s Treutlein and Schulten [40] first simulated the stationary probability density of a FN model for parameters which correspond to a deterministic excitable regime with a single stable fixed point. They found crater-like shapes of the density, corresponding to an oscillatory behavior for medium-sized noise intensities and strong time-scale separation $\epsilon \to 0$. Trajectories of the dynamics switch between the rest and excited state along a circular path, with well defined positions where the transitions takes place.

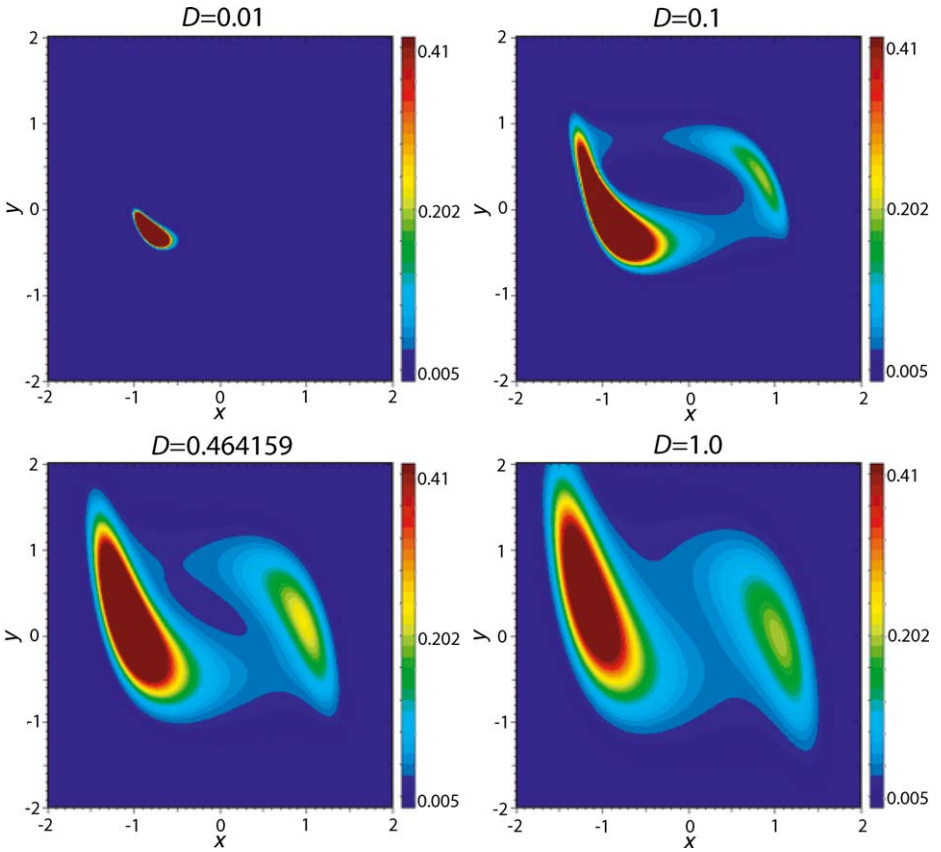

Fig. 3. Stationary probability density for different noise intensities D with fixed parameters $\epsilon_t = 0.1$, $b = 1.4$ and $\gamma = 2$ [229].

One would associate such craters to stochastic excitation above limit cycles of self-sustained oscillations, rather than to a regime with a single fixed point. Therefore, this noise-induced states were called stochastic limit cycles. Approximate expressions of the stationary densities with a qualitatively similar shape were found in [41,42,223,227,228].

Recently, we have numerically integrated the stationary Fokker–Planck equation for the FN with additive noise [229], making use of different integration schemes such as finite elements [230] and Runge–Kutta methods [231].

First, we fix the parameters $\epsilon_t = 0.1$, $\gamma = 2$, and $b = 1.4$, and vary D. The single fixed point of the deterministic nullclines corresponding to the rest position is located at $x \simeq -0.83$, and it is a stable node. Plots of the probability density are shown in Fig. 3. For small noise intensity ($D = 0.01$), the probability density is concentrated around the fixed point. For increasing noise ($D = 0.1$), a second maximum emerges, together with a "hole" in the middle of the distribution. The crater around the hole is completed by two separated regions with larger probability, where transitions between the two branches take place. At a further increase of the noise intensity ($D = 0.46$) the "hole" disappears, and we find only two separate peaks above the rest and excited portions. Transitions between the two peaks occur from a broad region of inhibitor values centered with maximal probability around $y = 0$.

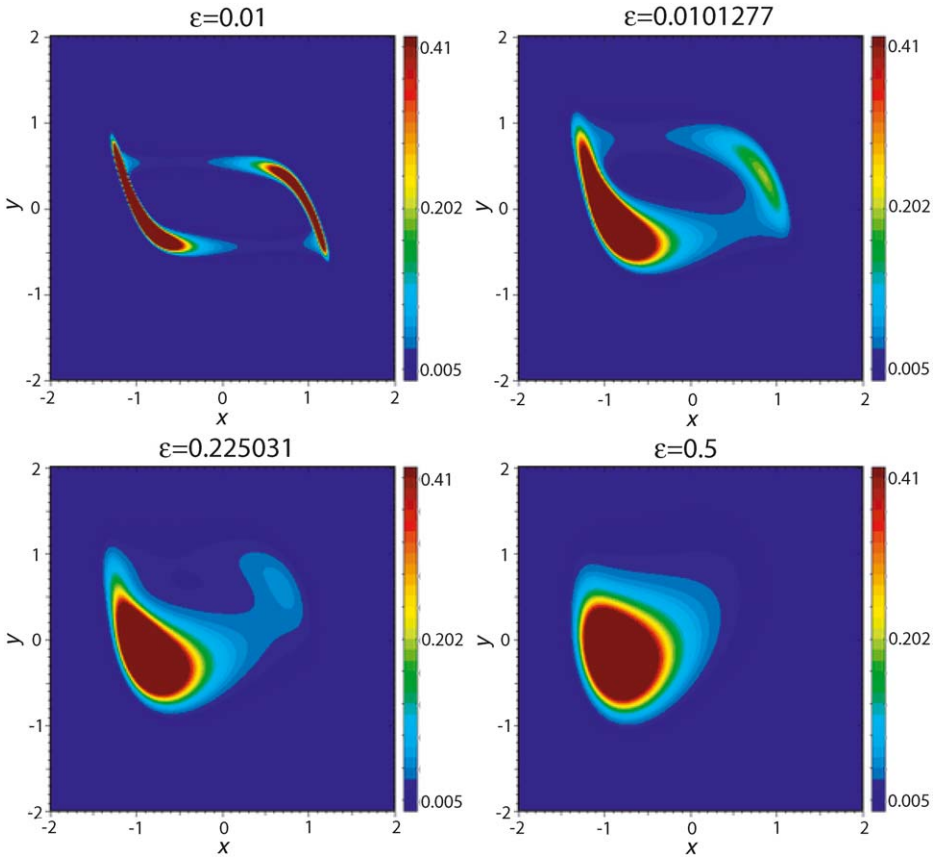

Fig. 4. The stationary probability distribution for different time scale ratios ϵ_t with fixed parameters $\gamma = 2$, $b = 1.4$ and noise intensity $D = 0.1$ [229].

Another sequence of the stationary density is shown in Fig. 4 for varying time scale ratio ϵ_t. Note that ϵ_t does not change the location of the nullclines in the deterministic model, but obviously affects the system's dynamics. At small ϵ_t values, we find the crater enclosing the hole, two peaks along the nullcline $y(x) = x - x^3$ and two separated saddles above the most probable position for transitions. In between this crater, a minimum forms. When we increase $\epsilon_t \approx 0.101$ the region of the maximum near the deterministically stable fixed point grows and the excited one shrinks. For further increase of $\epsilon_t \approx 0.225$, the minimum and the saddle point at higher y values vanish. For values $\epsilon_t \approx 0.5$, the second saddle point and the maximum of the excited branch merge and disappear, and a single peaked density centered at x values higher than the rest state remains.

2.4. The leaky integrate-and-fire model

One of simpler models that captures features of excitability is the leaky integrate-and-fire (LIF) model used in many computational studies in theoretical neurobiology [232–235,13]. Its stochastic version has been studied in the presence of periodic forcing by means of approximations

[236–240], sophisticated numerical methods [113,241,242], and exact analytical solutions [112,243–245]. Furthermore, there are numerous simulation studies of the model (see for instance [246,247], among many others).

The LIF model is a one-dimensional model with reset, where the voltage across the nerve membrane *in between excitations* is determined by a simple current balance

$$C\dot{V} = -V/R_{\mathrm{leak}} + I(t) \ , \tag{5}$$

where C is the capacitance of the cell membrane and R_{leak} is a leak resistance. The input current $I(t)$ is usually chosen to be a superposition of a white Gaussian noise and a periodic signal. As in the case of the FitzHugh–Nagumo model, the noise stands either for intrinsic fluctuations or for the superposition of many external synaptic input spike trains. The signal corresponds either to an externally applied current, or to the time dependent mean of the synaptic input. The generation of spikes is implemented by a spike-and-reset rule: whenever the voltage reaches a threshold level V_{thr} a spike is fired, the voltage is reset to a fixed value V_{reset}, and after an absolute refractory time τ_{ABS} it is allowed to evolve again according to Eq. (5) until it reaches the threshold once more, when the sequence is repeated again. Using the non-dimensional variable $v = (V - V_{\mathrm{reset}})/(V_{\mathrm{thr}} - V_{\mathrm{reset}})$ and measuring time in units of the membrane time constant $\tau_{\mathrm{mem}} = R_{\mathrm{leak}}C$, we can recast Eq. (5) into the simpler equation

$$\dot{v} = -v + \mu + \epsilon\cos(\omega t) + \sqrt{2D}\xi(t) \ , \tag{6}$$

where all constant terms are lumped into the so-called base current μ,[1] while $\epsilon\cos(\omega t)$ and $\xi(t)$ stand for the rescaled periodic signal and Gaussian white noise, respectively. With our transformation, the threshold is now always at $v_T = 1$, the reset is zero ($v_R = 0$) and the absolute refractory period is given by $\tau_{\mathrm{abs}} = \tau_{\mathrm{ABS}}/\tau_{\mathrm{mem}}$.

The output of the neuron, $\sigma(t)$, is a train of δ spikes representing action potentials:

$$\sigma(t) = \sum_{t_i \in \mathscr{T}} \delta(t - t_i) \ . \tag{7}$$

The parameter μ determines the resting value of the voltage. In the following we mainly consider the case $\mu < 1$, in which the LIF model shows excitability.

The general behavior of the LIF model is illustrated in Fig. 5, where a trajectory of the voltage and the generated spike train are shown. Note that for $\mu < 1$ the LIF model exhibits three time scales with distinct noise dependence. One time scale is the passage from reset to resting voltage, which can be looked upon as a relative refractory period, since escapes to threshold are unlikely during this time. The second time scale is determined by the noise activated escape from the resting level to threshold—the activation time, which displays a strong dependence on noise intensity. Finally, the third time is given by the absolute refractory period; by definition, it does not depend on the noise at all.

We want to draw the reader's attention to one important extension of the standard input used in Eq. (6). For cortical neurons both signal and noise are received in the form of massive spike train inputs from many other neurons (Fig. 6). In this scenario, a signal may arise because a subpopulation of the input-generating neurons fires with a common rate (population code) $s(t) = s_0 + \epsilon\cos(\omega t)$.

[1] Of course μ is a non-dimensional quantity, but it originates essentially from a constant input current.

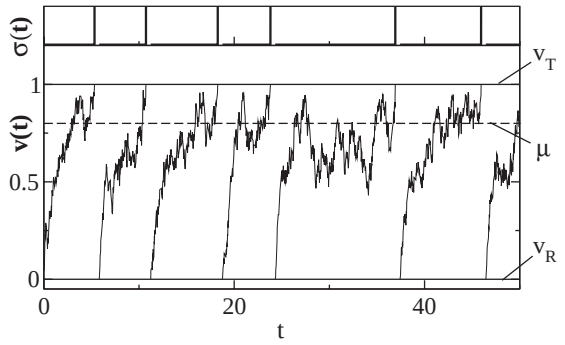

Fig. 5. Trajectory of the voltage variable $v(t)$ in the leaky integrate-and-fire model and generated spike train for $\mu = 0.8, D = 0.015, \tau = 0.5$.

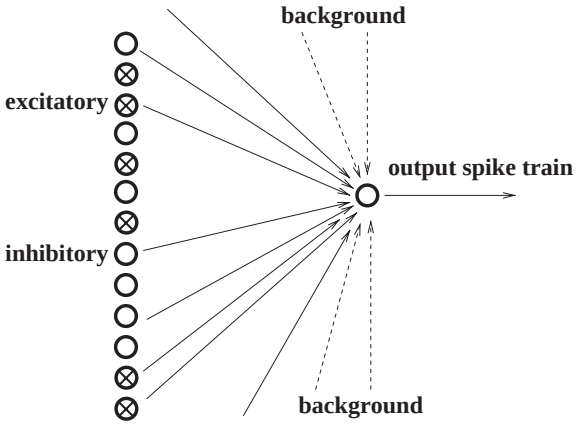

Fig. 6. The input signal of a LIF neuron is generated by neuronal background spikes (Poisson process with constant rate) and by a population of excitatory and inhibitory neurons firing with a time dependent rate $s(t) = s_0 + \epsilon \cos(\omega t)$.

Such a signal encoded in the rate of the input spike trains will be seen in the spooled input as a noise with signal-dependent mean [additive signal as in Eq. (6)] but also with a signal-dependent intensity (noise-coded signal, cf. Fig. 7) [112,248,249,244]. A LIF model that includes a noise-coded signal has been studied in Refs. [112,244]:

$$\dot{v} = -v + \mu + \varepsilon_\alpha \cos(\omega t) + \sqrt{2[D + \varepsilon_\beta \cos(\omega t)]}\xi(t) \ . \tag{8}$$

The relations between the effective parameters $\mu, \varepsilon_\alpha, \varepsilon_\beta$, D and the parameters of the input ensemble can be found in Refs. [112,244]. Here we note only that the noise intensity D possesses a lower bound $D > \varepsilon_\beta$ and can be varied by changing the strength of the neuronal background.

The simple LIF model introduced above can be still extended in many respects. Brunel and coworkers [243,245,250] have explored the important case where the input noise is not a white but a colored noise (Ornstein–Uhlenbeck process), corresponding to a spike train input that is filtered by a first-order synaptic dynamics. Another important generalization concerns the inclusion of nonlinear

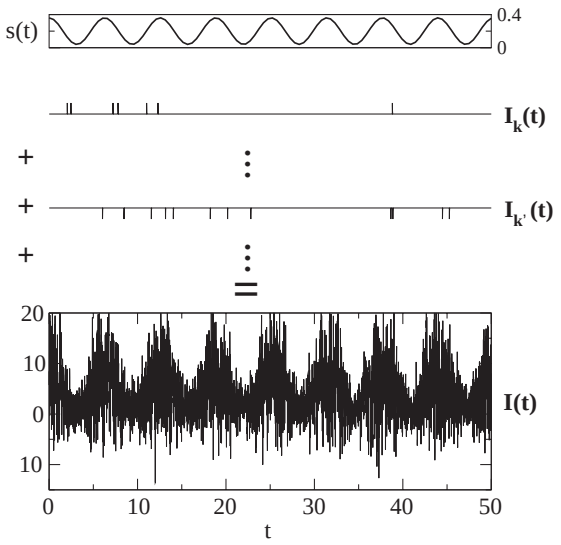

Fig. 7. The superposition of the spike trains $I_k(t)$ generated by the input neurons yields a noisy signal with a mean and a variance depending on the population's activity $s(t)$.

terms, e.g. in the so-called quadratic integrate-and-fire (QIF) neuron [251–253]. While the standard LIF model is neither clearly type I nor type II excitable, the QIF model is type I excitable and is even in close relation to the Θ neuron model and the normal form of a saddle-node bifurcation (see for instance [254]). Many other generalizations of the leaky integrate-and-fire model, including one with a dynamical threshold [255] and two- or three-variable LIF models [256–259] exist in the literature.

2.5. Phase description of excitability

Besides the LIF model, there is another one-dimensional system that can be regarded as excitable. The main feature of excitability in two-dimensional systems like the FN model is given by the noise-induced motion along the stochastic limit cycle with one stable point (the resting state that is left in the presence of noise).

This behavior can be alternatively described by an amplitude and a phase, where the latter variable captures the excitability features of the system [116,105,260] (cf. Fig. 8). These excitable phase models are extensions of the phase oscillator dynamics developed by Kuramoto and coworkers [114,115].

Let us first discuss in a purely phenomenological manner how a one-dimensional dynamics for the phase ϕ should look like. First of all, in a one-dimensional description the driving term can be always regarded as a potential force. This potential force should be 2π-periodic since ϕ is a cyclic variable. The potential should have one minimum corresponding to the resting state. Furthermore, for strong time scale separation the system passes through the stochastic limit cycle only in one direction. This corresponds to a bias in positive direction. Finally, there is a signal and a noise, which in the simplest case can be assumed to enter the dynamics independently of the phase variable. We thus

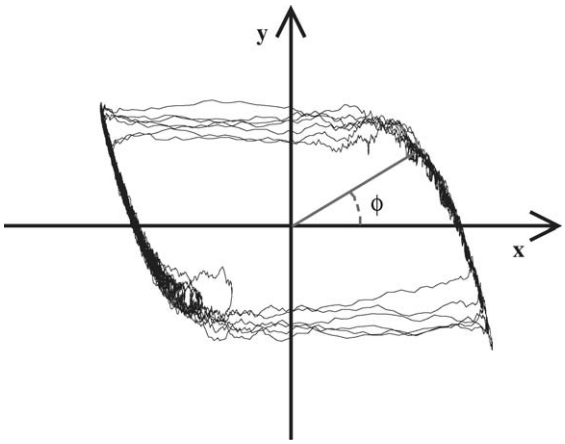

Fig. 8. Trajectory of FN model in phase space, specifying the phase variable.

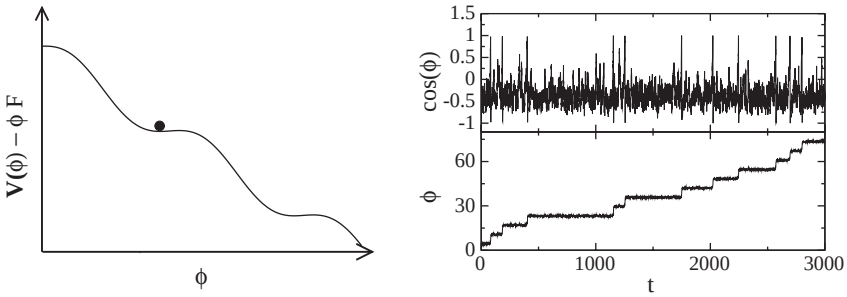

Fig. 9. Left: the effective potential in Eq. (9) for the case of a cosine potential and $F = 0.9$. Right: Stochastic trajectory of the phase variable (bottom) and excitable behavior seen in the corresponding value of the potential $\cos(\phi)$ (top) for $F = 0.9$ and $D = 0.02$.

arrive at the following first order dynamics for the phase:

$$\dot{\phi} = -V'(\phi) + F + s(t) + \sqrt{2D}\xi(t) \ . \tag{9}$$

Excitations (spikes) occur when the phase variable crosses a prescribed level, e.g. $\phi = \pi$ [actual spikes can be seen when the value of the potential $V(\phi(t))$ is plotted as a function of time, cf. Fig. 9 (right)]. An interspike interval is the time needed to go once around the circle, e.g. from $-\pi$ to π. The excitable regime of this phase model is obtained for a subcritical tilt F, for which the effective potential $V(\phi) - F\phi$ possesses a minimum (the rest state) and a maximum (an effective threshold). In other words, for a subcritical tilt, in order to get into the firing state (i.e. to pass the threshold), the system has to be externally excited by signal and/or noise. The effective potential and a number of purely noise-induced excitations are shown for $V(\phi) = \cos(\phi)$ in Fig. 9. Note that we consider here ϕ as an unbounded variable. Since the system is 2π-periodic, this does change the dynamics but provides the additional information how many excitations have occurred in a certain time interval.

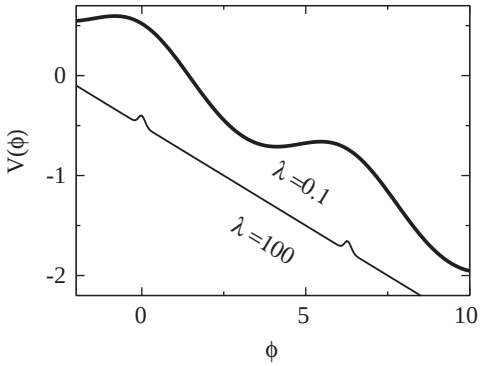

Fig. 10. The potential Eq. (10) for decreasing values of $\lambda = 100$ and 0.1 with $\Delta = 10.0$ and 0.282, respectively.

The equation governing the phase dynamics with the potential $V(\phi) = \cos(\phi)$ is usually called the Adler equation [261]. It is actually a good approximation for type I excitability, since close to the bifurcation point $F = 1$ it coincides to second order with the normal form of a saddle-node bifurcation. Another variant of Eq. (9) involving a cosine potential but also a multiplicative noise, the Θ neuron, can be *strictly* derived from any two-dimensional type I excitable model close to its bifurcation point [260,262].

We initially attempted to motivate phase models by viewing them as a phase description of the FitzHugh–Nagumo system, which is actually type II excitable. However, we have seen that the phase models described so far are (strictly speaking) type I excitable models. Are then phase models only suitable for type I excitability, or can they be actually used to approximate a type II excitable system like the FitzHugh–Nagumo model? We will demonstrate later that a phase model with a potential like

$$V(\phi) = \frac{\Delta}{\lambda}\, e^{\lambda(\cos(\phi)-1)} \tag{10}$$

can show a firing statistics akin to that of type II excitable models. Note that this is the case for large values of the parameter λ, for which the potential exhibits large extended flat parts and small and sharp barriers (see Fig. 10).

The dynamics of Eq. (9) with the potential Eq. (10) has been studied in Ref. [263]. In that work, as well as in many other papers, the variable ϕ in Eq. (9) was not interpreted as a phase, but as the position variable of an overdamped Brownian particle in an inclined periodic potential. Apart from the phase dynamics and the Brownian motion, there are other physical systems described by Eq. (9) (see [264]).

3. Noise-induced resonances in homogeneous excitable systems

When an excitable system is permanently perturbed by noise, it responds with an excitation sequence that is called a "pulse train" or "spike train". For small and large noisy forcing, this spike train is basically governed by the noise statistics and hence it appears as random. For intermediate noise intensity, however, this may be different. In fact, there exists a finite strength of the noise at which the spike sequence is most regular.

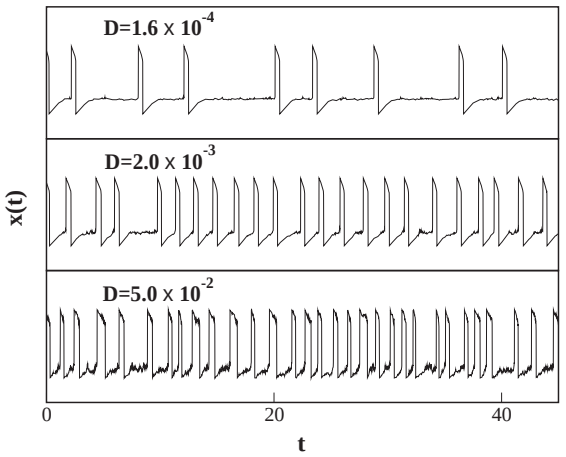

Fig. 11. Coherence resonance in the FitzHugh–Nagumo model. Numerical simulations of the stochastic dynamics of Eq. (1) with $\gamma = 1.5$, $b = 0.6$, $\epsilon = 10^{-3}$.

In general, this effect is due to the existence of a quasi-threshold and to the presence of the refractory period (which corresponds to the characteristic time scale determined by the decay of the unstable state). The existence of a threshold implies that the excitation time is controlled by noise, while the refractory time is determined mainly by the deterministic properties of the system and depends just weakly on the noise intensity. Optimal noise balances these two time scales in such a way that the interspike intervals are mainly determined by the dynamical refractory period with small fluctuations [48]. While in type II excitable systems the increase of spike train incoherence in the strong noise limit is mainly due to the increased jitter of the refractory period, in type-I excitable systems coherence is lost due to a noise-induced destruction of the spike shape itself [47,266].

The effect described above was called *coherence resonance* (CR) [48], *autonomous stochastic resonance* [49], *internal stochastic resonance* [265] or *stochastic resonance without periodic forcing* [47,266]. An example of coherence resonance in the FitzHugh–Nagumo model is shown in Fig. 11. For weak noise (top panel) the output spike train looks random, and the interval between excitations (interspike intervals) varies substantially. At moderate noise (mid panel) the spiking is rather regular, which implies that the interspike intervals do not differ much. Finally, at large noise intensity (bottom panel) the spikes are much more frequent than in the other cases, but the interspike intervals are more irregular again.

Recently, an effect opposite to coherence resonance has been discovered: the irregularity of spiking can be maximized if the driving noise has an finite "optimal" value. This incoherence maximization [57] or anti-coherence resonance [55] may occur for very different physical reasons. For the FitzHugh–Nagumo model, for instance, it can be observed at low noise if damped subthreshold oscillations are present. A completely different mechanism for noise-enhanced irregularity in the LIF model was found in [57] and is discussed in Section 3.2.6.

If a weak driving is present another effect can be observed: *stochastic resonance* (SR) [109,267,268]. SR was originally proposed and studied for bistable systems and later also found in excitable systems (see [109] and references therein). SR occurs in a wide range of nonlinear systems and manifests

itself by an enhancement of the response of a system to a weak signal by adding noise to the system. In the case of periodic signal these features become apparent by inspecting the power spectrum of the spike train or of one of the system's variable. The spectrum consists of a noisy background and peaks at the driving frequency and its multiples. The weights of these peaks as well as their ratio to the background spectrum pass through maxima as functions of noise intensity. For excitable systems an interesting question is how coherence resonance features affect stochastic resonance.

3.1. Resonance measures

3.1.1. Measures of coherence

The first problem encountered in the study of spiking behavior of excitable systems is the definition of a spike. This definition is evident in the LIF model. For the FN model we have to define a threshold level x_T (e.g. $x_T = 0$) in the voltage variable, an up-crossing of which is considered as the onset of a spike. Note that a short correlated noisy driving in the equation of the fast variable requires a more elaborated decision scheme, since in this case the voltage variable may cross a given level without passing actually through refractory and resting states (see [269] for further details). Given this decision rule we can measure the set of spiking times $\mathscr{T} = \{t_i\}$, and associate a δ spike train with them

$$\sigma(t) = \sum_{t_i \in \mathscr{T}} \delta(t - t_i) \ . \tag{11}$$

By integration of this function from 0 to t we obtain the number of spikes in the time window $(0, t)$, which is called the spike count $n(t)$. The quantity is a stochastic variable that undergoes a diffusive spreading. The stationary firing rate r_0 is the mean number of spikes per unit time, which can be determined by either $n(t)$ time averaging or ensemble averaging from the output of Eq. (11):

$$r_0 = \lim_{t\to\infty} \frac{n(t)}{t} = \langle \sigma(t) \rangle \ . \tag{12}$$

Equivalently, one may measure the statistics of the interspike interval (ISI), such as for instance the mean ISI $\langle T \rangle$, which is the inverse of the firing rate:

$$r_0 = \lim_{N\to\infty} \left(\frac{T_0}{N} + \frac{1}{N} \sum_{i=1}^{N} T_i + \frac{T_{N+1}}{N} \right)^{-1} = \frac{1}{\langle T \rangle} \ . \tag{13}$$

Here we have in mind a time series from $t = t_0$ to $t = t_{N+2}$ with $N + 1$ spike times t_i in between. Then $T_i = t_{i+1} - t_i$ (for $i = 1, \ldots, N$) denote the intervals between subsequent spikes, while T_0 and T_{N+1} are the intervals until the first and since the last spike have occurred. The latter two intervals can be neglected for large N. Note that consecutive intervals are statistically independent, i.e. LIF and FN models generate so-called renewal processes [270] (for the FN model this is true, at least to a very good approximation, for $\epsilon_t \ll 1$).

The variability of spike timing is quantified by other measures, the most common of which is the *coefficient of variation* R (CV), defined as the ratio of the standard deviation of the interspike intervals to its mean:

$$R = \frac{\sqrt{\langle \Delta T^2 \rangle}}{\langle T \rangle} \ . \tag{14}$$

Here $\langle T\rangle$ is the mean and $\langle \Delta T^2\rangle = \langle T^2\rangle - \langle T\rangle^2$ is the variance of the interspike interval. A Poisson process has $R = 1$ and a strictly periodic spiking has $R = 0$. Hence, if R is close to zero one may speak of a coherent output. The coherence resonance seen in Fig. 11 becomes therefore manifest by a minimum of the coefficient of variation vs noise intensity [48]. We must point out that the usage of the CV as the *only* indicator of coherence resonance can be misleading (see Ref. [310] and Section 3.2.5).

One may also use spike count statistics to quantify the regularity of spiking. As mentioned above, the spike count exhibits a diffusive spreading, i.e. its variance grows linearly with time. For renewal processes like those generated by LIF and FN models, the *diffusion coefficient* D_{eff} associated with that spreading can be calculated from the mean and variance of the interspike interval [270], and is thus related to CV and spike rate:

$$D_{\mathrm{eff}} = \lim_{t\to\infty} \frac{\mathrm{d}}{\mathrm{d}t} \frac{\langle n^2(t) - \langle n(t)\rangle^2\rangle}{2} = \frac{1}{2}\frac{\langle \Delta T^2\rangle}{\langle T\rangle^3} = \frac{1}{2} R^2 r_0 \ . \tag{15}$$

A small growth of the variance implies then a small value of the diffusion coefficient of the spike count, and indicates a regular spiking. Consequently, a strong manifestation of coherence resonance is the occurrence of a minimum in the diffusion coefficient vs noise intensity.

Another measure of coherence is the *correlation time* of the system, defined as the integral of the squared correlation function of one of the output variables [48]. Coherence resonance is characterized by a maximum of this quantity [48]. An estimate of the correlation time can be made using the diffusion coefficient and the spike rate [244], yielding essentially an inverse relationship [2]

$$\tau_{\mathrm{corr}} \sim \frac{1}{2D_{\mathrm{eff}}} - \frac{1}{r_0} \ . \tag{16}$$

Assuming that the spike rate r_0 increases monotonously with increasing noise, which is the case for all excitable systems considered in this review, one can show that a minimum of D_{eff} vs noise intensity implies a maximum in the correlation time Eq. (16). Thus if we find the signature of CR in the diffusion coefficient (minimum vs noise intensity), CR can be also observed (possibly at a slightly different noise level) by means of the correlation time.

Finally, the power spectrum of either the spike train or another dynamical variable of the system may be considered as measure of the coherence. For a process $x(t)$, its power spectrum is given by

$$S_x(\omega) = \int_{-\infty}^{\infty} \mathrm{d}\tau \, \langle x(t)x(t+\tau)\rangle \mathrm{e}^{\mathrm{i}\omega\tau} \ . \tag{17}$$

A quasi regular output (as in the case of coherence resonance, see for instance the mid panel of Fig. 11) should be characterized by a peak at a finite frequency, irrespective of whether $x(t)$ is the spike train or another system's variable. This peak can be quantified by the degree of coherence, which is the ratio of peak height to the width at which the spectrum decays to a fraction a of its maximal value

$$\beta = \frac{S(\omega_{\max})}{\Delta\omega/\omega_{\max}} \tag{18}$$

with

$$\Delta\omega = \omega_1 - \omega_2, \quad S(\omega_1) = S(\omega_2) = S(\omega_{\max})/a, \quad \omega_1 < \omega_{\max} < \omega_2 \ . \tag{19}$$

[2] This estimate is meaningful only for processes that are more regular than a Poisson process.

Note that for a renewal process, the power spectrum of the spike train can be expressed in terms of the characteristic function of the ISI (i.e. the Fourier transform of the ISI density, see e.g. [271]):

$$S_{\sigma-\langle\sigma\rangle}(\omega) = \frac{1}{\langle T\rangle}\,\frac{1-|\varrho(\omega)|^2}{|1-\varrho(\omega)|^2}\ . \tag{20}$$

Later on we will approximate the voltage variable of the FN model by a two-state process $\sigma(t)\in\{-1,1\}$, where the two states correspond to the resting state (voltage around resting potential) and the excited state (voltage at the peak of the spike). The interspike interval in that case consists of two approximately independent subintervals, namely the waiting times in the respective states. Under these conditions, the spectrum of $\sigma(t)$ can be expressed by the characteristic functions of the subintervals $\rho_r(\omega)$ and $\rho_l(\omega)$ as follows [271]:

$$S_{\sigma-\langle\sigma\rangle}(\omega) = \frac{8}{\omega^2\langle T\rangle}\Re\left(\frac{(1-\varrho_l(\omega))(1-\varrho_r(\omega))}{1-\varrho_l(\omega)\varrho_r(\omega)}\right)\ . \tag{21}$$

3.1.2. Measures for signal transmission

If an excitable system is stimulated by a periodic signal ($s(t)=\varepsilon\cos(\Omega t)$) and noise, the ensemble-averaged measures will explicitly depend on time. This is seen, for instance, in the instantaneous firing rate $r(t)$ that corresponds to the ensemble average of the spike train Eq. (11). For a weak signal, the rate is given by

$$r(t) = \langle\sigma(t)\rangle = r_0 + \varepsilon\alpha\cos(\Omega t-\phi)\ , \tag{22}$$

where α is a linear-response amplitude and ϕ is the phase shift. A similar ansatz can be made for the ensemble-averaged variables of the excitable system.

The response amplitude α is an illustrative measure for the presence of the signal in the output. However, measures derived from the power spectrum of dynamical variables or of the spike train are often more accessible for numerical simulations or experiments. For a weak signal the power spectrum is given by

$$S(\omega) = S_{\mathrm{bg}}(\omega) + \frac{\pi}{2}\,\varepsilon^2\alpha^2\left[\delta(\omega-\Omega)+\delta(\omega+\Omega)\right]\ . \tag{23}$$

A simulation of a LIF neuron driven by white noise and a periodic signal (Fig. 12) shows clearly the continuous and discrete components in the power spectrum. For a weak signal, the continuous contribution background spectrum S_{bg} is given by the spectrum of the unperturbed system ($\varepsilon=0$). In Fig. 12 this is nicely confirmed by the grey line, given by an exact expression for the spectrum in the absence of a signal [Eq. (37) in Section 3.2.2].

Regarding the discrete component, note that in any finite simulation (as well as in any experiment), instead of the δ peaks we obtain peaks of finite height. However, the area under the peak will be given, for sufficiently large measuring or simulation time, by the prefactor of the δ functions in Eq. (23).

The strength of the periodic output signal can be quantified by the spectral amplification [109,272], which is given by the ratio of signal output power to input power:

$$\eta = \alpha^2\ . \tag{24}$$

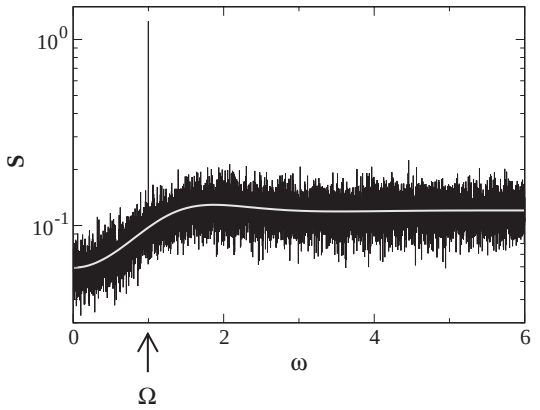

Fig. 12. Power spectrum (histogram) averaged over 30 realizations for the LIF model driven by an additive signal ($\varepsilon = 0.02, \Omega = 1$) at $\mu = 0.8$ and $D = 0.015$. The peak at $\omega = 1$ depends on the simulation time, here $T = 10^4$.

More common in experimental measurements is the signal-to-noise (SNR) ratio, which measures how well the spectral peak can be distinguished from the noise background. For a finite-time estimate of the power spectrum, the SNR can be defined by dividing the height of the signal peak by the background spectrum S_{bg}. In theoretical considerations it is desirable to eliminate the trivial linear dependencies on simulation time and input power introduced in the experimental SNR. To that end, the ratio of power amplification (i.e. peak height divided by input power and measuring time) to the background spectrum at the driving frequency is considered the theoretical equivalent of the SNR:

$$\mathrm{SNR} = \alpha^2 / S_{\mathrm{bg}} \ . \tag{25}$$

Another measure often used in studies of stochastic resonance are the residence time distributions [273,274], which are similar to the interspike interval histograms used in neuroscience [275,276]. The quality of signal transmission can also be characterized in terms of phase synchronization [277–283]: the cumulative sequence of phase jumps due to switchings or firings [284] (if discretized, the spike count times 2π) is locked for the longest average time by a signal at the optimal noise level. In the case of aperiodic signals, the appropriate measures include the cross-correlation and the coherence functions [106,281,285–287], as well as the theoretical information measures [288–297] and wavelets [298].

Here we focus mainly on periodic signals and study the dependence of spectral measures on noise intensity and driving frequency.

3.2. Coherence resonance

3.2.1. Coherence resonance in the FitzHugh–Nagumo model

In Fig. 11 it was shown that the FN model displays coherence resonance. Here we describe an analytical approach that allows us to determine the measures of CR in this model.

Our starting point is the separation between time scales in the dynamics of Eq. (1). The time scale ratio ϵ_t is close to zero, and so we may ask how the system behaves if we take the limit

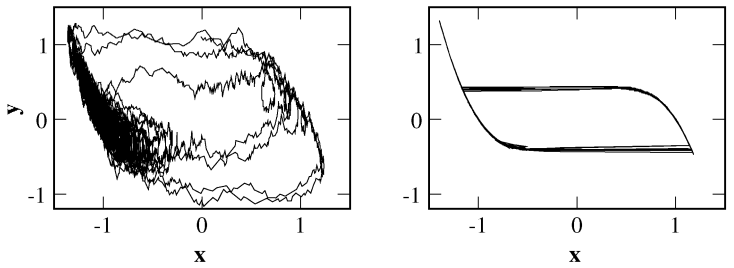

Fig. 13. Comparison of stochastic trajectories at different values of the time scale separation constant ϵ_t (see also Fig. 4). Parameters: $\gamma = b = 1.5$, $D = 0.3$; Left: $\epsilon_t = 10^{-1}$, right: $\epsilon_t = 10^{-4}$.

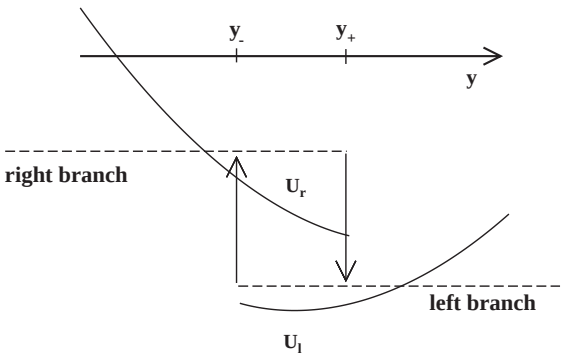

Fig. 14. Schematic picture of the system for $\epsilon_t \to 0$.

$\epsilon_t \to 0$. This is demonstrated in Fig. 13 (left) in agreement with the solutions of the stationary FPE described in Section 2.3. The two-dimensional stochastic system reduces for $\epsilon_t \to 0$ to a system of two one-dimensional subsystems corresponding to the stable branches of the cubic nullcline, which are connected by the probability fluxes from one branch to the other.

The dynamics of the slow variable y is schematically depicted in Fig. 14 (right) and resembles a Schmitt trigger driven by colored noise, as considered by Melnikov [299]. The phase point performs a diffusive motion on the left (right) branch until it is absorbed at the y coordinate of the minimum y_- (maximum y_+) of the cubic nullcline, and reset to the right (left) branch. The motion is subjected to the force of effective potentials that read

$$U_l(y) = \frac{(y-b)^2}{2} - \gamma \frac{x_l(y)}{4}(3y - x_l(y)) \ ,$$
$$U_r(y) = \frac{(y-b)^2}{2} - \gamma \frac{x_r(y)}{4}(3y - x_r(y)) \ . \tag{26}$$

for the left and right branch, respectively.

In order to obtain these functions, one has to insert the inverse of the cubic function given by Eq. (2):

$$x_l(y) = 3y_- \cosh\left(\frac{1}{3}\operatorname{arccosh}(y/y_+)\right) \ ,$$

$$x_r(y) = 3y_+ \cosh\left(\frac{1}{3}\operatorname{arccosh}(y/y_-)\right) \tag{27}$$

into the equation of the recovery variable. Note that the potential $U_r(y)$ does not possess a minimum (cf. Fig. 14), in accordance to the observation that the right branch is abandoned even in the absence of noise (the phase point will go "downhill" to the absorbing boundary in this case). Fokker–Planck equations for the two subsystems (which are coupled by probability currents) can be found, and the stationary density can be obtained [53].

More interesting in the context of coherence resonance is the fact that we may calculate the moments of the first-passage times along these branches (see also Refs. [300,301]). Obviously, in the limit $\epsilon_t \to 0$ the sum of the first passage times $\langle T_l\rangle$, $\langle T_r\rangle$ from y_+ to y_- (left branch) and vice versa (right branch) yields the interspike interval. Furthermore, the passage times are statistically independent, which implies that

$$\langle T\rangle = \langle T_l\rangle + \langle T_r\rangle, \quad \langle \Delta T^2\rangle = \langle \Delta T_l^2\rangle + \langle \Delta T_r^2\rangle \ . \tag{28}$$

The moments can be obtained by standard formulas [302], which in the case of T_r can be written

$$\langle T_r\rangle = \int_{y_-}^{y_+} \mathrm{d}x\, I_r(x), \quad I_r(x) = \frac{1}{D}\,\mathrm{e}^{U_r(x)/D} \int_{-\infty}^{x} \mathrm{d}y\, \mathrm{e}^{-U_r(y)/D} \tag{29}$$

and

$$\langle \Delta T_r^2\rangle = 2\int_{-\infty}^{y_+} \mathrm{d}z [I_{l,r}(z)]^2 \mathrm{e}^{-U_r(z)/D} \int_{z}^{y_+} \mathrm{d}x\, \Theta(z-y_-)\mathrm{e}^{U_r(x)/D} \ . \tag{30}$$

For the passage time toward the left branch similar formulas can be used when $U_r(y)$ is replaced by $U_l(-y)$.

From the moments we can calculate the stationary spike rate r_0, i.e. the inverse mean interspike interval, by means of Eq. (13), and also determine the coefficient of variation

$$R = \frac{\sqrt{\langle \Delta T_l^2\rangle + \langle \Delta T_r^2\rangle}}{\langle T_l\rangle + \langle T_r\rangle} \ . \tag{31}$$

The knowledge of r_0 and R, moreover, permits the determination of the spike diffusion coefficient according to Eq. (15).

The coefficient of variation and the spike-count diffusion coefficient obtained from the theory sketched above are shown in Fig. 15, and compared to simulations at different values of ϵ_t. One can see that at fixed ϵ_t both measures attain minima at roughly the same noise intensity. These minima are more shallow and appear at larger noise intensity when the time scale ratio is increased. The deviation of the approximation given by the theoretical formulas at $\epsilon_t = 0$ increases with increasing ϵ_t, as one may expect.

Note, furthermore, that not for all parameter sets where the FN model is excitable, both quantities necessarily have to attain a minimum. For the case $\gamma = 0.8$ and $b = 0.9$, the fixed point has a large

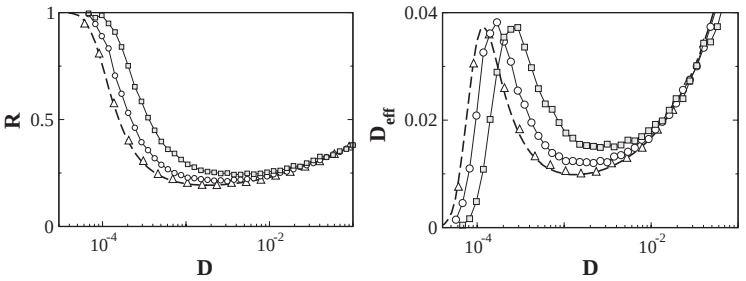

Fig. 15. Coefficient of variation (left) and diffusion coefficient of the spike count (right) vs noise intensity D for $\gamma = 1.5$, $b = 0.6$. Approximation (solid line) compared to simulations with $\epsilon_t = 10^{-3}$ (squares), $\epsilon_t = 10^{-4}$ (circles) and $\epsilon_t = 0$ (triangles).

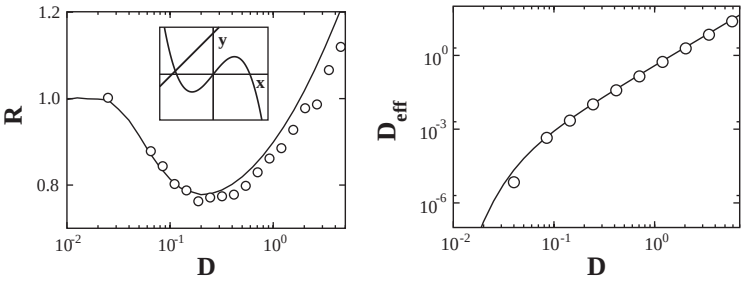

Fig. 16. Coefficient of variation (left) and spike-count diffusion coefficient (right) vs noise strength D, for $\gamma = 0.8$ and $b = 0.9$ (the nullclines for these parameters are shown in the inset). The theoretical approximation (solid line) is compared to simulations with $\epsilon_t = 10^{-4}$ (circles).

distance to the "self-excitatory" region (cf. inset of Fig. 16), which implies a small ratio of excursion and activation times. Consequently, only a weak form of coherence resonance exists. In this case, only the coefficient of variation possesses a (very shallow) minimum, while the diffusion coefficient is a monotonous function of the noise intensity (cf. Fig. 16).

As was shown in [110], the power spectrum can be also calculated in the limit $\epsilon_t \to 0$ applying some additional minor modifications. First, the cubic polynomial is replaced by the piecewise linear function Eq. (3) (this is not necessarily a bad choice with respect to the biological application of the model [303]). Second, the spectrum of the variable $x(t)$ is approximated by that of a discretized variable $\sigma(t) = \mathrm{sgn}(x(t))$. Since the changes in v along the branches are small compared to the change due to a jump from one branch to the other, this approximation will introduce a negligible deviation.

If both nullclines are (piecewise) linear, the resulting effective potentials will be parabolic. The power spectral density can then be calculated [110] generalizing a result due to Melnikov [299]. Expressed by parabolic cylinder functions [304] denoted by $\mathscr{D}_{a,z}$, the result reads

$$S(\omega) = \frac{8r_0}{\omega^2}\,\Re\left(\frac{\left[\mathscr{D}_{i,\omega}\left(\frac{x_-}{\sqrt{D}}\right) - \mathrm{e}^{\Delta x}\mathscr{D}_{i,\omega}\left(\frac{x_+}{\sqrt{D}}\right)\right]\left[\mathscr{D}_{i,\omega}\left(\frac{y_-}{\sqrt{D}}\right) - \mathrm{e}^{\Delta y}\mathscr{D}_{i,\omega}\left(\frac{y_+}{\sqrt{D}}\right)\right]}{\mathscr{D}_{i,\omega}\left(\frac{x_-}{\sqrt{D}}\right)\mathscr{D}_{i,\omega}\left(\frac{y_-}{\sqrt{D}}\right) - e^{\Delta x}\mathrm{e}^{\Delta y}\mathscr{D}_{i\omega}\left(\frac{x_+}{\sqrt{D}}\right)\mathscr{D}_{i\omega}\left(\frac{y_+}{\sqrt{D}}\right)}\right)\,, \tag{32}$$

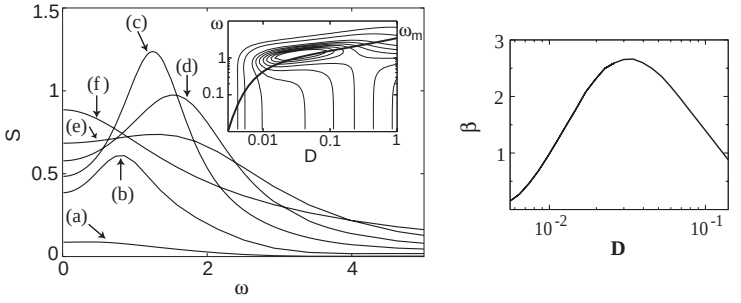

Fig. 17. Left: output spectrum vs frequency for $\gamma = 1$, $b = 0.4$, and different noise levels (a)–(f): $D = 0.004$, 0.009, 0.033, 0.094, 0.207, 0.769. Inset: contour plot of spectral density vs D and ω, compared with the mean frequency $\omega_m(D) = 2\pi r_0$ (thick line) where $r_0 = 1/\langle T \rangle$ is the stationary spike rate. Right: degree of coherence according to Eq. (18) with $a = 1.2$.

where

$$\Delta x = \frac{x_+^2 - x_-^2}{4D}, \quad \Delta y = \frac{y_+^2 - y_-^2}{4D} \tag{33}$$

and

$$x_\pm = \pm\frac{1}{2} - \frac{b-\gamma}{1+\gamma}, \quad y_\pm = \pm\frac{1}{2} + \frac{b+\gamma}{1+\gamma}\ . \tag{34}$$

Additionally, time and noise intensity have been rescaled according to $t \to t/(1+\gamma)$ and $D \to (1+\gamma)D$, respectively. The spectrum indeed reveals coherence resonance (Fig. 17). At small and large noise it has an almost monotonous shape, while at moderate noise intensity a pronounced peak appears.

As shown in Fig. 17 (right), the degree of coherence [Eq. (18)] passes through a maximum as a function of noise. Simulations of the full dynamics of Eq. (1) indicate a good agreement with these findings, provided the time scale ratio ϵ_t is sufficiently small.

3.2.2. *Coherence resonance in the leaky integrate-and-fire model*

A one-dimensional excitable system like the LIF model can also display coherence resonance [56,57]. This model has the advantage that many of the CR measures can be analytically calculated [57]. In the absence of a periodic signal [setting $\varepsilon = 0$ in Eq. (6)], the moments of the interspike interval are given by those of the first passage time in a parabolic potential from reset point to threshold. The first moment reads [305]

$$\langle T \rangle = \tau_{\rm abs} + \sqrt{\pi} \int_{(\mu - v_T)/\sqrt{2D}}^{(\mu - v_R)/\sqrt{2D}} {\rm d}z\, {\rm e}^{z^2}\, {\rm erfc}(z)\ , \tag{35}$$

where ${\rm erfc}(z)$ is the complementary error function [304]. The stationary spike rate r_0 is the inverse of this expression, according to Eq. (13). The second moment can be written as [57]

$$\langle \Delta T^2 \rangle = 2\pi \int_{(\mu - v_T)/\sqrt{2D}}^{\infty} {\rm d}x\, {\rm e}^{x^2} [{\rm erfc}(x)]^2 \int_{(\mu - v_T)/\sqrt{2D}}^{x} {\rm d}y\, {\rm e}^{y^2}\, \Theta\left(\frac{\mu - v_R}{\sqrt{2D}} - y\right)\ . \tag{36}$$

Fig. 18 shows the spike rate, coefficient of variation and spike-count diffusion coefficient for different values of μ and zero absolute refractory period. The function R possesses a minimum for

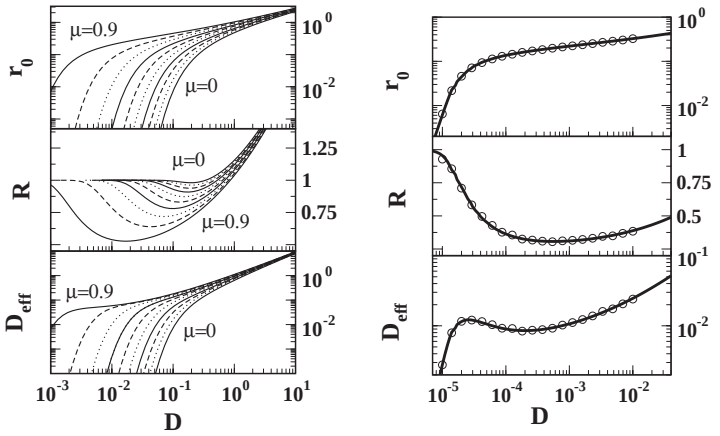

Fig. 18. Analytical results for the rate, coefficient of variation and diffusion coefficient vs noise intensity for $\tau_{\mathrm{abs}} = 0$. Left: The parameter μ is varied from 0 to 0.9 in steps of 0.1 (subthreshold base current μ, i.e. noise-activated firing regime). Right: For $\mu = 0.99$, the characteristics are compared to results (circles) from a numerical simulation of Eq. (6).

almost all values of μ, which deepens and shifts to smaller values of D with increasing μ. As pointed out above, the passage to $v = \mu$ can be looked upon as a relative refractory period. Increasing μ increases this period, and simultaneously diminishes the activation time needed to escape beyond the threshold. Note that the curves for different μ never intersect; this implies that the coherence of spiking is always increased with growing μ irrespective of the value of D.

Values up to $\mu = 0.9$ do not yield a minimum in the diffusion coefficient. For a resting value very close to the threshold (which is $v_T = 1$) a minimum can be nevertheless observed (cf. Fig. 18, right). This is in accordance with what happens in the FN model. The closer we are to the bifurcation point, the more pronounced is the CR effect.

Moreover, the power spectrum is simpler to calculate for the LIF than for the FN model. The characteristic function of the interspike interval has been known for a long time, and the power spectrum of the spike train can be expressed by Eq. (20) employing the characteristic function. The resulting spectrum reads [57]

$$S(\omega) := S_{\sigma-\langle\sigma\rangle}(\omega) = r_0 \frac{\left|\mathscr{D}_{i\omega}\left(\frac{\mu-v_T}{\sqrt{D}}\right)\right|^2 - \mathrm{e}^{2\Delta}\left|\mathscr{D}_{i\omega}\left(\frac{\mu-v_R}{\sqrt{D}}\right)\right|^2}{\left|\mathscr{D}_{i\omega}\left(\frac{\mu-v_T}{\sqrt{D}}\right) - \mathrm{e}^{\Delta}\mathrm{e}^{\mathrm{i}\omega\tau_{\mathrm{abs}}}\mathscr{D}_{i\omega}\left(\frac{\mu-v_R}{\sqrt{D}}\right)\right|^2} \,. \tag{37}$$

Here $\mathscr{D}_a(z)$ denotes again the parabolic cylinder function, and Δ is given by

$$\Delta = \frac{v_R^2 - v_T^2 + 2\mu(v_T - v_R)}{4D} \,. \tag{38}$$

Let us now consider the spectrum for the case $\mu = 0.99$. As in case of the FN model, the spectrum exhibits a peak in the case of coherence resonance, i.e. at a finite noise intensity.

Note that the spectrum does not decay at large values, but saturates at the stationary rate, i.e. $S(\omega \to \infty) = r_0$. This is due to the fact that we consider the spectrum of a δ-spike train, which has

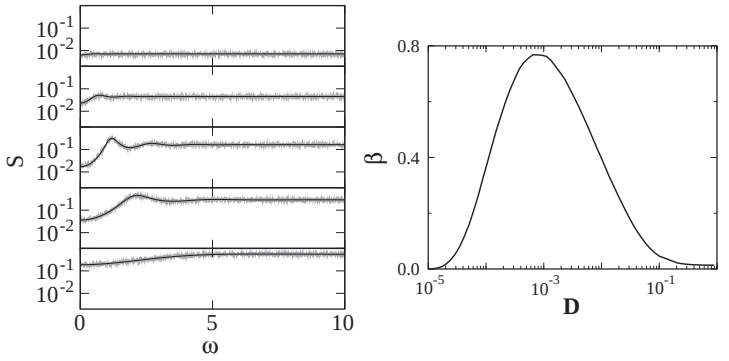

Fig. 19. Power spectra for different noise intensities (left) and degree of coherence vs noise intensity (right) for $\mu = 0.99$ and $\tau_{\text{abs}} = 0$. From top to bottom: $D = 10^{-5}$, 2×10^{-5}, 2×10^{-4}, 5×10^{-3}, 10^{-1}, theory (black) according to Eq. (37) compared to simulations (grey).

an infinite variance. As a measure of coherence resonance we use a modified version of the degree of coherence [3] [56]:

$$\beta = \frac{S(\omega_{\max}) - r_0}{\Delta\omega/\omega_{\max}} \ . \tag{39}$$

As seen in Fig. 19 (right) this function passes through a maximum as a function of noise.

The analytical results for the LIF model demonstrate that coherence resonance can be observed in one-dimensional systems. This is important, because it is sometimes asserted in the literature that CR is based on subthreshold oscillations around a fixed point that cannot be realized in one-dimensional (first-order) dynamics.

3.2.3. Coherence resonance in phase models

Coherence resonance has also been observed in a number of phase models. In the noisy Adler equation [i.e. Eq. (9) with a cosine potential], coherence resonance has been found numerically using spectral measures [58]. We recall that this model is type I excitable, because close to the bifurcation point it approaches the normal form of a saddle-node bifurcation. Here we will demonstrate CR in a noisy Adler equation by means of exact analytical results for the coefficient of variation and the diffusion coefficient of the spike count.

The mean and variance of the ISI in the phase model can be expressed by quadratures applying standard methods for the associated first-passage-time problem [302]. A considerably simplified expression for the variance was recently derived by Reimann and coworkers [306]:

$$\langle T \rangle = \frac{\int_0^{2\pi} \mathrm{d}x I_{\pm}(x)}{1 - \mathrm{e}^{-2\pi F/D}}, \quad \langle \Delta T^2 \rangle = 2D \int_0^{2\pi} \mathrm{d}x \, I_+(x) I_-^2(x) \ , \tag{40}$$

[3] The modification is needed since the power spectrum of the spike train does not decay to zero in the high-frequency limit.

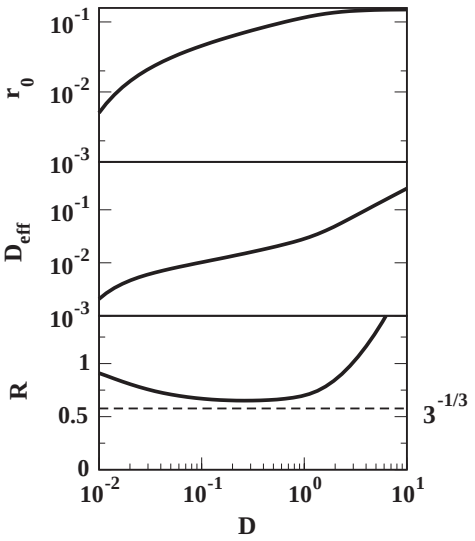

Fig. 20. Analytical results for the characteristics of the excitable phase model, i.e. rate, diffusion coefficient of spike count, and coefficient of variation of the interspike interval, as functions of the noise intensity. The cosine potential and a bias $F = 0.95$ were used.

where

$$I_+ := \frac{1}{D}\,\mathrm{e}^{V(x)/D}\int_{x-2\pi}^{x}\mathrm{d}y\,\mathrm{e}^{-V(y)/D}, \quad I_- := \frac{1}{D}\mathrm{e}^{-V(x)/D}\int_{x}^{x+2\pi}\mathrm{d}y\,\mathrm{e}^{V(y)/D}\ . \tag{41}$$

From these expressions we can calculate the spike rate, the coefficient of variation, and the diffusion coefficient of the spike count by means of Eqs. (13), (14), and (15), respectively.

Results for a strong subcritical tilt ($F = 0.95$) are shown in Fig. 20, and indeed reveal coherence resonance in the phase model. The CV passes through a minimum as a function of noise intensity. However, the type I excitable phase model exhibits only a weak form of coherence resonance. The CV does not fall below the value $1/\sqrt{3}$, and the diffusion coefficient of the spike count does not show a minimum. The former result does not depend on the bifurcation parameter, as long as the system is excitable (cf. Fig. 21). The lower bound for the CV is furthermore consistent with numerical findings for the type I excitable Morris–Lecar model [62] and with the fact that the normal form of a type I excitable system right at the bifurcation point possesses a CV that is given by the value $R = 1/\sqrt{3}$ [42,254].

We now show that using the potential shape given in Eq. (10) instead of a cosine potential, a firing statistics akin to type II excitability can be achieved. We recall that the potential Eq. (10) exhibits extended flat parts and small and sharp barriers for large values of the parameter λ.

At variance with the cosine phase model, the ISI is now not necessarily dominated by the escape over the threshold (the barrier of the effective potential), but can also (at comparably small noise intensity) be dominated by the passage along the flat parts of the potential. This leads to a strong coherence of the output spike train and to a pronounced coherence resonance (Fig. 22). The minimum of the CV is low ($R_{\min} \approx 0.28$) and the diffusion coefficient of the spike count passes through a minimum as a function of noise intensity. By varying the potential parameters Δ and λ, the minima

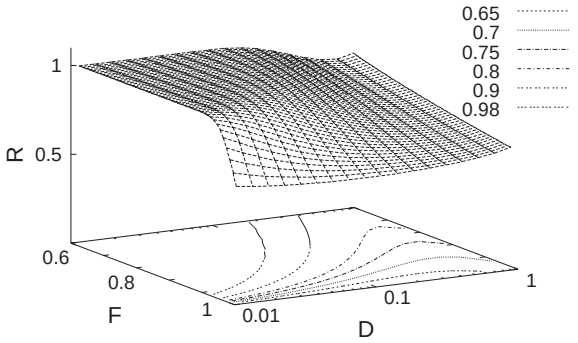

Fig. 21. The CV as a function of tilt (bifurcation parameter with critical value $F_c = 1$) and noise intensity for the cosine potential. A shallow minimum vs noise intensity can be observed for all values of $F \in [0.5, 0.99]$ and also inferred from the contour lines in the F–D plane.

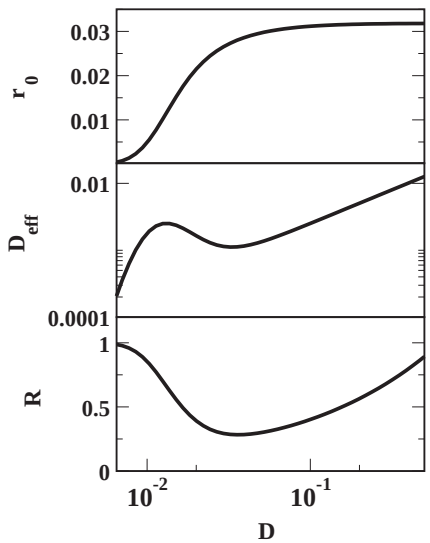

Fig. 22. Analytical results for the characteristics of the excitable phase model, i.e. rate, diffusion coefficient of spike count, and coefficient of variation of the interspike interval as functions of the noise intensity. The potential Eq. (10) with $\Delta = 10, \lambda = 100$ and a tilt $F = 0.2$ were used.

of the CV and the diffusion coefficient can be further deepened (not shown). These results resemble strongly the findings for the FitzHugh–Nagumo model presented in Fig. 15.

Finally, we would like to mention that the optimal spike output found in case of coherence resonance in the phase model is equivalent to a *coherent transport* of Brownian particles when the dynamics is regarded as a description of overdamped Brownian motion in an inclined periodic potential. Analytical results for this effect have been achieved in Refs. [263,307] (see also Refs. [306,308]). A further manifestation of coherent transport at finite noise has been recently discovered in a spatially periodic dynamics with multiplicative noise but zero tilt [309], which is a simple model

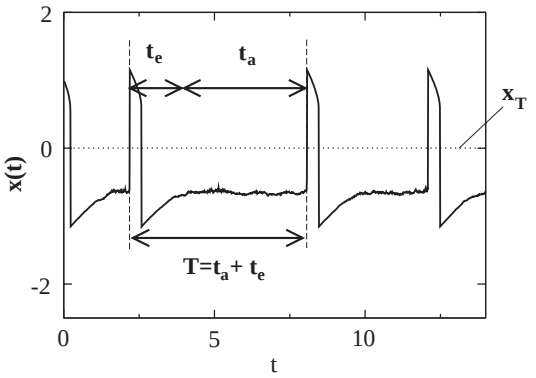

Fig. 23. Voltage variable of the FN model vs time. A division of the interspike interval into two subintervals (activation and excursion times) are indicated. The threshold level is $x_T = 0$.

of so called Brownian motors. This shows that the consequences of the simple CR effect can be more far reaching than one might expect at the first glance.

3.2.4. Qualitative approach to coherence resonance

How can the phenomenon of coherence resonance be understood? First, one has to realize that the interspike interval consists of two different times t_a (activation time) and t_e (excursion time), as illustrated in Fig. 23. The activation time is the time needed for the escape of the state point from the fixed point, while the excursion time corresponds to the interval the system spends in the active and refractory states. The statistics of these times is quite different: while the activation time obeys approximately a Poissonian statistics with strong dependence on the noise intensity, the excursion time corresponds instead to the decay time of an unstable state, and hence displays a much weaker dependence on the noise intensity than the activation time.

A simple consideration of the squared coefficient R^2 (which reaches its minimum for the same noise intensity as R) reveals the mechanism of coherence resonance (see also Pakdaman et al. [56]). Assuming statistical independence between the two times, we obtain for the squared coefficient of variation

$$R^2 = \frac{\langle \Delta(t_a + t_e)^2 \rangle}{\langle T \rangle^2} = \frac{\langle \Delta t_a^2 \rangle}{\langle t_a \rangle^2} \frac{\langle t_a \rangle^2}{\langle T \rangle^2} + \frac{\langle \Delta t_e^2 \rangle}{\langle t_e \rangle^2} \frac{\langle t_a \rangle^2}{\langle T \rangle^2} = R_a^2 \left(\frac{\langle t_a \rangle}{\langle T \rangle} \right)^2 + R_e^2 \left(\frac{\langle t_e \rangle}{\langle T \rangle} \right)^2 , \tag{42}$$

where R_a and R_e denote the coefficients of variation of the activation and excursion times, respectively.

If we assume a Poissonian process for t_a, the coefficient R_a is unity, and the first term will be the squared ratio of the activation time to the interspike interval. For increasing noise intensity this term drops rapidly from one to almost zero, while the second term increases in both factors: the jitter of the excursion time R_e as well as the ratio $\langle t_e \rangle / \langle T \rangle$. The minimum in R^2 (and hence in R) appears as a compromise at a noise intensity where both terms are just small (cf. Fig. 24), i.e. when the noise strength suffices to generate a small activation time compared to the excursion time, while it is still weak enough to introduce only a small jitter in the excursion time. In this case, the noise

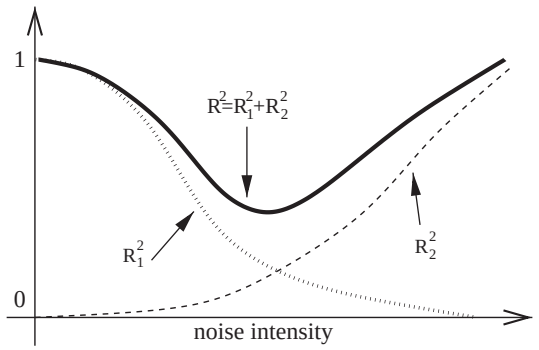

Fig. 24. Sketch of how the minimum in the CV occurs: the squared coefficient of variation can be split up into two monotonous functions of the noise intensity: the CV of the Poissonian activation time multiplied with the squared ratio of mean activation time and mean ISI $R_1^2 = R_a^2(\langle t_a\rangle/\langle T\rangle)^2$ (thin solid line, always decreasing with growing noise) and the CV of the excursion time multiplied with the squared ratio of mean excursion time and mean ISI $R_2^2 = R_e^2(\langle t_e\rangle/\langle T\rangle)^2$ (dashed line, increasing with growing noise). The sum (thick line) attains a minimum where both terms are still small.

induced oscillations are mainly determined by the rather regular excursion time and may thus look regular itself. In general, the effect is the more pronounced the larger the ratio between excursion and activation time is at moderate noise.

From the point of view of dynamical systems there is another explanation of the effect of coherence resonance [50]. All models introduced above possess also other dynamical regimes than the excitable one. In the LIF model, for instance, a base current above threshold ($\mu > v_T$) will generate a periodic firing of the model neuron. In the FN model, a value of parameter b such that the nullclines intersect on the middle unstable branch of the cubic nullcline will lead to a limit cycle system that generates spikes in the voltage variable also for vanishing noise. Finally, a supracritical tilt ($F > 1$ in case of a cosine potential) for the phase model will lead to sustained firing. The parameters μ, b and F play the role of control parameters. Upon variation of these parameters, the deterministic systems ($D = 0$) undergo a bifurcation from an excitable regime to an oscillatory regime. With noise perturbations the power spectrum of the system will possess a peak which is characteristic for the oscillatory regime even before a bifurcation will actually occur. Due to the nonlinearity of the respective system, this precursor emerges only for a finite range of noise intensities. A strong noise results in most systems just in a noisy output and thus spoils more sensitive features of the dynamics.

3.2.5. Limitation of the coefficient of variation as a measure of coherence resonance

We have used the CV to explain the mechanism of coherence resonance. Although certainly illustrative, the use of the CV as the only measure of coherence can be somewhat misleading. There are cases where the CV does not show a minimum but nevertheless the coherence is maximized at finite noise intensity. In those cases, the CV fails as an indicator of coherence resonance. For instance, the normal form of type I excitability shows only a decreasing CV saturating at $1/\sqrt{3}$ at large noise [254], whereas two-dimensional type I excitable dynamics displays a coherence resonance at finite noise intensity, if quantified for instance by the spectral coherence [47,266]. This is due to the destruction of the spike shape in the strong noise limit—a feature that cannot be described by a measure that is based only on the intervals between spikes.

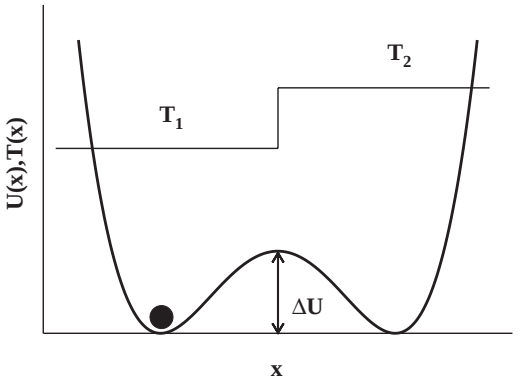

Fig. 25. Brownian particle in double well potential with different temperatures. For weak noise the interwell motion of the particle can be associated with a two-state process. The corresponding transition rates r_1 and r_2 depend monotonously on the temperatures T_1 and T_2, respectively.

Conversely, it is possible that the CV exhibits a minimum without significant coherence, i.e. at the noise level in question other indicators of coherence do not show minimal or maximal values. Shuai et al. [310] discuss a threshold spike generator with doubly filtered white noise input that shows a CV dropping with increasing noise but does not possess a peaked power spectrum. Another simple example [244] is a two-state process $\sigma(t) \in \{-1, 1\}$ with Poissonian jumps where one of the rates (r_1) is kept fixed while the other rate (r_2) is varied (Fig. 25 shows a bistable dynamics that is approximated by such a two-state process). This system is not excitable. We may, however, obtain a spike generator as follows: every transition $\sigma = -1 \to 1$ defines a spiking time; thus the interspike intervals are given by the intervals separating two subsequent transitions from $\sigma = -1 \to 1$. Because of the independent Poissonian statistics of the single transitions, the CV is given by

$$R = \frac{\sqrt{r_1^2 + r_2^2}}{r_1 + r_2} \ . \tag{43}$$

Suppose the rate r_2 can be changed from 0 to infinity (e.g. by changing the temperature T_2 in the system depicted in Fig. 25). Then the CV obviously tends to 1 in both limit cases $r_2 \to 0$ and $r_2 \to \infty$, while it attains a minimum if the rates are equal

$$\frac{\mathrm{d}R}{\mathrm{d}r_2} = 0 \Rightarrow r_2 = r_1 \rightsquigarrow R_{\min} = 1/\sqrt{2} \ . \tag{44}$$

Thus, we have tuned the "noise intensity" (rate r_2 or equivalently temperature T_2) such that the system is symmetric, and obtained a minimum in R. But the symmetric system in the two-state approximation described above corresponds to one of the standard stochastic processes, namely the random telegraph noise, commonly looked upon as a rather irregular process. This process possesses a diffusion coefficient monotonously increasing with r_2 and a Lorentzian spectrum (i.e. with no peak at finite frequency) that is independent of r_2. Thus, despite the CV exhibits a minimum, further indications of a coherence resonance are absent. Consequently, a mere minimum of the CV vs noise intensity does not necessarily indicate a noise-induced eigenfrequency, and such a minimum can be at most considered as a weak form of coherence resonance.

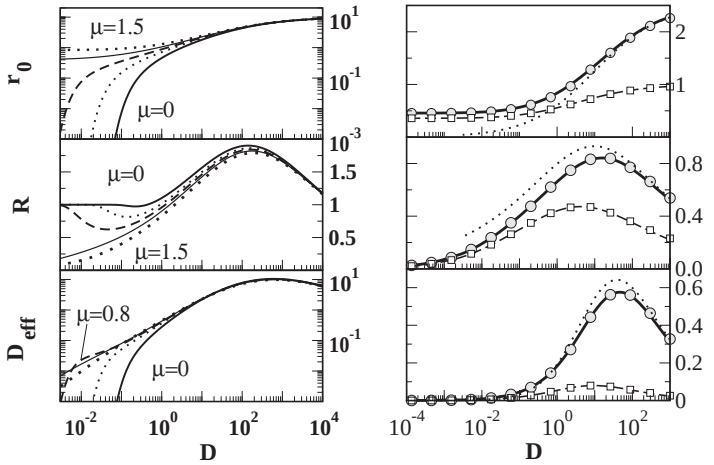

Fig. 26. Analytical results for rate, coefficient of variation, and spike-count diffusion coefficient vs noise intensity for finite τ_{abs}. Left: $\tau_{abs} = 0.1$, μ is varied: 0 (solid), 0.5 (dotted), 0.8 (dashed), 1.1 (thin solid), 1.5 (thick dotted). Right: $\mu = 1.2$, $\tau_{abs} = 0.4$ (solid) and $\tau_{abs} = 1$ (dashed) compared to numerical simulation results (circles and squares), dotted lines give the strong noise expressions according to Eq. (45) for $\tau_{abs} = 0.4$.

3.2.6. Incoherence maximization in the leaky integrate-and-fire model

Here we show, within the framework of the leaky integrate-and-fire model with absolute refractory period, that the effect of a maximal spike train incoherence can be observed. This is the opposite effect to coherence resonance, and may be relevant in situations where an asynchronous firing pattern is more desirable than coherent firing like, for instance in the case of Parkinson disease [311,312].

As mentioned above, the LIF model is characterized by three different time scales: the passage of the voltage variable from reset value to the resting voltage, the escape from the resting state to threshold, and the absolute refractory period τ_{abs}. For coherence resonance, the third time scale is not essential since its presence leads in any case to a more pronounced coherence irrespective of the noise intensity. However, the absolute refractory period determines the regularity of the spike train in the strong noise limit. For $D \to \infty$, both escape time and relative refractory period approaching zero, leaving τ_{abs} as the dominant time and thus the interspike intervals will be narrowly distributed around τ_{abs}. For the parameters used in the previous subsection, this takes place for a huge amount of noise. For larger values of τ_{abs} (compared to the other two time scales), however, this can be seen at high but still realistic noise levels. Considering now a LIF model with supra-threshold base current μ ($\mu > v_T$), we expect perfectly regular spiking for vanishing noise ($D = 0$) but also in the large noise limit ($D \to \infty$). For finite noise intensity, the spiking is irregular. Put differently, by tuning the noise intensity, we may maximize the irregularity or incoherence of the spike train. Consequently, maxima in the CV and in the diffusion coefficient of the spike count as functions of D should be observable, while the power spectrum of the spike train should be flat with respect to frequency for an intermediate value of the noise intensity.

As demonstrated in Figs. 26 and 27, this is indeed the case. The CV and D_{eff} pass through maxima as functions of noise intensity. Location and height of these maxima are largely independent of the base current μ. This is also found in a large-D approximation for rate and CV [57] (assuming also

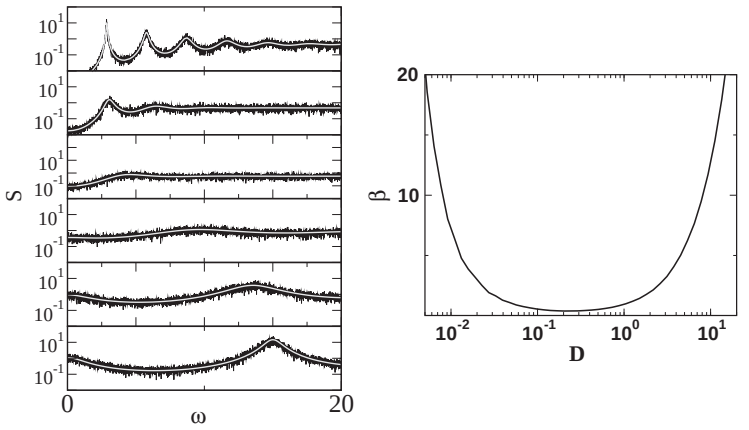

Fig. 27. Left: power spectra in the deterministic firing regime for different noise intensities. Right: spectral coherence as a function of noise intensity at $\mu = 1.2$, $\tau_{\rm abs} = 0.4$. Left (from top to bottom): $D = 10^{-3},\ 10^{-2}, 10^{-1}, 10^{0}, 10^{1}, 10^{2}$, theory (grey) according to Eq. (37) compared to simulations (black).

small values of $\tau_{\rm abs}$)

$$r_0 \approx 1/\left[\tau_{\rm abs} + \sqrt{\pi}/\sqrt{2D}\right] ,$$

$$R \approx \sqrt{c_1}\,\frac{(2D)^{1/4}}{1+\tau_{\rm abs}\sqrt{2D/\pi}} ,$$

$$D_{\rm eff} \approx c_1\,\frac{D/\sqrt{\pi}}{\left(1+\tau_{\rm abs}\sqrt{2D/\pi}\right)^3} \tag{45}$$

(here $c_1 \approx 0.782$) that yield the approximate values of D which maximize R and $D_{\rm eff}$, respectively

$$D_{R_{\rm max}} \approx \pi/(2\tau_{\rm abs}^2), \quad D_{D_{\rm eff}\,\rm max} \approx 2\pi/\tau_{\rm abs}^2 = 4D_{\rm Rmax} . \tag{46}$$

Thus, the positions of the maxima are mainly determined by the absolute refractory period $\tau_{\rm abs}$.

The power spectra shown in Fig. 27 reveal the same effect. At small and at large noise intensities they are sharply peaked either at the deterministic eigenfrequency or at the inverse of the absolute refractory period $2\pi/\tau_{\rm abs}$ (in either case also peaks at higher harmonics are present). Remarkably, the degree of coherence shows a minimum which appears, however, at a significantly lower noise level than the maxima in $R(D)$ and $D_{\rm eff}(D)$. Thus the regularity induced by the absolute refractory period is present in the spectral measure at a much smaller noise intensity (for a discussion of this effect, see [57]).

An incoherence maximization can be observed also in the case of subthreshold base current if the absolute refractory period is sufficiently small [57]. In this case, the CV passes first through a minimum (coherence resonance) and then through a maximum (incoherence maximization). For larger values of $\tau_{\rm abs}$, the coherence is always enhanced by increasing the noise intensity, for instance, the CV will drop in this case from the Poissonian limit ($CV \to 1$ as $D \to 0$) to the large noise limit ($CV = 0$ as $D \to \infty$).

3.3. Stochastic resonance

We now turn to the dynamics of an excitable system that is driven by noise and a periodic signal $s(t) = \varepsilon \cos(\Omega t)$. If the periodic driving is strong, the excitable dynamics will follow this forcing, i.e. the occurrence of a spike will be correlated to the signal phase. In the FitzHugh–Nagumo system, for instance, this can be easily understood for very slow driving (adiabatic case, $\Omega \ll 1$), where the signal enters effectively as a static modification of the x nullcline. A positive signal ($s(t) > 0$) shifts the nullcline such that the fixed point is on the middle branch of $f(x)$. In this case the system exhibits an oscillatory (limit cycle) behavior. This implies sustained firings of the system even in the absence of noise. During the second half period, the signal will be negative and the nullcline is shifted in opposite direction. As a result the system will be even less excitable than in the absence of a signal. Since noise is present, the exact location of spikes is still random, but the probability of a firing depends on the signal.

For moderate amplitude and finite frequency (nonadiabatic case), one observes different phase locking patterns [313]. In contrast, small-amplitude signals cannot elucidate activations, but only small oscillations around the resting state. With the help of noise, spikes may be nevertheless generated and will be correlated to the weak signal. This is the basis of stochastic resonance in excitable systems.

Let us now turn to the case of a weak periodic signal. As is well known from the literature [109,104,105], in this case stochastic resonance (SR) can be found, i.e. the output of the excitable system is most strongly correlated to the periodic input at a *finite* intensity of the applied noise. This behavior becomes evident in the power spectrum of the output, which consists of a noisy background spectrum, as discussed in the previous sections, and superimposed peaks at the driving frequency and its higher harmonics. An indication of SR is that the weight of the signal peak as well as its ratio to the background spectrum (signal-to-noise ratio, SNR) pass through maxima as functions of noise intensity. This happens not only for the usual case of additive periodic driving, but can also be found for a noise-coded signal. A distinct feature of the latter kind of signal is a high frequency response, i.e. if the excitable system is driven by a noise-coded signal, the measures of signal transmission saturate at finite values in the limit of large driving frequency.

The SR features of the FN and LIF models have been the subject of simulation studies [104–106,269] and sophisticated numerical treatment [113,242]. Adiabatic approximations neglecting the internal dynamics of the systems have been proposed in [105,106]. Here we focus on a nonadiabatic theory for the FN model [110] and the LIF model [112] developed more recently.

3.3.1. Stochastic resonance in the FitzHugh–Nagumo model

We first consider the case of weak periodic stimulation in the FN model, setting $s(t) = \epsilon \cos(\Omega t)$ in Eq. (1). One may apply such a forcing to either the dynamics of the voltage or the recovery variable, yielding only minor differences [110]. Here we choose to apply the forcing in the second equation, i.e.

$$\begin{aligned} \varepsilon \dot{x} &= f(x) - y \ , \\ \dot{y} &= \gamma x - y + b + \varepsilon \cos(\Omega t) + \sqrt{2D}\xi(t) \ . \end{aligned} \tag{47}$$

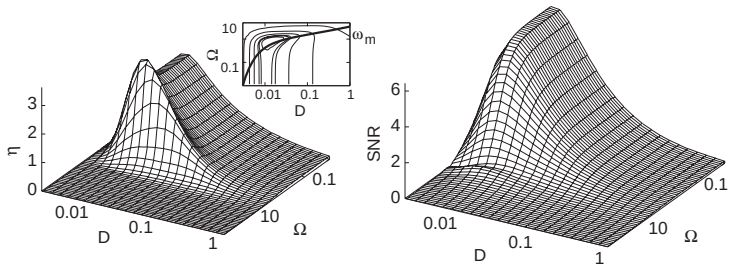

Fig. 28. Spectral amplification (left) and spectral SNR (right) vs rescaled noise intensity and driving frequency for the FN model. Inset: contour lines of the amplification compared to the mean frequency that is drawn as a function of the noise intensity. Parameters: $\gamma = 1$, $b = 0.4$.

We choose again $f(x)$ according to Eq. (3), and consider the limit of a perfect time scale separation ($\varepsilon \to 0$). The linear response to the periodic stimulation may be expressed by the spectral power amplification [272] with respect to the discretized voltage variable Eq. (24). This function is given by the ratio of output and input signal intensity and reads [110,244].

$$\eta = \frac{4r_0^2}{D}\,\frac{1}{(1+\gamma)^2(1+\Omega^2)} \times \left| \frac{(\mathrm{e}^{\Delta y}\psi_{y+} - \psi_{y-})(\mathrm{e}^{\Delta x}\Phi_{x+} - \Phi_{x-}) + (\mathrm{e}^{\Delta y}\Phi_{y+} - \Phi_{y-})(\mathrm{e}^{\Delta x}\psi_{x+} - \psi_{x-})}{\mathrm{e}^{\Delta x}\mathrm{e}^{\Delta y}\psi_{x+}\psi_{y+} - \psi_{x-}\psi_{y-}} \right|^2 \tag{48}$$

with

$$\psi_{x_\pm} = \mathscr{D}_{i,\Omega}\left(\frac{x_\pm}{\sqrt{D}}\right), \quad \psi_{y_\pm} = \mathscr{D}_{i,\Omega}\left(\frac{y_\pm}{\sqrt{D}}\right), \quad \Phi_{x\pm} = \mathscr{D}_{i,\Omega-1}\left(\frac{x_\pm}{\sqrt{D}}\right),$$

$$\Phi_{y\pm} = \mathscr{D}_{i,\Omega-1}\left(\frac{y_\pm}{\sqrt{D}}\right), \quad \Delta x = (x_+^2 - x_-^2)/(4D), \quad \Delta y = (y_+^2 - y_-^2)/(4D),$$

where $x_\pm$ and $y_\pm$ are given by Eq. (34), and time, frequency and noise intensity are rescaled according to $t \to t/(1+\gamma)$, $\Omega \to \Omega(1+\gamma)$, and $D \to D(1+\gamma)$, respectively. The SNR can be determined from Eq. (25) using the spectrum of the unperturbed system Eq. (32) as the background spectrum (this is valid only as long as the linear response approximation holds).

In contrast to approximations assuming small noise intensity (employing Kramers rate) or small frequencies (quasistatic, i.e. "adiabatic" approaches), the results given above hold true for arbitrary driving frequency and noise intensity. In Fig. 28 (left) the amplification and SNR are shown as functions of noise intensity and driving frequency. The first feature that becomes apparent in this plot is stochastic resonance, i.e. a maximum of η as well as SNR vs noise intensity for arbitrary but fixed frequency. The reason for this resonance can be easily understood by considering the limits of vanishing and infinite noise intensity: at $D = 0$ the subthreshold signal cannot evoke any spiking response in the neuronal dynamics, therefore $\eta = 0$; at large noise intensity the FN neuron will fire at a high rate, however the weak signal will have vanishing influence on this firing rate as D tends

to infinity. For a moderate level of noise, the firing depends on an effective threshold that in turn depends on the signal phase. In this case one can expect a finite correlation between firing events and signal phase, i.e. between output and input signal.

The second feature of Fig. 28 (left) is a pronounced maximum of the amplification with respect to the driving frequency that is seemingly independent of the stochastic resonance observed. What is the reason for this maximum? As we have seen in the previous sections, noise alone may induce a regularity of the neuronal output already in the absence of periodic driving, reflected by noise-induced eigenfrequency that appears in the power spectrum. If the signal frequency matches this eigenfrequency, a classic resonance can be expected. This is indeed the reason for the maximum of the spectral power amplification, as can be seen by comparing the contour lines in the inset of Fig. 28 with those of the spectrum in absence of a signal (Fig. 17, inset). The maximum in spectral amplification appears roughly within the same region of the Ω–D plane where coherence resonance is indicated by a peak of the spectrum in the ω–D plane.

Since the spectral amplification is maximized at finite D and finite ω the effect has been called stochastic double resonance by Plesser and Geisel [113], who found the same effect numerically in the leaky integrate-and-fire neuron model.

It is easy to understand why this resonance cannot be observed in the signal-to-noise ratio (Fig. 28, right). Since the SPA and the background spectrum show the same resonance, the maxima vs frequency cancel each other like in the case of a periodically driven noisy harmonic oscillator, for which the same behavior in the SNR is observed [314]. Remarkably, due to the nonlinearity of the excitable system a weak nonmonotonous behavior is nevertheless found at high frequencies, which results from the different dependence of amplification and background spectrum in this parameter region. Note, however, that the response in this region is quite weak compared to the adiabatic ($\Omega \to 0$) case.

3.3.2. Stochastic resonance in the leaky integrate-and-fire model

Like in the FN model, a periodic signal $s(t)$ may induce periodic firing in the LIF model if the signal amplitude is sufficiently strong. This is plausible for a slow signal the amplitude of which is larger than $|\mu - v_T|$: at positive signal phase the effective resting level is above threshold and the threshold is therefore reached in a finite time; at negative signal phase the effective resting level is even smaller than in the absence of a signal, and hence spikes are unlikely to occur.

In the following we focus on the case of weak signals that can evoke firings only by the assistance of noise. Intuitively it is evident, that the correlation between spike train and input signal is finite only at a *finite* noise level—again stochastic resonance can be observed in this model.

The effect of stochastic double resonance can be also found in the leaky integrate-and-fire neuron by means of analytical results [112]. Including a weak periodic forcing in the LIF model, the dynamics reads

$$\dot{v} = -v + \mu + \varepsilon \cos(\Omega t) + \sqrt{2D}\xi(t) \ . \tag{49}$$

The mean value of the output (i.e. the instantaneous firing rate) depends now explicitly on time due to the presence of the signal, according to Eq. (22). The response amplitude α (recall that the output firing rate is periodically modulated with the amplitude $\epsilon\alpha$) can be calculated by means of

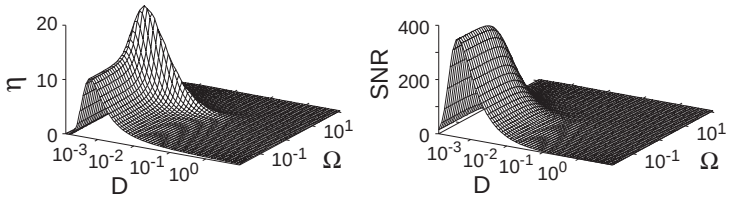

Fig. 29. Spectral amplification and signal-to-noise ratio vs noise strength and driving frequency for the LIF model with $\mu = 0.95$.

linear response theory [112,244]

$$\alpha = \frac{r_0 \mathrm{i}\Omega/\sqrt{D}}{\mathrm{i}\Omega - 1} \frac{\mathscr{D}_{\mathrm{i}\Omega-1}\left(\frac{\mu-v_T}{\sqrt{D}}\right) - \mathrm{e}^{\Delta}\mathscr{D}_{\mathrm{i}\Omega-1}\left(\frac{\mu-v_R}{\sqrt{D}}\right)}{\mathscr{D}_{\mathrm{i}\Omega}\left(\frac{\mu-v_T}{\sqrt{D}}\right) - \mathrm{e}^{\Delta}\mathrm{e}^{\mathrm{i}\Omega\tau}\mathscr{D}_{\mathrm{i}\Omega}\left(\frac{\mu-v_R}{\sqrt{D}}\right)} \,.$$

Given the signal dependent part of the mean output, we can readily calculate the spectral amplification and the signal-to-noise ratio by means of Eqs. (24) and (25), where the background spectrum is given (in linear response) by the spectrum in the absence of the periodic signal [Eq. (37)].

Spectral amplification and SNR for the LIF neuron are shown in Fig. 29. Again, a nonmonotonous dependence on frequency and noise strength can be found in the spectral amplification, but not in the signal-to-noise ratio. The overall maximum appears again within the region where coherence resonance is most pronounced, providing evidence that—like in the FN model—the effect is due to a classic resonance with the noise-induced eigenfrequency (see also Ref. [244]).

The nonmonotonous dependence on the driving frequency may have some functional relevance in real neurons, as proposed by Plesser and Geisel [113]. The transfer characteristics demonstrated in the stochastic neuron models indicates that a neuron may operate as a bandpass filter for subthreshold signals. Most notably, both the stochastic resonance feature and the resonance with respect to frequency are purely noise-induced effects, and provide in this way a possible explanation for the high degree of "variability" (or simply, noise) observed in real neuronal systems.

Finally we would like to mention some findings by Brunel and coworkers [243], who studied the LIF response to periodic stimulation in the presence of a colored noise, instead of the white noise considered above. A colored noise like the Ornstein–Uhlenbeck process is a more realistic model of the actual input to the point neuron, since the typical input (a superposition of many random spike trains) is low pass filtered by the synaptic dynamics. Brunel et al. [243] found that at moderate correlation time of the noise the LIF shows a finite high-frequency transmission (HFT), i.e. for a colored noise the response amplitude α saturates at a finite level. In cases where the driving noise is too close to the white noise limit (e.g. for input transmitted through fast $GABA_A$ synapses), another possibility to realize a finite HFT is a noise coded signal, as we will show in the next subsection.

3.3.3. Stochastic resonance for a noise-coded signal in the leaky integrate-and-fire model

In the introduction of the LIF model (Section 2.4) we have seen that there is evidence for the presence of a noise-coded signal that modulates the intensity of the input fluctuations. If both additive and noise-coded signals are present, the LIF dynamics is given by Eq. (8), which we rewrite here

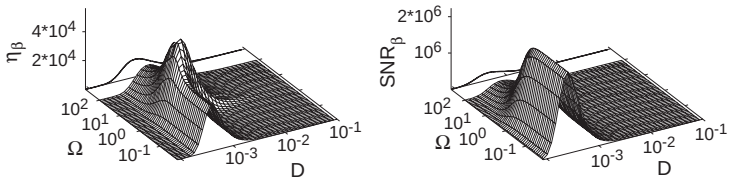

Fig. 30. Spectral amplification and signal-to-noise ratio for $\mu = 0.95$ vs noise strength and driving frequency for the LIF model and a noise-coded signal.

again for the sake of convenience:

$$\dot{v} = -v + \mu + \varepsilon_\alpha \cos(\Omega t) + \sqrt{2[D + \varepsilon_\beta \cos(\Omega t)]}\xi(t) \ . \tag{50}$$

We recall that the noise intensity contains contributions from the neuronal background and from the input population of neurons, which also generate signals. This setup raises the question of whether the transmission of a noise-coded signal (i.e. $\varepsilon_\beta \cos(\Omega t)$) can be enhanced by increasing the constant noise intensity D through an increase of the background noise intensity.

For a system with two input signals, the linear response of the firing rate is

$$\langle \sigma(t) \rangle = r(t) = r_0 + \varepsilon_\alpha |\alpha| \cos(\Omega t - \phi_\alpha) + \varepsilon_\beta |\beta| \cos(\Omega t - \phi_\beta) \tag{51}$$

which leads to the following spectral response

$$S(\Omega) = S_{\rm bg}(\Omega) + \frac{\pi}{2}(\varepsilon_\alpha^2 |\alpha|^2 + \varepsilon_\beta^2 |\beta|^2 + 2\varepsilon_\alpha \varepsilon_\beta |\alpha||\beta| \cos(\phi_\alpha - \phi_\beta)) \times [\delta(\omega - \Omega) + \delta(\omega + \Omega)] \ . \tag{52}$$

The function α was already given in Eq. (50), while β is given by [112]

$$\beta = \frac{r_0 \mathrm{i}\Omega(\mathrm{i}\Omega - 1)}{D(2 - \mathrm{i}\Omega)} \frac{\mathscr{D}_{\mathrm{i}\Omega - 2}\left(\frac{\mu - v_T}{\sqrt{D}}\right) - \mathrm{e}^{\Delta} \mathscr{D}_{\mathrm{i}\Omega - 2}\left(\frac{\mu - v_R}{\sqrt{D}}\right)}{\mathscr{D}_{\mathrm{i}\Omega}\left(\frac{\mu - v_T}{\sqrt{D}}\right) - \mathrm{e}^{\Delta} \mathrm{e}^{\mathrm{i}\Omega\tau} \mathscr{D}_{\mathrm{i}\Omega}\left(\frac{\mu - v_R}{\sqrt{D}}\right)} \ , \tag{53}$$

$$\Delta = \frac{v_R^2 - v_T^2 + 2\mu(v_T - v_R)}{4D} \ .$$

Note that the prefactor of the δ functions now also depends on the difference of the phase shifts that are given by the complex phases of α and β

$$\phi_\alpha = \arg(\alpha), \quad \phi_\beta = \arg(\beta) \ . \tag{54}$$

Let us first consider the response to a purely noise-coded signal (ε_α=0) and compare it to the response to an additive signal, which was the subject of the previous section. If only the noise-coded signal is present, the spectral power amplification and signal-to-noise ratio of this signal are given by [4]

$$\eta_\beta = |\beta|^2, \quad SNR_\beta = |\beta|^2 / S_{\rm bg} \tag{55}$$

in exact analogy to the additive case.

Both functions are shown in Fig. 30 for a subthreshold driving in the noise-induced firing regime, but close to the bifurcation point ($\mu = 0.95$). A number of interesting features arise. First of all,

[4] Here we consider $\varepsilon_\beta \cos(\Omega t)$ as the input signal and not the product of the noise and the periodic signal.

stochastic resonance can be also observed with respect to a noise-coded signal. Both SPA and SNR are nonmonotonous functions of the noise intensity, and show clear peaks for any driving frequency, although at different noise levels. The reason for this kind of stochastic resonance is similar to the additive case: at small noise intensity D, spikes occur very rarely (the neuron operates in the subthreshold firing regime and does not fire at all without noise), and modulation of the small spike rate will be weak as well. At moderate noise, the spike rate is larger and also its modulation becomes noticeable. In the strong noise limit, the weak modulation of the input noise has no effect anymore, therefore the output power and the SNR drop again.

The second feature we encounter is that the LIF neuron driven by a noise-coded signal shows stochastic double resonance, i.e. the global maximum of the SPA is at finite noise intensity as well as at finite driving frequency. The nonmonotonous dependence on the driving frequency is again due to an ordinary resonance with the noise-induced eigenfrequency, which is itself due to coherence resonance. As a consequence, the SNR (which is the ratio of SPA to the background spectrum) does not show the resonance, since the resonances seen in SPA and background spectrum cancel each other. Hence, an LIF neuron can act as a bandpass filter not only for subthreshold additive signals, but also for noise-coded signals.

The third remarkable characteristic of Fig. 30 is a finite high-frequency transmission (HFT), i.e. neither SPA nor SNR drop in the limit $\Omega \to \infty$, but both reach finite limiting curves given by

$$\eta_\beta(\Omega \to \infty) \approx \frac{r_0^2}{D^2}, \quad \mathrm{SNR}_\beta(\Omega \to \infty) \approx \frac{r_0}{D^2} \ . \tag{56}$$

These functions, which only involve the stationary firing rate of a white-noise driven LIF neuron [inverse of the mean ISI given in Eq. (35)] exhibit the SR effect, too. As pointed out in Ref. [112] HFT of noise-coded signals is associated with a *fast* signal transmission of transient noise-coded signals (the latter effect has been first discussed in Ref. [315]). Physical limitations for the transmission of very high frequencies exist, though: (1) the fire-and-reset condition in the LIF model is only an approximation that replaces the action of certain fast variables in more realistic neuron models; (2) in order to extract a fast signal, population averaging of the spike rate requires an increasing number of neurons if we go to higher and higher frequencies. Estimates of an upper bound of the frequency can be made [244] revealing that the frequency range of noise-coded signals may be two orders of magnitude higher than that of additive signals. Thus, white Gaussian noise can act as an efficient signal carrier in the LIF model.

Finally, we take a look at the response of the LIF when both kinds of stimuli are present. Here we restrict ourselves to the total output power, i.e. the integral over the δ function in Eq. (52), and show the dependence on driving frequency only. We have tuned the input amplitudes ε_α and ε_β in such a way that both signals yield comparable single responses. Two important observations can be made: (1) the result for the presence of both signals (nicely confirmed by computer simulations) is significantly larger than the mere sum of the single responses (this sum is shown by a thick line); (2) for the chosen value of the base current ($\mu = 0.8$) the nonmonotonous frequency dependence of the single responses is weak, whereas the resonance for the full response is much more pronounced. Both findings can be understood by the phase shifts that enter Eq. (52). The difference between the phase shifts is never larger than π, and furthermore contributes its own dependence on the driving frequency (see Ref. [244] for further details) (Fig. 31).

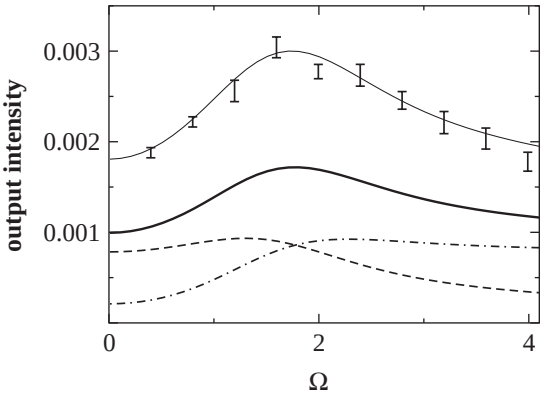

Fig. 31. Output signal intensity in presence of additive and noise-coded signal versus driving frequency for $\mu = 0.8$, $\epsilon_\alpha = 0.022$, $\epsilon_\beta = 0.002$, and $D = 0.02$. Theory [prefactors of the δ spikes in Eq. (52) shown by the thin solid line] compared to results of a numerical simulation (error bars) with $N = 200$, $T = 2000$, $\Delta t = 10^{-5}$–10^{-2}. Additionally shown are the individual responses to either only the noise-coded (dot-dashed line) or only the additive signal (dashed line). The thick line indicates the sum of the single responses.

4. Coherence and stochastic resonance in applications

As mentioned previously, coherence resonance can be found in many theoretical models and has been verified in many different experimental situations. Here we consider in detail two applications of stochastic excitable dynamics, the first one in cell biology and the second one in laser physics.

4.1. Clusters of stochastic calcium channels

Calcium plays an important role as an intra- and inter-cellular messenger in all types of cells and tissues. The release of free intracellular calcium concentration from calcium stores, e.g. the endoplasmatic reticulum (ER), is gated by ion channels. In several types of tissues, e.g. neuronal tissue and smooth muscles, these channels belong to the family of inositol-(1,4,5)-triphosphate receptor (IP_3R) channels. For models of channel dynamics see, for example, Refs. [316,317].

In the following we show that a channel clusters are governed by excitable dynamics. The role of the activator is played by the intracellular calcium concentration, which we assume globally distributed through the cluster. As a second time-dependent variable we identify the concentration of open channels in the cluster. Stochasticity comes into play if we consider a finite number of channels in the cluster [318]. Such a population of ion channels creates a common noise [319]. In the case of small number of channels, the stochasticity of their opening and closing events becomes dominant, whereas for large channel numbers this influence shrinks. Hence, a certain finite number of channels inducing a optimal common level of noise might be the origin of stochastic oscillations in this excitable system [319]. The situation can be interpreted as a case of finite system coherence resonance [320–322]. Finite-size effects in channel dynamics were also considered in Refs. [73,74,126,67,323]. We also note that wave propagation [324–327] and nucleation [328,329] in those

stochastic systems (with local coupling and taking into account the distribution of clusters across the membrane [330]) has attracted much attention.

We now aim to calculate analytically the power spectrum of the dynamics following ideas outlined in the previous Section [75]. The results will reveal collective stochastic calcium oscillations of clustered IP3 release channels which were first obtained in Ref. [319] by numerical analysis and have been confirmed in Ref. [75] by means of analytic approximations.

One single channel is composed of four homolog subunits, each of which is activated by IP_3 and shows a bell-shaped activation dependence on the calcium concentration [331]. Thus, calcium induces and limits its own release. De Young et al. [332] incorporated this into an eight-state model with three different receptors, assuming that the subunit is activated if the first two receptors are occupied by calcium and IP_3, but the third one is unoccupied. Later, a reduced two-state system was developed by Li and Rinzel, in which only the dynamics of the third slow receptor was made explicit [333,334].

We now apply the Li–Rinzel model to a single cluster of N subunits, i.e. $N/4$ channels. The channel interaction is assumed to be instantaneous via the spatially homogeneous calcium concentration $c = [Ca^{2+}]$, which is assumed to be realized by fast intracellular calcium diffusion. One channel is open if at least three out of four subunits are in the activated state [335],

$$P_{\text{open}} = x^4 + 4x^3(1-x), \quad x = \frac{pc(1-y)}{(p+K_1)(c+K_5)} , \tag{57}$$

where y is the probability of the subunit being calcium-inactive, and $p = [IP_3]$ is the concentration of the ligand IP_3.

If M of the N subunits are in the inactive state, a master equation for the dynamics of inactivation can be formulated:

$$\frac{\partial P(M,t)}{\partial t} = -((N-M)K^+ + MK^-)P(M,t) + (N-M+1)K^+P(M-1,t) + (M+1)K^-P(M+1,t) . \tag{58}$$

Therein the rate of inactivation $K^+(c)$ depends on the calcium concentration, since an additional calcium atom has to attach to the empty receptor. The activation process, K^-, for releasing an calcium atom is independent of c. Specifically, the rates are

$$K^+(c) = \frac{2c(K_1k_1k_4 + k_2k_4c + k_1k_2p)}{c(k_2+k_4) + 2k_1(K_1+p)} ,$$
$$K^- = \frac{2(k_{-3}k_{-4} + k_{-2}(k_{-4} + k_3p))}{k_{-2} + k_{-4} + 2k_3(K_3+p)} . \tag{59}$$

Eq. (58) can be expanded for $N \gg 1$ to give a Fokker–Planck equation, which is in turn equivalent to the following Langevin equation (with $y = M/N$) [319,336]:

$$\dot{y} = (1-y)K^+ - yK^- + \sqrt{\frac{(1-y)K^+ + yK^-}{N}}\,\xi(t) , \tag{60}$$

where $\xi(t)$ is a zero-mean, Gaussian white noise, with correlation $\langle \xi(t)\xi(t+\tau)\rangle = \delta(\tau)$. Its intensity scales inversely proportional to the channel number in the cluster (comp. also [126] for sodium and potassium channels).

The intracellular calcium concentration is determined by [324,337]

$$\dot{c} = (r_1 P_{\text{open}} + r_2)(c_{\text{ER}} - c) - r_3 \frac{c^2}{c^2 + K_p^2} \ , \tag{61}$$

where $c_{\text{ER}} = (C_0 - c)/\alpha$. The first term of this equation models the gradient-dependent influx (Ca^{2+} source), while the second term represents the activity of the SERCA-pump (Ca^{2+} sink) that re-establishes this gradient; r_1, r_2 and r_3 are channel, leak and pump fluxes, respectively, c_{ER} is the ER calcium concentration, α is the ratio of ER volume to cell volume and C_0 is a constant, representing a local condition for a fixed amount of total cell calcium; our numeric standard parameters, including the dissociation constants $K_i = k_{-i}/k_i$, are given in [338]. Most of them are taken from [332,324], some were adopted to new measurements [339], and some were slightly changed by us in order to investigate other regimes.

With the aim of finding an analytic description, we have carried out further simplifications of the model described above [75]: (i) perfect time scale separation, (ii) linear nullcline approximation, and (iii) replacement of phase-state dependent noise by additive noise, whose level is taken in the fixed point $(c^s, y^s) = (0.076\ \mu\text{M}, 0.0802)$. This defines a two-state process switching between low and high intracellular calcium concentration. Shuai et al. [319] numerically described this process and computed its spectrum. We used the results of the piecewise linear FN model to find an analytic description [75].

The spectrum for the linearized system shows the same properties as Fig. 17. Additionally, the second harmonics of the peak are present. There exists an intermediate noise level for which the degree of coherence, Eq. (18), reaches a maximum value, for the corresponding number of channels calcium signalling can be considered most regular (Fig. 33).

To prove the validity of our simplification, we performed stochastic simulations of the Li–Rinzel model. Each of the four channel subunits was treated according to that model, i.e. the process $y(t) = 0$ or 1: to decide for a transition between these two states, a uniformly distributed random number $\rho \in [0, 1]$ is drawn and, if $\rho\, \mathrm{d}t < K^{\pm}$ the subunit makes the corresponding transition. For noninhibited subunits, the probability of being in the open-state is given by Eq. (57), and the open state is set if $\rho' < x$, where ρ' is another uniform random number. A channel opens if three or four subunits are in the open-state, and the fraction of open channels N^{open}/N substitutes P_{open} in Eq. (61).

The evolution of $c(t)$ was sampled with $\mathrm{d}t = 0.01$ s for a time $T = 2621.44$ s, and the time series was then zero-averaged and fast-Fourier transformed (with 2^{18} points). In order to obtain a smooth power spectrum we averaged over 300 runs. Results are displayed in Fig. 32 (left). For a single channel (maximal noise level) the spectrum shows no peak but monotonously falls off for increasing frequencies. If the number of channels is increased, i.e. the system noise reduced, a peak emerges, reaches a maximum value and later starts to disappear again for very large clusters. Thus, the simulations show the same qualitative behavior as the reduced model shown on Fig. 32 (right). We note that the approximation given by the Langevin Eq. (60) is limited to a large numbers of channels. Therefore, results for $N = 1$ are beyond the validity of the theory.

To answer the key question—what is the optimal channel number per cluster with respect to signalling periodicity—we calculated the degree of coherence of the stochastic oscillations from Eq. (18) with $a = 2$. The comparison of analytic and stochastic calculation is given in Fig. 32 (left) and shows excellent agreement.

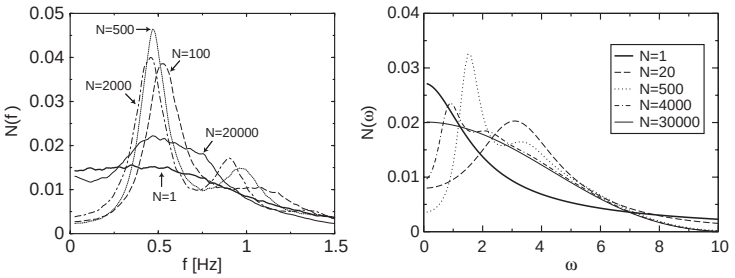

Fig. 32. Power spectra of the calcium dynamics for different numbers of subunits in the cluster (left: simulations of the Li–Rinzel model (see text), right: analytics) [75].

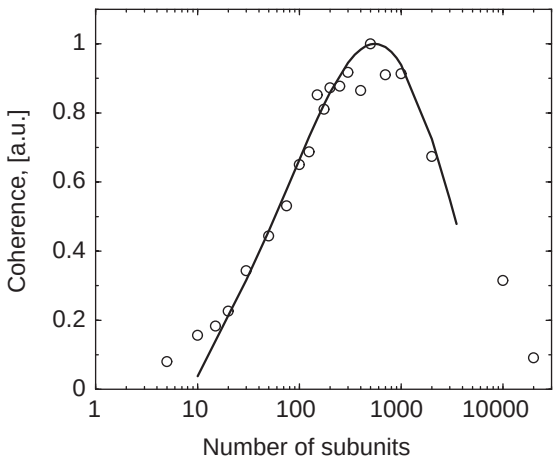

Fig. 33. Degree of coherence of the calcium dynamics with respect to the number of subunits in a cluster of calcium channels, stochastic simulation (circles) compared with analytic results (line) [75].

In [330] Shuai and Jung underline that their stochastic approach "predicts optimal signalling cellular capability at cluster sizes and distances that agree with experimentally found values in Xenophus oocyte [340–342]". In the analytic approximation we found a range of 20–750 channels per cluster optimal for signaling periodicity. The lower bound agrees with the experimental findings of about 20–50 release channels [330].

4.2. Excitable laser systems

Ever since their initial development in the 1960s, laser systems have exhibited dynamical behavior [8]. By way of example, a bistable laser offered one of the earliest and most influential experimental observations of stochastic resonance [343]. In recent years, several types of optical systems have provided clear examples of excitable behavior, among which one can find lasers with saturable absorber [344,345], passive nonlinear ring cavities [346], and lasers with injected signal [347]. Following these studies, coherence resonance was predicted theoretically in a laser with saturable absorber [70].

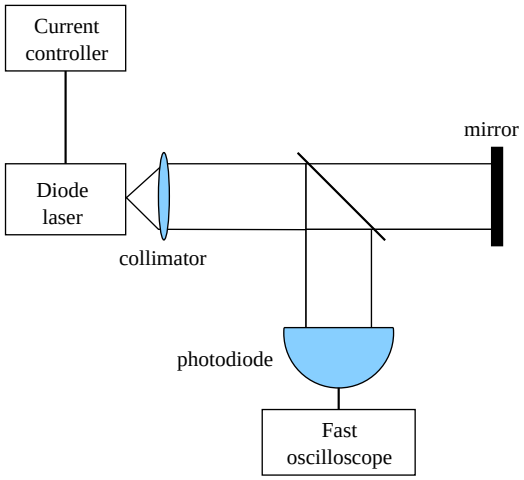

Fig. 34. Experimental setup of a semiconductor laser with optical feedback.

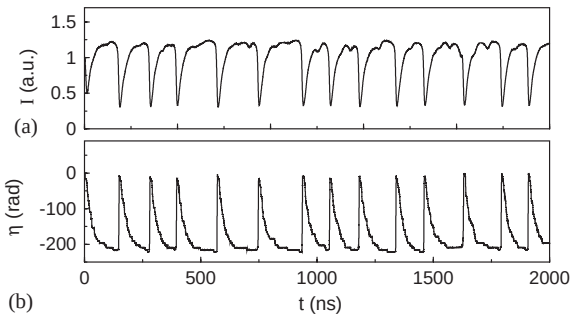

Fig. 35. Time evolution of the intensity (a) and the corresponding phase change of the electric field during the external round-trip (b) as computed numerically for a semiconductor laser with optical feedback [71]. The model used for this numerical simulation is the Lang–Kobayashi model, described below.

4.2.1. Excitable behavior in semiconductor lasers with optical feedback

Fig. 34 shows the typical experimental setup of a semiconductor laser with optical feedback, where the first experimental observation of optical coherence resonance was made [153,155,156]. Part of the light emitted by the laser, which is pumped by an electrical current, is fed back into it after reflection on an external mirror. For moderate feedback strengths and pumping current close to the emission threshold, the laser goes through a dynamical state where constant emission is interrupted at irregular times by sudden dropouts in power. A numerically computed time trace of the light intensity emitted by the laser in this regime is displayed in Fig. 35(a). This time series has been low-pass filtered (with a cut-off frequency of 100 MHz) in order to mimic the bandwidth-limited operation of photodetectors. Therefore, it only represents the envelope of a much faster dynamics consisting of short pulses with widths on the order of picoseconds [348]. Each power dropout, on other hand, corresponds to a sudden increase in the phase accumulated by the electric field as it

travels towards the external mirror and back, as shown in Fig. 35(b). This time series allows for a much easier detection of the dropout occurrence times than if the intensity time series is used (which should be filtered first).

A vast literature exists devoted to analyze the mechanism of the self-pulsed behavior described above (see for instance Ref. [349] and references therein). In particular, the system depicted in Fig. 34 has been shown, both experimentally [350] and numerically [351], to have excitable properties: when the constant pumping current of the laser is perturbed with electrical pulses over a threshold value, dropouts can be generated whose shape is basically independent of the perturbation. For larger pumping rates (but still close to the laser threshold) the intensity dropouts appear spontaneously, as described above. In the excitable regime, experiments have shown that when noise is added to the driving current of the laser, the regularity of the dropout series initially increases with growing fluctuations, and reaches a maximum for an optimal amount of noise [153], which constitutes a clear example of coherence resonance in an optical system. We now show that this situation can be modeled by means of a rate equation system including a delay term. The model used is the well-known Lang–Kobayashi (LK) model [349], which is generalized to take into account the addition of external noise into the system through the laser's pumping current.

4.2.2. Modeling the dynamics of semiconductor lasers with feedback

The LK model describes the temporal evolution of the slowly varying complex envelope of the electric field $E(t)$ inside the laser, and of the excess carrier number $N(t)$. It considers only one longitudinal mode of the solitary laser, and one single reflection from the external feedback mirror (i.e. multiple reflections are neglected, which is valid for not too large reflectivity). In dimensionless form the model reads [71]:

$$\frac{\mathrm{d}E}{\mathrm{d}t} = \frac{1+\mathrm{i}\alpha}{2}(G(E,N)-\gamma)E(t) + \kappa \mathrm{e}^{-\mathrm{i}\omega\tau_f}E(t-\tau_f) + \sqrt{2\beta N}\zeta(t)\ ,$$

$$\frac{\mathrm{d}N}{\mathrm{d}t} = \gamma_e\{C[1+\xi(t)]N_{\mathrm{th}} - N(t)\} - G(E,N)|E(t)|^2\ , \tag{62}$$

where γ and γ_e are the inverse lifetimes of photons and carriers, respectively, C is the pumping rate (directly related to the driving current; $C=1$ is the solitary-laser threshold), α is the line width enhancement factor (which couples amplitude and phase of the electric field, and is a relevant quantity in semiconductor lasers), and ω is the solitary-laser frequency. The last term in the electric-field equation represents spontaneous emission fluctuations, where $\zeta(t)$ is a Gaussian white noise of zero mean and correlation $\langle\zeta(t)\zeta(t')\rangle = \delta(t-t')$, and β measures the internal noise strength. The material-gain function $G(E,N)$ is given by

$$G(E,N) = \frac{g(N(t)-N_0)}{1+s|E(t)|^2}\ , \tag{63}$$

where g is the differential gain coefficient, s the saturation coefficient, and N_0 is the carrier number at transparency. The threshold carrier number is $N_{\mathrm{th}} = \gamma/g + N_0$. The optical feedback is described by two parameters: the feedback strength κ and the external round-trip time τ_f. Finally, the external noise is represented by the term $\xi(t)$, which cannot be considered to be white. That impossibility is due to the fast time scales in which this system evolves ($\sim$ tens of ps, as mentioned above), smaller than or on the order of the characteristic time scales of the fastest random fluctuations that

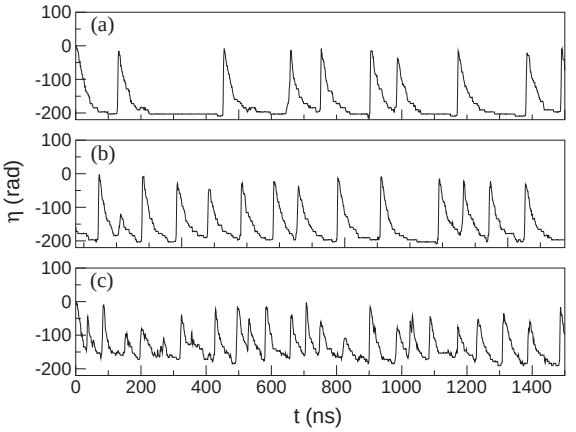

Fig. 36. Left: temporal behavior of the phase difference η for increasing noise amplitudes: (a) $\sigma = 7.36 \times 10^{-2}$, (b) $\sigma = 9.35 \times 10^{-2}$, and (c) $\sigma = 1.60 \times 10^{-1}$. The parameters used are: $C = 1.01$, $\tau_c = 24$ ps, $\gamma_e = 6 \times 10^{-4}$ ps^{-1}, $\gamma = 0.158$ ps^{-1}, $g = 2.79 \times 10^{-9}$ ps^{-1}, $s = 3 \times 10^{-7}$, $\alpha = 3.5$, $N_0 = 1.51 \times 10^{8}$, $\beta = 5 \times 10^{-10}$ ps^{-1}, $\kappa = 0.025$ ps^{-1}, $\tau_f = 2.4$ ns, $\omega\tau_f = 2$, and $D = 0$ [71].

can be experimentally introduced in the pumping current of the laser, and which are restricted by limitations of the electronics involved ($\sim$ GHz). This is the situation in the experiment reported in [153]. Following this reasoning, we assume that the external noise has a non-delta correlation in time. In particular, we consider an Ornstein–Uhlenbeck noise, Gaussian distributed with zero mean and correlation

$$\langle \xi(t)\xi(t')\rangle = \frac{D}{\tau_c}\,\mathrm{e}^{-|t-t'|/\tau_c}\ . \tag{64}$$

This external noise is characterized by two parameters, its intensity D and its correlation time τ_c. The variance of the noise is given by D/τ_c, and hence we measure its amplitude as $\sigma = \sqrt{D/\tau_c}$.

4.2.3. Optical coherence resonance

Let us now examine the effect of the external noise $\xi(t)$ on the system dynamics. Fig. 36 shows three time traces of the phase difference $\eta(t) = \phi(t) - \phi(t - \tau_f)$ (with $E(t) = \sqrt{I}\exp(\mathrm{i}\phi)$) for increasing amplitudes of the external noise, keeping its correlation time constant. In this case, the semiconductor laser is biased at 1% above the solitary-laser threshold, a situation for which the system is stable in the absence of external noise. A small amount of noise produces infrequent dropouts (Fig. 36(a)), which become more numerous and regular as the noise amplitude increases (Fig. 36(b)). For large noise strengths the pulses become increasingly irregular, both in separation and in amplitude (Fig. 36(c)). Hence, an optimal amplitude of the external noise exists for which the coherence of the pulsed output of the laser is optimal. In order to quantitatively characterize this effect, one can analyze the statistical properties of the normalized dropout separation $\theta = T/\langle T\rangle$ and normalized dropout amplitude $\mu = A/\langle A\rangle$, where T is the time interval between two consecutive dropouts, and A is the peak value of the phase difference $\eta(t)$ at a dropout, measured with respect to its minimum value between dropouts. In order to take into account both the dropout separation and amplitude simultaneously in the determination of the signals regularity, it is useful to define a joint entropy

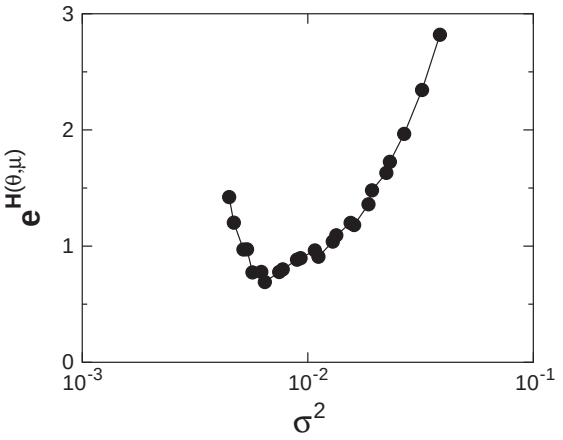

Fig. 37. Joint entropy $H(\theta,\mu)$ as a function of the external noise amplitude. Parameters as in Fig. 36 [71].

$H(\theta,\mu)$ of the two quantities, where $H=-\sum P\log P$, with P the joint probability density of the two random variables. For the case of two Gaussian independent random variables the following relation holds [153]: $\exp(H(\theta,\mu))=2\pi e R_\theta R_\mu$, where R_θ and R_μ are the standard deviations of the normalized dropout separation and amplitude, respectively. Assuming that this result is approximately valid in the present case, we plot this joint entropy in Fig. 37(d), which shows a maximum regularity of the dropout series for an optimal noise amplitude.

This resonant effect can be understood in the light of the deterministic mechanism behind the power dropouts, which is well characterized in the framework of the LK model. This model exhibits multiple coexisting fixed points, which appear in pairs of solutions called modes and antimodes. The antimodes are saddle points, and most of the modes are also unstable due to a Hopf bifurcation [352]. However, sometimes one of the modes (the one with maximum power) is stable. In this complex phase-space landscape, a large enough fluctuation may be able to take the system away from the basin of attraction of the stable fixed point and, upon collision with a neighboring antimode, produce a sudden increase in the phase difference (see Fig. 35(b)) which corresponds to a power dropout. The corresponding escape time, also called activation time t_a, is a random variable whose average decreases with the intensity of the external noise according to Kramers' law [353]. Following the dropout, a build-up process begins in which the system undergoes a chaotic itinerancy around the Hopf-unstable modes, jumping consecutively from one to the next while being drifted back towards the stable maximum-gain mode [354]. For small intensities of the external noise, the excursion time t_e required by this process is basically independent of noise, and has the role of a refractory time during which no dropouts can be induced. As noise intensity increases the escape events become more frequent, reducing the standard deviation of the interspike intervals accordingly. A minimum of variability occurs for an optimal amount of noise when the dropout separation is of the order of t_e. Beyond that point, noise intensity is large enough to produce escapes before the build-up process is finished (i.e. before the stable mode is reached), which leads to an irregular dynamics.

The value of the correlation time of the noise used in the previous results ($\tau_c = 24$ ps) is of the order of the fast time scale of the deterministic dynamics. In fact, as the white-noise limit is

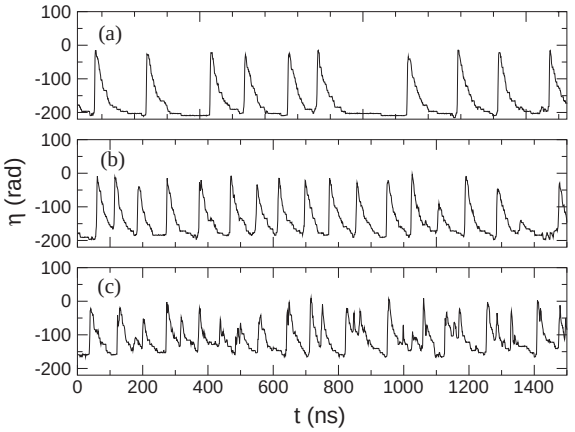

Fig. 38. Temporal behavior of the phase difference η for increasing noise correlation time: (a) $\tau_c = 15.8$ ps, (b) $\tau_c = 57.6$ ps, and (c) $\tau_c = 153.2$ ps. Noise amplitude has been taken constant, $\sigma = 0.079$, and other parameters are those of Fig. 36.

approached the amount of noise necessary to obtain similar effects climbs up to unreasonably high values. The reason is that the carrier dynamics acts as a frequency filter for the external noise [see equation for $N(t)$ in Eqs. (62)], which also prevents the system from responding to high-frequency modulations of the pump current. Therefore, most of the power of a white noise has no effect upon the system dynamics, and the noise intensity needs to be very large in order to have a noticeable influence. In the opposite frequency limit a similar situation occurs: for low-frequency forcing the carrier dynamics has enough time to follow the modulation, and the system responds simply with a modulated output. Only for intermediate frequencies will the external forcing be able to influence the dropout statistics and enhance the coherent response of the system. In order to verify this conjecture, we now fix the amplitude $\sigma = \sqrt{D/\tau_c}$ of the external noise and analyze the behavior of the system for an increasing correlation time of the Ornstein–Uhlenbeck noise. The result is shown in Fig. 38 (a–c) for three different values of τ_c. It can be seen that the regularity of the pulsed time series is maximal for intermediate values of the noise correlation time. This resonant effect is quantified by means of the joint entropy $H(\theta, \mu)$ defined above, as plotted in Fig. 39(d). This behavior can be interpreted as a resonance with the fast deterministic dynamics of the system, and has not been observed so far experimentally. A similar resonance has been observed experimentally in a chemical excitable medium [196].

4.2.4. Stochastic resonance in an excitable laser system

We have seen that external noise in the pumping current is able to enhance the regularity of the dropout time series emitted by the laser, extracting an internal time scale defined by the characteristic excursion time mentioned above. But noise in this experimental setup can also enhance the response of the laser to an external harmonic driving, in a sort of stochastic resonant effect. In order to show this effect, we now include in Eq. (62) a pumping current of the form $C(t) = C_0[1 + \xi(t) + A\sin(\Omega t)]$, where C_0 is the bias pumping rate, $\xi(t)$ represents again the external Ornstein–Uhlenbeck noise and the harmonic driving has amplitude A and frequency Ω. In Fig. 40 we show the numerically computed intensity and phase difference time traces, and the corresponding probability distribution functions

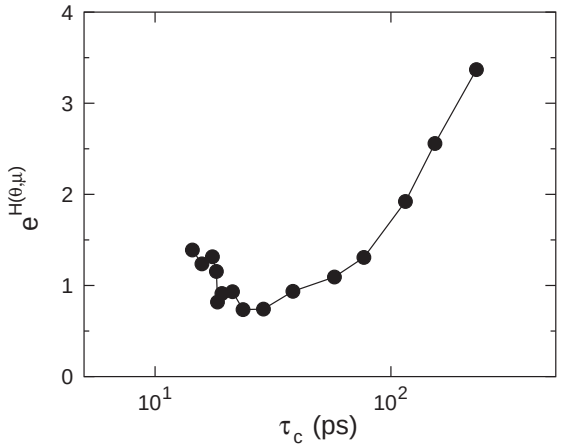

Fig. 39. Joint entropy $H(\theta,\mu)$ as a function of the noise correlation time [71]. Parameters are those of Fig. 38.

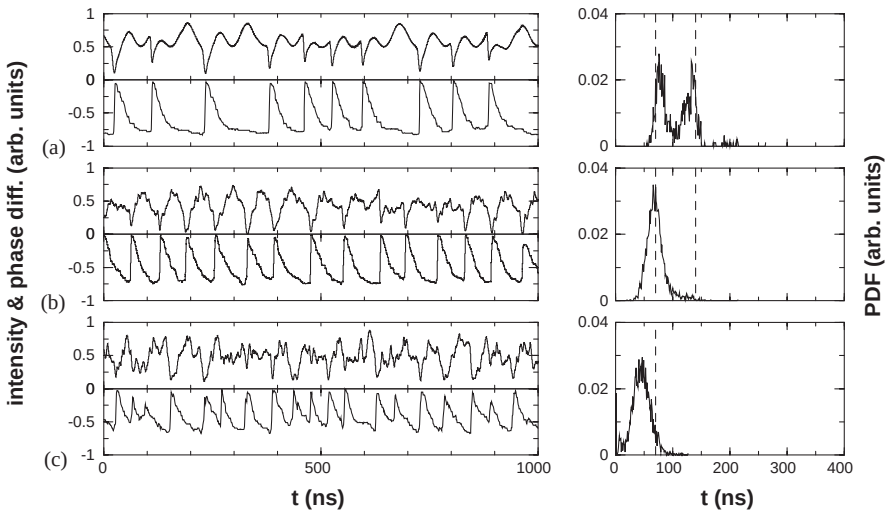

Fig. 40. Time evolution of the laser intensity (left column, upper plots), the phase difference $\eta(t)$ (left column, lower plots) and the corresponding PDFs of the dropout periods (rights column) for increasing values of the external-noise strength: (a) $D = 0.0$ ps, (b) $D = 0.25$ ps, and (c) $D = 0.80$ ps [355].

(PDFs) of the interval between dropouts, for three different values of the noise amplitude $\sigma = \sqrt{D/\tau_c}$ and a fixed correlation time of $\tau_c = 240$ ps. The modulation amplitude is set to 3% of the threshold current and its period to $T = 70$ ns. In the absence of noise (Fig. 40(a)), and with these parameters, the PDF presents two peaks at periods around T and $2T$. When noise intensity is increased to intermediate values, such as $D = 0.25$ ps, the PDF exhibits just one peak centered at around T (Fig. 40(b)). Finally, when noise intensity is increased further the system loses regularity, and dropouts occur much closer to one another, and hence clear dropouts become difficult to discern (Fig. 40(c)).

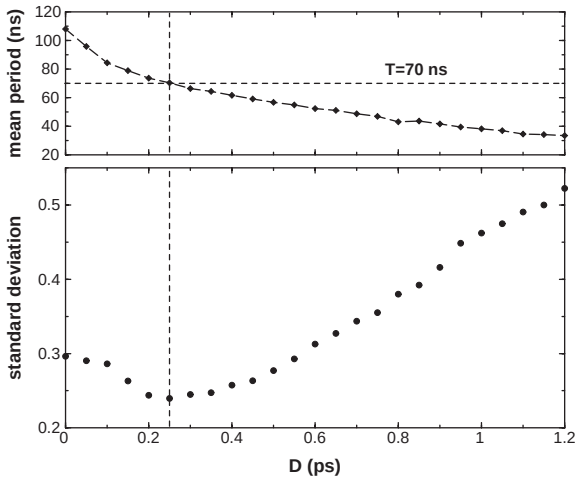

Fig. 41. Mean and relative standard deviation of the dropout intervals versus noise intensity [355].

The enhanced regularity for increasing noise can be characterized by computing the mean value and standard deviation of the dropout intervals. The dependence of these two quantities on the noise intensity is shown in Fig. 41, which shows clearly that the regularity of the time series is maximal for an intermediate value of noise. For this optimal situation the mean dropout interval coincides with the period of the external driving. As in the case where the external modulation is absent, the resonance also exists with respect to the noise correlation time [355].

5. Noise-induced global oscillations in stochastic cellular automata

We now shift our attention towards the dynamics of coupled excitable elements under the influence of spatio-temporal random fluctuations. Starting from the pioneering work of Winfree [356] and Kuramoto [357,358] on coupled phase oscillators, numerous studies have focused on systems where the dynamics of the single units is *deterministic*. It is still one of the current topics in complex systems research [3,359].

In the next two sections, we examine collective behavior and synchronization in the presence of noise [360–374], whereas Section 7 deals with spatio-temporal structures induced by noise in locally coupled excitable media. We review computer simulations and then give analytical treatments using coupled cellular automata and stochastic active rotators as models.

5.1. Global oscillations in excitable cellular automata

5.1.1. Cellular automata for excitable media

A simple way to describe the dynamics of spatially extended excitable media relies on the cellular automata models [3,375]. This kind of description consists of a set of rules which determine the activation state at a given location in space at a certain time, as a function of the state of the system at that point and neighboring ones in the past. As usual, a few discrete values $u_{i,k}$ define the state of

a location i,k in cellular automata, in the simplest case $u_{i,k} = 0, 1$ standing for "rest" and "excited" in the case of excitable media.

Cellular automata are routinely used, for instance, in neuroscience, where they provide a simple but approximative description of cortical tissue [376,377]. Stochastic generalizations are straightforward, with deterministic updates being replaced by stochastic rules. In the context of noise-induced phenomena, a stochastic cellular automaton was proposed by Jung and Mayer–Kress [378] to study the behavior of an array of stochastic threshold devices with excitable properties. It led to the first evidence of spatio-temporal stochastic resonance and noise-induced spiral waves in excitable media [130,378].

Jung and Mayer-Kress' model does not take into account inhibitor dynamics. For that reason, it is unable to exhibit stationary structures such as spots and Turing patterns, like the ones appearing in activator–inhibitor models where the inhibitor diffuses faster than the activator [3]. Stochastic cellular automata that explicitly describe the dynamics of the two species and their diffusion display that type of structures [379], and can also exhibit synchronized global oscillations. This global dynamics can exist even when the system is in the subexcitable regime, provided parametric noise is present [143]. In what follows we will review these results.

Consider a cellular automaton [379,380] described by two dynamic variables, u_{ik} and v_{ik}, which are defined in a two-dimensional square lattice with $N \times N$ sites ($i,k = 1 \ldots N$). The variable u_{ik} can only take the values 0 or 1, and represents the state of the activator at a given cell: 1 stands for the excited state, and 0 for the rest state. The second variable, v_{ik}, represents the concentration of particles that inhibit the state u_{ik}. The activator obeys the following threshold dynamics:

$$u_{ik}(t + \Delta t) = H(\langle u(t)\rangle_{ik} - a_{ik}) \ , \tag{65}$$

where H is the Heavyside step-function, which is equal to 1 when $\langle u(t)\rangle_{ik} > a_{ik}$ and 0 otherwise. The local spatial average $\langle u(t)\rangle_{ik}$ is defined by $\langle u(t)\rangle_{ik} = \sum_{i'k'} u_{i'k'}(t) K(i',k',i,k)$, where the sum runs over all lattice sites, and the function $K(i',k',i,k)$ is a normalized Gaussian kernel that depends only on the Euclidean distance between the sites (i,k) and (i',k'), and whose width gives the characteristic diffusion length L_u of the activator. The corresponding relaxation time τ_u, on the other hand, is given by the update time of rule (65), $\tau_u = \Delta t$.

The parameter a_{ik} represents the local excitation threshold of the system. This threshold is assumed to increase with inhibitor concentration and to be subject to spatio-temporal fluctuations, according to

$$a_{ik} = a_0 + \beta v_{ik}(t) + \sigma \xi_{ik}(t) \ , \tag{66}$$

where a_0 is a constant baseline threshold, β represents coupling with the inhibitor. σ is the standard deviation of the noise, which obeys a Gaussian distribution and is uncorrelated both in space and time.

According to the rule 65, a cell becomes excited if the corresponding local density is overcritical at the previous time instant. Given the definition of the threshold parameter a_{ik} given above, v_{ik} plays the role of an inhibitory field, which is described by a number of inhibitory particles whose dynamics is given by a set of birth-death rules, that update the value of v_{ik} every time step Δt. The birth process is deterministic: in all excited sites the number of inhibitory particles increases by a constant amount $\gamma b^2 \Delta t$, where γ is a generation rate per unit area, and b is the lattice spacing.

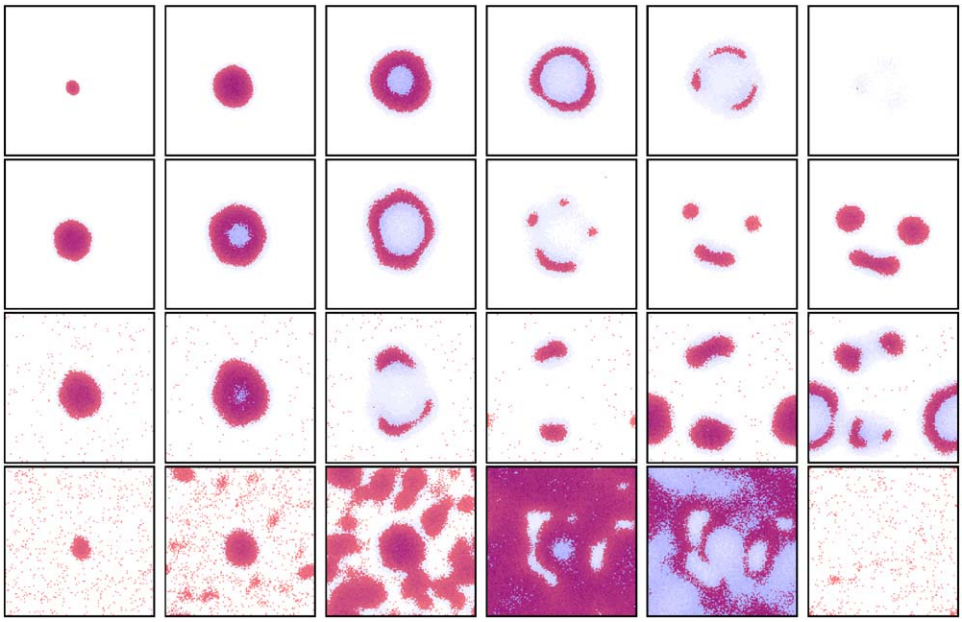

Fig. 42. Spatio-temporal evolution of a cellular automaton with fluctuating excitation threshold in four different regimes (one per row, time flows from left to right). Noise intensity is, from top to bottom, $\sigma = 1.6 \times 10^{-2}$, 4.7×10^{-2}, 5.7×10^{-2}, and 6.3×10^{-2}. A black dot denotes that the corresponding site is excited ($u_{ik} = 1$), and the gray level corresponds to inhibitor concentration (darker for higher concentrations). The time interval between consecutive snapshots differs in general. Other parameters of the model are $N = 128$, $\Delta t = 1$, $a_0 = 0.14$, $\gamma\tau_v = 190$ and $\beta = 4.2 \times 10^{-3}$. The values of the relaxation time and diffusion coefficient ratios ($\epsilon \equiv \tau_u/\tau_v = 0.25$ and $\alpha \equiv D_u/D_v = 0.5$, where $D_s = L_s^2/\tau_s$) correspond to a subexcitable situation. Periodic boundary conditions are considered [143].

The death process, on the other hand, follows a probabilistic rule: at every update, a particle decays with constant probability $\Delta t/\tau_v$, where τ_v is the decay time of v.

Spatial coupling of v is represented by random walks of the inhibitory particles through the lattice, whose characteristic length gives the diffusion length L_v of the inhibitor.

5.1.2. *Noise supported spatio-temporal structures*

Let us examine the influence of noise in the subexcitable regime of this cellular automaton model. This regime is defined as that in which no initial excited structure can survive deterministically. The typical evolution of a localized initial condition is shown in Fig. 42 for increasing values of the noise level σ, with different rows corresponding to different values of the noise intensity and time evolves from left to right.

For very small noise intensities (upper row) all initial perturbations decay and the system reaches a steady rest state where all cells are inactive. However, as soon as the noise intensity is increased slightly (second row from above) the excitation is seen to survive, since new spots are nucleated in the remains of the original ring before it decays. Increasing noise intensity further spontaneous nucleation occurs, as shown in the third row from above of Fig. 42. Finally, for large enough noise levels (larger than $\sigma_3 \approx 6.0 \times 10^{-2}$ in this case; bottom row of Fig. 42), nucleation processes become ubiquitous and tend to occur in a synchronized way in the different locations of the lattice.

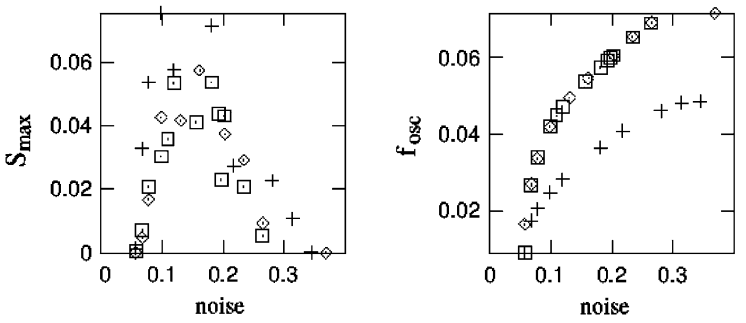

Fig. 43. Amplitude and frequency of the oscillating global (diamonds and crosses) and local (squares) signal as a function of the noise level σ. Diamonds and squares: $\tau_u/\tau_v = 0.25$, crosses: $D_u/D_v = 0.12$ [143].

Such global oscillations arise even though the deterministic regime is subexcitable. Hence, noise induces the medium to become oscillatory. We note at this point that in order to have this effect, fluctuations must act independently in the different sites of the lattice (spatially uncorrelated noise). A *global* noise, affecting in an identical way all lattice cells every time instant, is not able to sustain structures in this system (in fact, spatial correlation is able to change the effect of noise [141,381]).

5.1.3. Power spectrum analysis of the global oscillations

We now concentrate on the synchronized regime depicted in the bottom row of Fig. 42. The dependence of the oscillatory properties of the system versus the noise amplitude σ is shown in Fig. 43, which represents the height and the position of the power spectrum peak of the global signal $U(t) = \sum_{ik} u_{ik}(t)/N^2$.

The spectral peak height, which measures the amplitude of the oscillations, exhibits a maximum for a certain optimal noise, corresponding to synchronization of the firing events among elements of the system. Larger noise destroys synchronization.

On the other hand, the position of the spectral peak measures the fundamental frequency of oscillations (right plot of Fig. 43), and increases monotonously with noise strength, reaching a saturation level that decreases with the inhibitors decay time τ_v (compare diamonds and crosses in the right plot of Fig. 43).

Fig. 43 also shows peak height and position for the power spectrum of the local signal $u_{ik}(t)$ (squares), which coincide with those of the global output discussed above. This means that due to synchronization the local and global fields oscillate with the same well-defined frequency.

It should also be noted that the previous results do not depend on the ability of the inhibitor to diffuse: they hold even in the limit case $L_v = 0$ but with nonvanishing refractory time [382]. This fact indicates that it is the local dynamics of the inhibitor, and the associated *dynamical* refractory time of the system, which gives rise to the global oscillations reported above.

5.2. Analytical treatment of coupled excitable units

5.2.1. Discrete model of excitability

A simple prototype that mimics general features of excitability can be introduced by the three-state non-Markovian model [385,383,384] shown in Fig. 44. Therein a unit is characterized by three

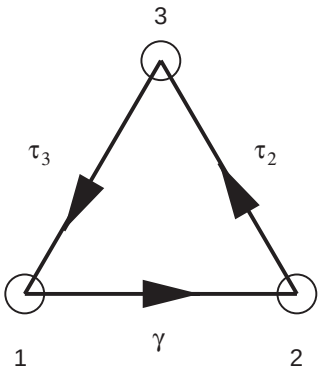

Fig. 44. Three-state model of an excitable unit. The process $1 \to 2$ is Markovian, while the transitions $2 \to 3$ and $3 \to 1$ are deterministic with a fixed waiting time.

different states: state 1 stands for the rest position, from which it escapes by noise to the excited state 2, after which the system performs a longer excursion via state 3 and finally returns to state 1.

The escape $1 \to 2$ is controlled by a rate γ, which can be expressed as an Arrhenius-like relation [53] (cf. Section 2). The waiting probability density for the system to stay in 1 during a time $\tau_{1\to 2}$ is given by

$$w_{1\to 2}(t) = \gamma \exp(-\gamma t) \ , \tag{67}$$

with mean and standard deviation $1/\gamma$.

The transitions $2 \to 3$ and $3 \to 1$ have peaked waiting time distributions at τ_2 and τ_3, which introduces a delay in the model [361,376,386]:

$$w_{2\to 3}(t) = \delta(t - \tau_2), \quad w_{3\to 1}(t) = \delta(t - \tau_3) \ . \tag{68}$$

These expressions model the excursion along the stable branch of the nullcline of the activator. It is supposed that noise does not affect the period of excitation and the return to the rest position.

The proposed model exhibits CR with increasing rate γ. It implies a decay of randomness in the sequence of rotations with the decreasing period $1/\gamma + \tau_2 + \tau_2$, and an increase of the regularity of the spike train. We note that, in contrast to the other models introduced in Section 2, this description does not possess the large noise limit where randomness grows. A proper assumption about the waiting densities (Eq. (68)) could lead to the inclusion of this circumstance.

5.2.2. *Power spectrum of the three-state system*

Generally, to model excitability in a discrete way a two-state description with appropriate waiting time densities would be sufficient. One distinguishes between "firing" and "resting" only, hence the recovery period in this description is included within the resting phase. Then (and this is the advantage of this description), simple results of renewal theory can be used. For example, one can easily find the corresponding power spectra [271]. [5]

[5] Later on when we couple the units, the distinction into three states becomes important again.

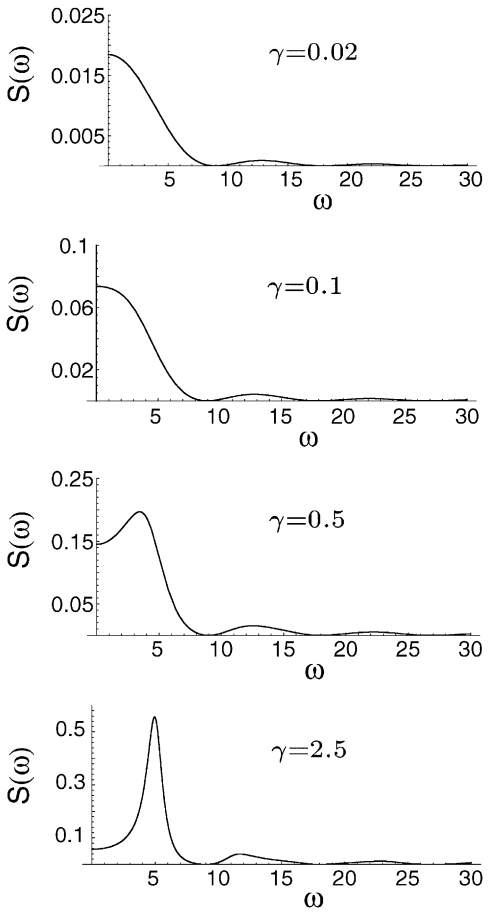

Fig. 45. Power spectra of a single three-state unit with $\tau_2 = 0.3$ and $\tau_3 = 0.7$ and γ as indicated. For small values of $1/\gamma$ the process is oscillating. In contrast to coherence resonance, the peak of the spectrum grows monotonously with increasing γ.

Here we demonstrate that the dynamics of each unit shows typical features of an excitable system [384]. Setting the output $s(t)$ of a unit equal to 1 if the unit is in state 3, and 0 elsewhere, we do not distinguish between 1 and 2. Then, we find the power spectrum of the three-state dynamics [see Eq. (21)]:

$$S = \frac{4}{\omega^2(1/\gamma + T)} \operatorname{Re} \frac{(1 - \mathrm{i}\omega/\gamma - \mathrm{e}^{\mathrm{i}\omega\tau_2})(1 - \mathrm{e}^{\mathrm{i}\omega(T-\tau_2)})}{1 - \mathrm{i}\omega/\gamma - \mathrm{e}^{\mathrm{i}\omega T}} , \tag{69}$$

with $T = \tau_2 + \tau_3$.

The stochasticity can be controlled by varying the amount of time spent in state 1 compared to T. If $1/\gamma$ is large, the system spends a lot of time in state 1 and the stochasticity of the first step dominates the dynamics. As a result, the spectrum decreases monotonically until it becomes zero at $\omega_0 = 2\pi/\tau_3$. Contrarily, for smaller values of $1/\gamma$ the process becomes oscillating (Fig. 45).

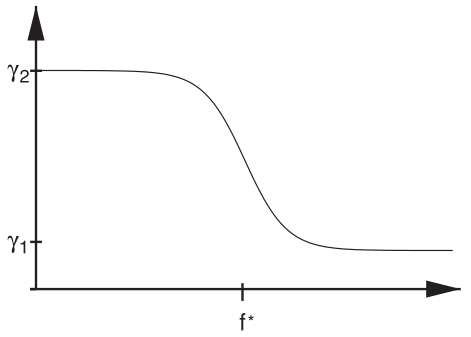

Fig. 46. Sigmoidal dependence of the rate γ for the transition $1 \to 2$ as function of the order parameter. In the following the position of the sigmoid f^* is always kept equal to 0.5, $\gamma_{2/1} = \gamma_0(1 \pm \Delta)$.

5.2.3. Order parameter, coupling and balance equations

Let us consider a system consisting of N stochastic three-state units. As we will show, this simple reduced description allows an analytical treatment for the occurrence of global oscillations in excitable media [383,384]. First, we introduce the dynamic order parameter of the ensemble:

$$f(t) = \frac{1}{N} \sum_{i=1}^{N} s_i(t) \ , \tag{70}$$

with $s_i(t)$ denoting the output of unit i. Furthermore we set $s_i(t) = 1$ if the ith element is in state 3, and $s_i(t) = 0$ otherwise. Therefore, the order parameter $f(t)$ describes the occupancy of the third state.

Coupling between the individual elements is introduced by feeding back the order parameter $f(t)$ into the rate γ in a inhibitory sigmoidal fashion (Fig. 46)

$$\gamma(f(t)) = \gamma_0 \left(1 + \Delta \tanh\left[-\frac{f(t) - f^*}{2\sigma}\right]\right) \ . \tag{71}$$

This expression models the fact that the transition from $1 \to 2$ is slowed down if the third state is populated. Additionally, if the parameter σ is large the coupling depends weakly on the value of $f(t)$. The rate γ is approximately constant and equal to γ_0. Contrarily, in case of small σ a sharp transition between the two rates $\gamma_{2/1}$ occurs if $f(t)$ crosses f^*. Hence, σ^{-1} can be seen as the coupling parameter.

A typical temporal sequence of $f(t)$ is shown in Fig. 47 for a system consisting of $N = 1000$ units. Although each individual unit is governed by the stochastic transition $1 \to 2$, the whole system shows an undamped oscillation with a period about 3 [a.u.]. Obviously, this behavior resembles coherence resonance in coupled excitable units as presented previously [143,118].

In the limit $N \to \infty$ the state of the system can be described by the ensemble-averaged occupation probabilities $P_k(t)$, $k = 1, 2, 3$, i.e. the probability that a unit in the ensemble stays in the state k at time t. Following a mean field assumption, we identify the order parameter $f(t)$ with $P_3(t)$. In particular, we set $f(t) = P_3(t)$ in the expression of the rate in Eq. (71). Then the dynamics of the

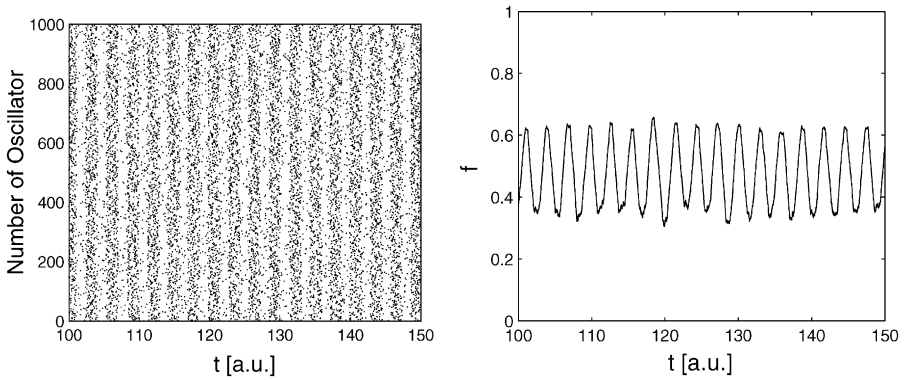

Fig. 47. Temporal sequence of globally coupled $N = 1000$ units (vertical axis) versus time. Each time an unit performs a $2 \to 3$ transition a point is plotted. The right plot shows the global system output f. In all figures the following parameters were used: $T = 2.5$, $\tau_2 = 0.5$, $\gamma_0 = 0.5$, $\Delta = 0.6$, $\sigma = 10^{-5}$ and $f = 0.5$ [383].

ensemble can be described by the set of integro-delay equations:

$$P_1(t) = 1 - P_2(t) - P_3(t) \ ,$$

$$P_2(t) = \int_{t-\tau_2}^{t} \gamma(P_3(t'))P_1(t')\,\mathrm{d}t' \ ,$$

$$P_3(t) = \int_{t-T}^{t-\tau_2} \gamma(P_3(t'))P_1(t')\,\mathrm{d}t' \ . \tag{72}$$

While the first equation expresses the normalization condition, the second and third account for the balance of probability. The probability $P_2(t)$ is equal to the time-integrated decay from state 1 from $t - \tau_2$ up to time t and $P_3(t)$ the integrated decay from $t - T$ up to $t - \tau_2$, respectively.

5.2.4. The transition to global oscillations

Eq. (73) possesses a single stationary solution (fixed point). Setting $P_k(t) = P_k^*$ leads to a self consistent relation for P_3^*:

$$P_3^* = \frac{\tau_3}{T + 1/\gamma(P_3^*)} \ , \tag{73}$$

which is the ratio between the time spent in state 3 to the mean time for one round trip. Analogous relations follow for P_1^* and P_2^*.

In order to analyze the stability of this single steady state given by Eq. (73), we add small perturbations $P_k(t) = P_k^* + \delta P_k(t)$ with $\sum_{k=1}^{3} \delta P_k = 0$. With the typical ansatz $\delta P_k(t) \propto \exp(\lambda t)$, where $(\lambda \neq 0)$, linearization of Eqs. (72) for small δP_k leads to the characteristic equation [383]:

$$1 + \lambda^{-1}\{\gamma(P_3^*)(1 - \mathrm{e}^{-\lambda T}) - s(\mathrm{e}^{-\lambda\tau_2} - \mathrm{e}^{-\lambda T})\} = 0 \ . \tag{74}$$

Here we have introduced $s = \gamma'(P_3^*)P_1^* < 0$ and γ' as the first derivative of γ with respect to P_3.

Solutions of Eq. (74) $\lambda = \lambda' \pm \mathrm{i}\lambda''$ are complex conjugate, and the bifurcation corresponds to parameter values where λ crosses the imaginary axis. Putting, therefore, in Eq. (74) $\lambda' = 0$ with

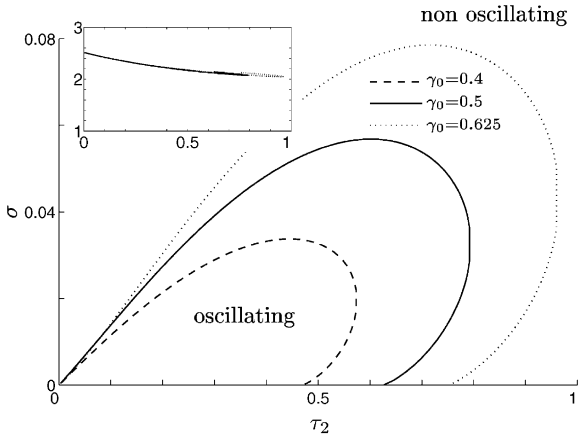

Fig. 48. Bifurcation diagram in the τ_2–σ plane for different values of γ_0, showing the parameter region of coherent oscillations. The inset shows the corresponding frequency along the line of bifurcation. All other parameters as in Fig. 47 [383].

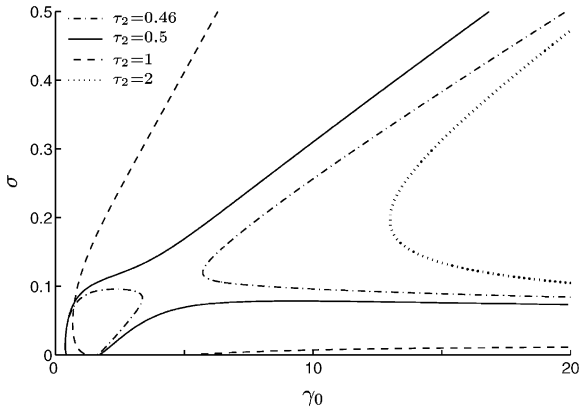

Fig. 49. Bifurcation diagram in the γ_0–σ plane for different values of τ_2 showing the parameter region of coherent oscillations. All other parameters as in Fig. 47 [383].

$\lambda'' \neq 0$ one finds the condition for a Hopf bifurcation of the dynamics of the ensemble. In parameter space, the Hopf bifurcation is defined by the following equations:

$$\gamma(P_3^*)(1-\cos(\lambda'' T)) - s(\cos(\lambda''\tau_2) - \cos(\lambda'' T)) = 0 \ ,$$

$$\lambda'' + \gamma(P_3^*)\sin(\lambda'' T) + s(\sin(\lambda''\tau_2) - \sin(\lambda'' T)) = 0 \ .$$

Both equations can be solved numerically. Figs. 48 and 49 show the region of coherent oscillations in the $\tau_2 - \sigma$ and $\gamma_0 - \sigma$ plane, respectively.

With the increase of τ_2 with fixed γ_0 and $\sigma \neq 0$, the coherent oscillations start from a finite value of τ_2. Even for $\sigma = 0$ the waiting time in the state $'2$ τ_2 must be greater than 0 to obtain oscillations

of the ensemble. For larger values of τ_2 the ensemble desynchronizes again. Interestingly, there exist values of τ_2 where σ has to exceed some finite value in order for the oscillations to be observed, and one gets a re-entrant phase transition back to the non-oscillating phase. With increasing γ_0 the region of synchronous oscillating behavior expands.

The effect of γ_0 on the occurrence of oscillations is more complex, as presented in Fig. 49 for different τ_2. For small τ_2 two separated regions for oscillations in the parameter plane (dash-dotted lines) exist, which merge at $\tau_2 \approx 0.48$ (solid line). The region corresponding to oscillations grows with increasing τ_2 and attains a maximum at $\tau_2 \approx 1$ (dashed line). Further increase of τ_2 reduces the region of oscillations again (dotted line). Only large values of γ_0 above 14 are able to exhibit global oscillations. Another interesting result is that for small values of σ and small values of τ_2 an increase of randomness by decreasing γ_0 causes coherent oscillations to appear.

In summary, the bifurcation behavior describes the existence of collective oscillations of the globally connected excitable units. Also the frequency of oscillations obtained in the simulations agrees quantitatively with the bifurcation analysis, as shown in the inset of Fig. 48. We underline that the specific choice of the coupling function is not crucial to obtain the collective oscillations. It was selected to model the generic feature of coupling, which consists in a change (decay) of the local transition behavior of the individual units in dependence on the present state of the network and coupling constant. Interestingly, Hopf bifurcations can be found in the case that the spectra of the single units, taken independently [see Eq. (45)], exhibit a strong peak, but also for parameter values for which they decay monotonously at small frequencies.

5.2.5. *Sparse networks of coupled excitable elements*

For completeness, we now turn our attention to sparse networks and the influence of the connectivity on the onset of coherent oscillations [383]. For this purpose, we study the transition from an ordered topology to a random network via a small-world network, as introduced recently by Watts and Strogatz [387–392]. We start from a ring with $N \approx 1000$ vertices, each vertex being one the three-state units described above. Each vertex is connected to its k nearest neighbors with undirected edges. With probability p each edge is then cut and reconnected to a randomly chosen different vertex in the network.

In this way, the parameter p interpolates between a completely regular ($p = 0$) and a completely random ($p = 1$) network. Note that the number of links is much smaller than the number of all possible connections between vertices, which is $N(N-1)/2$. The small-world networks are found for small values of p, where the mean shortest path between two arbitrary nodes drops rapidly, while the cluster index, giving the number of common neighbors and characterizing the order of the network, is still large [387].

As a measure for the size of the collective oscillations, we choose the height of the central peak in the power spectrum of the global order parameter $f(t)$. In the case of a completely regular network with $p = 0$ we have found small coherent islands, which interchange over time but never collapse to a global cluster. Since these islands are generally not in phase, the system does not display *global* oscillations and no peak in the spectrum arises. For increasing randomness, i.e. $p > 0$ with the number of connections fixed, the oscillations become more pronounced and are finally maximized for complete disorder, as can be seen in Fig. 50. The transition to macroscopic oscillations shows a threshold-like behavior at $p \approx 0.2$.

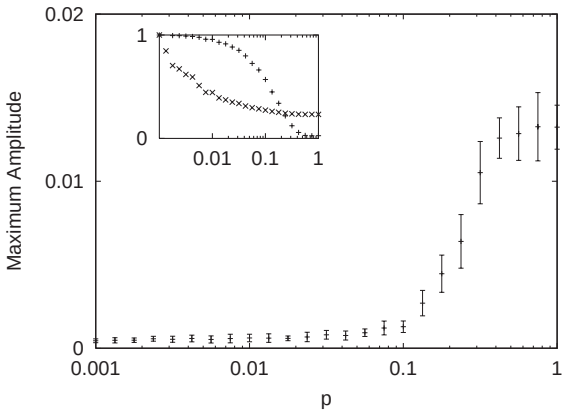

Fig. 50. Location of the maximum amplitude of the spectrum of the system output f. The inset shows the cluster index (+) and the mean shortest path length (×) in the network [383].

The inset shows for comparison both the cluster index and the mean path length. As it can be seen, there is a steep decrease in the mean path length already for small $p \approx 0.01$. However, the amplitude of the oscillations starts to increase, only as the cluster index begins to decrease. We conclude, therefore, that completely random networks synchronize best in our model. A small network with short mean connections is insufficient for synchronization in our model.

6. Ensemble of globally coupled FitzHugh–Nagumo elements

6.1. Simulations of globally coupled FitzHugh–Nagumo elements

Another illustration of transitions between different dynamical regimes of a mean field is provided by a set of globally coupled FN elements:

$$\epsilon \dot{x}_i = x_i - \frac{x_i}{3} - y_i + W(\bar{x} - x_i) \ ,$$

$$\dot{y}_i = x_i + b + \sqrt{2D}\xi_i(t) \ , \tag{75}$$

where $\bar{x} = 1/N \sum_{k=1}^{N} x_k(t)$, N is the number of elements in the array, W is the coupling strength, b and D are again the excitability parameter and the noise intensity, respectively.

Eqs. (75) were simulated numerically for $N = 1000$ elements. The coupling strength W was fixed at $W = 0.1$. The parameter $b = 1.05$ was chosen in the excitable region, so that in the absence of noise each individual element possesses a stable fixed point.

The collective dynamics of the system can be visualized using the mean fields $\langle x(t) \rangle$ and $\langle y(t) \rangle$. The phase portraits of the system on the plane $\langle x(t) \rangle$ versus $\langle y(t) \rangle$ are shown in Fig. 51. For weak noise the system possesses a stable equilibrium. With increasing noise intensity a limit cycle is born. The waveform of $\langle x(t) \rangle$ resembles periodic spiking of a single FN. As we will see below, this situation corresponds to the running phase solution.

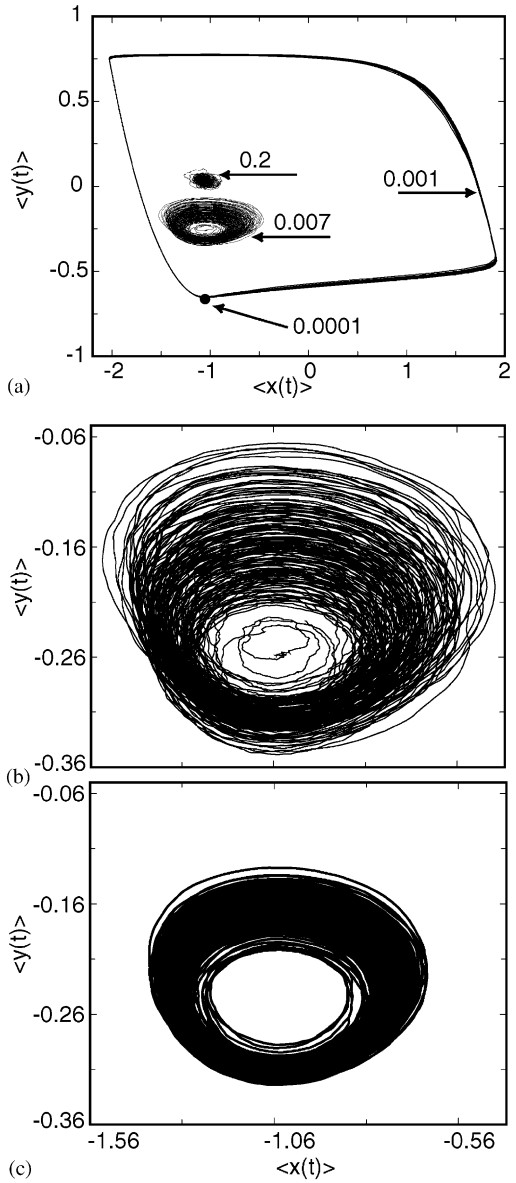

Fig. 51. (a) Phase portraits of the mean field $\langle x(t)\rangle$, $\langle y(t)\rangle$ for $N=10^3$, $b=1.05$, $W=0.1$, $\epsilon=0.01$, and indicated values of noise intensity D. Magnified phase portrait for $D=0.007$ for $N=10^3$, (b) and $N=10^4$, (c) elements. Transients are omitted [393].

With further increase of D, the amplitude of oscillations shrinks dramatically at $D \approx 0.0068$. In this case the waveform $\langle x(t)\rangle$ does not exhibit spikes, but rather resembles chaotic motion [Fig. 51(b)]. This case corresponds to a local oscillation in the phase model.

We have checked how the observed complex motion is robust against changing the number of elements in the ensemble (for a discussion of finite size effects on mean field dynamics, see

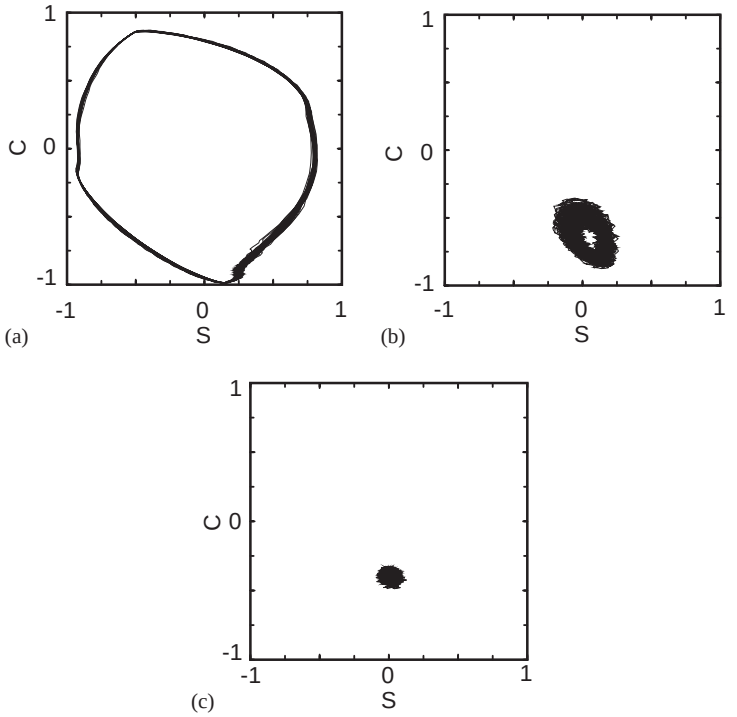

Fig. 52. Phase portraits for the order parameter in Eq. (76). (a) $D = 0.001$, (b) $D = 0.007$, (c) $D = 0.2$. Other parameters are the same as in the previous figure [393].

Refs. [394,395]). In Fig. 51(c) we show simulation results for $N = 10\,000$ elements, for the same parameters values as in Fig. 51(b). These results demonstrate a smeared limit-cycle attractor. The correlation structure of the corresponding processes is qualitatively the same as for the smaller ensemble (see the results of power spectra analysis below). Finally, for large noise intensity the mean field dynamics again collapses to the fixed point, which is apparently different from the equilibrium observed at low values of D. Note that individual elements in both last cases demonstrate spiking behavior.

An alternative description is based on the introduction of the instantaneous phases for individual units. The phase of ith element can be estimated as $\varphi_i(t) = \arctan(\dot{x}_i(t)/x_i(t))$, although other definitions are indeed possible (for example based on spike occurrence times or on the analytic signal concept) [433]. Afterwards one may proceed with a complex order parameter

$$\frac{1}{N}\sum_{j=1}^{N} \mathrm{e}^{\mathrm{i}\varphi_j} = c + \mathrm{i}s \ , \tag{76}$$

where $c \equiv N^{-1}\sum_{j=1}^{N}\cos\varphi_j$ and $s \equiv N^{-1}\sum_{j=1}^{N}\sin\varphi_j$. Phase portraits c versus s are shown in Fig. 52 for the same parameter values as in the previous figure, and confirm the above conjecture that the increase of noise is accompanied by a transition from the steady state (through two different kinds of oscillations) to the other time-independent distribution.

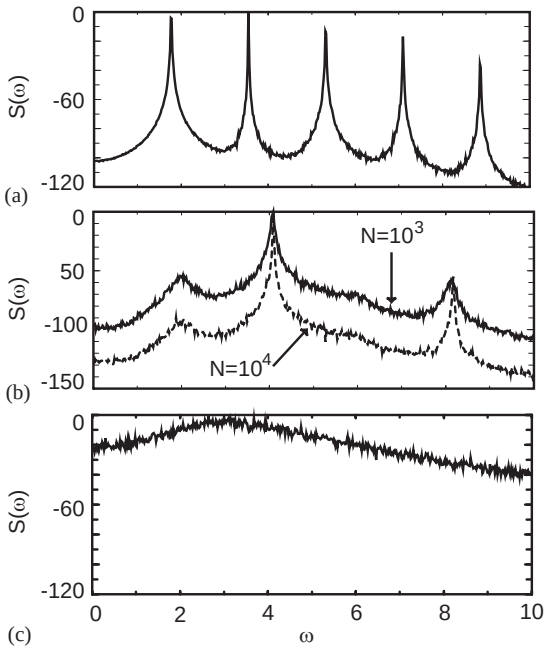

Fig. 53. Power spectra of the cosinus of ensemble phase for the ensemble of globally coupled FN elements given in Eqs. (75). (a) $D = 0.001$, $N = 10^3$, (b) $D = 0.007$ for $N = 10^3$ (solid line) and $N = 10^4$ (dashed line), (c) $D = 0.2$. Other parameters are the same as in the previous figure [393].

Finally, we investigate the power spectrum of the cosinus of the ensemble phase as a function of the noise intensity. For a small noise intensity the spectrum is uniform, resembling white noise. This is the case where the mean field relaxes to a stable fixed point. If the limit cycle is created with increasing noise, the spectrum displays well-defined peaks at the main frequency and its harmonics [Fig. 53(a)]. The complex motion at moderate noise is characterized by broadened peaks [Fig. 53(b)]. The oscillatory character of this regime is still expressed by the existence of a sharp peak at $\omega = 4$. However, broad peaks at the subharmonics resemble a power spectrum of a chaotic motion. Note that the qualitative structure of the power spectrum is conserved if the number of elements in the ensemble changes [solid and dashed lines in Fig. 53(b)]. For a large noise intensity, if the oscillations disappear the power spectrum possesses again a uniform structure [Fig. 53(c)].

6.2. Analysis of globally coupled FitzHugh–Nagumo systems

We now present a cumulant approach that, together with a Gaussian approximation, allows us to analyze the behavior of an ensemble of coupled FN elements driven by additive noise (for other approaches see [396–400]). The use of a full set of cumulants or moments instead of a hierarchy of probability densities is an alternative way to describe a stochastic process [302]. Techniques based on cumulants are in many cases more convenient, because they allow to use several approximations. For instance, for a Gaussian stochastic process only first and second order cumulants are non-zero, while all moments may have finite values.

For diffusion stochastic processes, which are described by Fokker–Planck equations, the cumulant approach aims to study the dynamics of cumulants, and allows to analyze a set of ODEs instead of the parabolic partial differential equation (the Fokker–Planck equation). The noise intensity appears to be an additional parameter in cumulant equations. A problem arises, though, when the original stochastic differential equations are nonlinear. In such case the set of ODEs for cumulants appears to be unclosed: an equation for the nth order cumulant may contain higher order cumulants. Several approximations can be used to truncate the series of cumulant equations [401], the simplest one being the Gaussian approximation, which takes into account the evolution of only the first- and second-order cumulants. The resulting system of cumulant equations in the Gaussian approximation allows us then to perform a bifurcation analysis with an additional control parameter, namely the noise intensity. The cumulant approach within the Gaussian approximation was successfully used to study the influence of noise on bifurcations in maps [402,403], colored noise-induced transitions in bistable systems [404], phase transitions and SR in globally coupled bistable elements [405,320], dynamics of noisy FN neurons [400] and transitions in globally coupled noisy phase rotators [116,406].

We will now perform the cumulant analysis of a system of globally coupled FN oscillators in the thermodynamic limit of an infinitely large ensemble, $N \to \infty$. In that case the stochastic differential equations of the model read,

$$\begin{aligned} \epsilon \dot{x}_i &= x_i - \frac{x_i^3}{3} - y_i + W(\langle x\rangle - x_i) \ , \\ \dot{y}_i &= x_i + b + \sqrt{2D}\xi_i(t) \ , \end{aligned} \tag{77}$$

where $\langle x(t)\rangle = \lim_{N\to\infty} 1/N \sum_{i=1}^{N} x_i(t)$. Next, we introduce deviations from the mean field, $\langle x(t)\rangle$, $\langle y(t)\rangle$, for each element: $n_x(t) = \langle x(t)\rangle - x_i(t)$, $n_y(t) = \langle y(t)\rangle - y_i(t)$. We assume that these fluctuations are Gaussian and statistically independent in different elements. We introduce the following notation for the first- and second-order cumulants: the means: $m_x(t) = \langle x(t)\rangle$, $m_y(t) = \langle y(t)\rangle$; the mean square deviations: $s_x(t) = \langle n_x^2(t)\rangle$ $s_y(t) = \langle n_y^2(t)\rangle$; and the cross cumulant: $u(t) = \langle n_x, n_y\rangle$. In the Gaussian approximation (all higher-order cumulants are zero) we obtain the following set of cumulant equations:

$$\begin{aligned} \epsilon \dot{m}_x &= m_x - \frac{m_x^3}{3} - s_x m_x - m_y \ , \\ \dot{m}_y &= m_x + b \ , \\ \frac{\epsilon}{2}\dot{s}_x &= s_x(1 - m_x^2 - s_x - W) - u \ , \\ \frac{1}{2}\dot{s}_y &= u + D \ , \\ \frac{1}{2}\dot{u} &= \frac{1}{\epsilon}u(1 - m_x^2 - s_x - W) - \frac{1}{\epsilon}s_y + s_x \ . \end{aligned} \tag{78}$$

Thus, the SDEs (77) are now approximated by a set of 5 nonlinear ODEs. In order to obtain an analytical result for the noise-induced transition to oscillatory motion, we can simplify the cumulant equations (78) further, by noting the difference in the relaxation time scales between the first- and second-order cumulants: the latter change faster than the former. We thus can consider the dynamics

of only the first-order cumulants by substituting the stationary values for the second-order cumulants into the first two equations in the set (78), to obtain

$$\epsilon \dot{m}_x = m_x - \frac{m_x^3}{3} - \frac{m_x}{2}\left[1 - W - m_x^2 + \sqrt{(W - 1 + m_x^2)^2 + 4D}\right] - m_y \ ,$$
$$\dot{m}_y = m_x + b \ . \tag{79}$$

This is a rather rough approximation that provides, however, a qualitatively correct description of the transition to oscillatory regime for the original globally coupled array of FN elements each in excitable regime ($a > 1$), and for small noise intensities. The bifurcations of stationary solutions of the cumulant equations (79) can then be studied analytically. The single equilibrium point

$$m_x^0 = -b \ ,$$
$$m_y^0 = -\frac{b}{6}\left[3 + b^2 + 3W - 3\sqrt{4D + (W + b^2 - 1)^2}\right] \ ,$$

experiences a Hopf bifurcation with increasing noise intensity D. The Hopf bifurcation is given by a surface in three-dimensional parameter space (b, W, D),

$$D = \frac{1}{8}[-1 - 5b^4 + b^2(10 - 6W) - (W - 6)W]$$
$$- \frac{1}{8}\sqrt{(w^2 + b^2 + 1)((1 + W)^2 - 7b^4 - 2b^2(3W - 5))} \ . \tag{80}$$

For the parameters values used in numerical simulations $b = 1.05$, $W = 0.1$ (see Fig. 51), Eq. (80) gives a bifurcation value of the noise intensity equal to $D = 0.0025$, which is close to what was observed in the numerical simulations.

6.3. Coupled active phase oscillators

6.3.1. Phase description of coupled phase oscillators

Another approach to explain collective oscillations is based on the model of coupled phase oscillators (active rotators) [359]. We intend here to study the simplest variant where the phase dynamics of each rotator evolves akin to an overdamped Brownian particle in a biased periodic potential. For simplicity we assume a cosine potential and Gaussian white noise as in Section 2.5. This model can be improved by taking into account higher-order Fourier components of the potential, and with generically multiplicative components in the noise source.

Compared with Section 2.5, coupling adds another term [2,114,115,358,407] in the model

$$\frac{\mathrm{d}}{\mathrm{d}t}\varphi_i = \Omega - a\sin\varphi_i + \sum_j W_{i,j}(\varphi_j - \varphi_i) + \sqrt{2D}\xi_i(t) \ , \tag{81}$$

This model was first introduced by Kuramoto and coworkers to study coupled oscillators [114,115]. Since then it has attracted a lot of interest, and a huge literature has been devoted to many different aspects of the dynamics of coupled phase oscillators, such as pattern formation, forced and mutual synchronization with local and global coupling [356,408–413]. A quite rich variety of locally and globally locked, running, pinned and dead solutions have been reported in Refs. [414–418].

Also, random switches between two time dependent frequencies $\Omega(t)$ [419,420] have been considered, and have shown bistability and oscillatory behavior. Many experimental observations in different research fields, most of them dealing with synchronization phenomena, relate to this model (e.g. Refs. [34,421–424], to mention only a few of them).

Here we again will concentrate on noise effects on collective dynamics of globally connected oscillators [see Eq. (81)]. A multifaceted behavior has been found in case of multiplicative noise, including noise-induced first- and second-order phase transitions, time-periodic phases, and clustering [425–427]. Spontaneous symmetry breaking entailing a ratchet-like transport mechanism with negative resistance and a hysteretic behavior has been reported [428–431], whereas globally connected ratchets have been studied in Ref. [432].

We aim to answer the question of whether independent additive white noise added to every unit in the ensemble is sufficient for bifurcations to occur in the global response of the system. This question was first addressed by Kuramoto using a Fourier-decomposition approach [115]. Later Kurrer and Schulten [116] derived dynamical equations for the first two cumulants (the mean and the variance) of the ensemble averaged phase

$$\phi(t) = \frac{1}{N}\sum_{i}^{N} \varphi_{(t)} \ . \tag{82}$$

Kurrer and Schulten have confirmed the existence of noise-induced oscillations of coupled excitable units. However, their approach was limited to small values of the variance. Here we derive modified cumulant equations, within the Gaussian approximation, which are valid even for strong noise [393]. This approach will allow us to perform a detailed bifurcation analysis of the system. In addition, we find a new regime of localized or breathing oscillations.

The bifurcation scenario that we derive in this section [393] agrees qualitatively with results obtained using the Fourier decomposition approach with 14 Fourier modes [115]. In contrast, we describe qualitatively the same situation with only equations for the first and second cumulants, which happen to be sufficient as long as the probability density of the phase distribution can be approximated by a single peaked function.

6.3.2. The model and cumulant equations

We start with a set of N globally coupled identical nonlinear elements which are subjected to white noise. The state of each element is characterized by its instantaneous phase φ_i, with $i = 1,\ldots,N$. All elements have the same frequency, and without loss of generality we choose $\Omega = 1$. Finally, the elements are assumed to be globally connected. Hence the dynamics of an element reads:

$$\frac{\mathrm{d}}{\mathrm{d}t}\varphi_i = 1 - a\sin\varphi_i + \frac{W}{N}\sum_{j=1}^{N}\sin(\varphi_j - \varphi_i) + \xi_i(t) \ . \tag{83}$$

The parameter a characterizes the inhomogeneity of the phase rotation. When, for a decoupled single oscillator, a is increased across the value 1, the oscillatory regime is replaced by a steady state due to a saddle-node bifurcation. The intensity of coupling between the oscillators is measured by the parameter W, which independent of a. Finally, stochastic terms $\xi_i(t)$ (corresponding to independent noise) are added, and assumed to be Gaussian and white with $\langle \xi_i(t_1)\xi_j(t_2)\rangle = 2D\delta(t_1 - t_2)\delta_{ij}$.

The dynamics of the collective variables c and s, as defined in Eq. (76), is described by the following equations:

$$\dot{s} = c - Ds - (a + Wc)\langle \sin\varphi_i \cos\varphi_i \rangle + Ws\langle \cos^2\varphi_i \rangle \ ,$$
$$\dot{c} = -Dc - s + (a + Wc)\langle \sin^2\varphi_i \rangle - Ws\langle \sin\varphi_i \cos\varphi_i \rangle \ , \tag{84}$$

where the averages $\langle \cdots \rangle$ are taken over the whole ensemble of N elements. If the distribution of ϕ [see Eq. (82)] is Gaussian, the averages can be computed explicitly. Let m and σ be the mean and the variance of the distribution, respectively. Then the average of the sine and cosine terms are:

$$\langle \sin b\phi \rangle = \mathrm{e}^{-b^2\sigma^2/2} \sin m, \quad \langle \cos b\phi \rangle = \mathrm{e}^{-b^2\sigma^2/2} \cos m \ . \tag{85}$$

This allows to obtain a set of dynamical equations in closed form:

$$\dot{m} = 1 - a\mathrm{e}^{-\sigma^2/2} \cosh\sigma^2 \sin m \ ,$$
$$\dot{\sigma^2} = 2D - 2(a\mathrm{e}^{-\sigma^2/2} \cos m + w\mathrm{e}^{-\sigma^2}) \sinh\sigma^2 \ . \tag{86}$$

The noise intensity D has entered these equations as an additional parameter, and becomes a control parameter for the bifurcations that will be presented below.

The phase space of Eq. (86) is a cylinder. The center of the Gaussian $m(t)$ is restricted to the circle, whereas the unwrapped variance $\sigma^2(t)$ evolves over positive values. It can be easily seen that the variance for generic solutions remains bounded, which is an important qualitative improvement compared to the previous Gaussian approximation in [116]. There the equations for the first cumulants retained only the lowest-order terms in σ^2. As a result, $\sigma^2(t)$ displayed an unbounded growth in the non-stationary regimes of the dynamical system [116]. On the other hand, taking into account higher-order terms in Eq. (86) ensures saturation at finite σ^2, except for a singular parameter value.

6.3.3. Dynamical regimes and their bifurcations

Analysis of Eqs. (86) in the physically relevant domain of parameters shows that the dynamics possesses either 1 or 3 steady solutions. The corresponding bifurcation diagrams are presented in Fig. 54 for two different values of coupling strength W. High values of a and D correspond to domains in which one steady state is globally attracting. For low and moderate values of D, a decrease of a leads through a sequence of bifurcations that finally, for small a and small noise, results in the existence of an attracting limit cycle around an unstable fixed point (region indicated as rotations and localized oscillations).

There are two saddle-node bifurcations. The line s_1 in Fig. 54 creates two additional steady states: a saddle point and a node. The other line s_2 in Fig. 54 destroys the saddle and the originally existing fixed point. On both curves s_1 and s_2 one of the eigenvalues vanishes. Additionally, a codimension-2 point exists where two eigenvalues disappear. On the right branch s_1 of the saddle-node bifurcation this point is a Takens–Bogdanov bifurcation point denoted by TB. It is the origin of two further bifurcation lines: (i) the Hopf bifurcation H which extends into the domain of lower a tending to $D = W/2$ as $a \to 0$; and (ii) a homoclinic bifurcation denoted by h and ending at L on the left branch s_2 (for details see Fig. 55).

Above H, for larger noise, the steady state created on the line s_1 is stable, and below it becomes unstable surrounded by a stable limit cycle. Above H at s_2 one stable fixed point and the saddle disappear and a single stable fixed point remains. The curve h marks the existence of a homoclinic

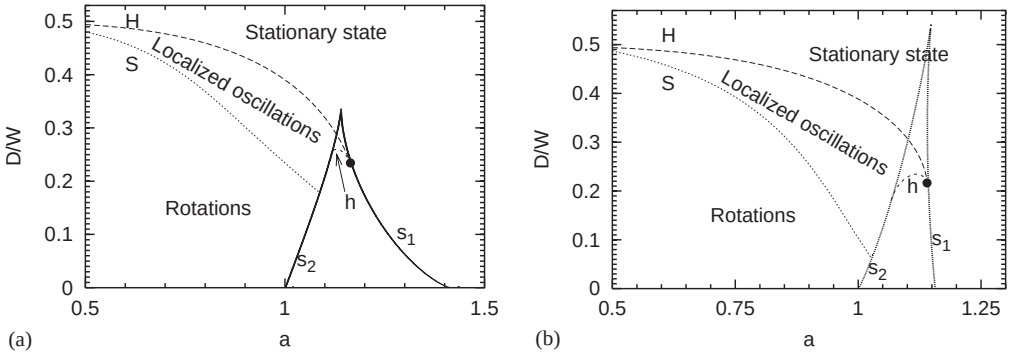

Fig. 54. Bifurcation diagrams of Eq. (86) at $W = 1$ (a) and $W = 0.25$ (b). $s_{1,2}$: saddle-node bifurcations; H: Hopf bifurcation; h: homoclinic bifurcation; S: change of type of oscillatory state; filled circle: Takens–Bogdanov point [393].

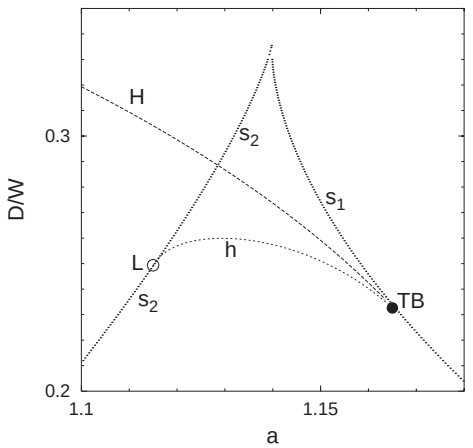

Fig. 55. Enlarged segment of the bifurcation diagram of Eq. (86) at $W = 1$. $s_{1,2}$: saddle-node bifurcations; H: Hopf bifurcation; h: homoclinic bifurcation; circles: bifurcation points of codimension 2 [393].

orbit of the saddle point. Together with the saddle, this curve exists between the two lines $s_{1,2}$. The region above h corresponds to a hysteretic dynamics: a stable steady state coexists with an attracting limit cycle around an unstable fixed point, and their attraction basins are separated by the stable manifolds of the saddle.

Below h the homoclinic orbit has destroyed the limit cycle, and saddle, stable, and unstable fixed points exist. The saddle and the unstable steady state were generated at s_1. At s_2 the stable point together with the saddle collapses, generating first a homoclinic orbit around the third unstable point (Andronov bifurcation). Left from s_2 the saddle and stable fixed point disappear, leaving an attracting limit cycle and the unstable fixed point.

Near the homoclinic bifurcations the period of oscillations diverges. Approaching from the left the lower segment of the curve s_2 this divergence follows the law of inverse square root. Just above the curve h the divergence is logarithmic.

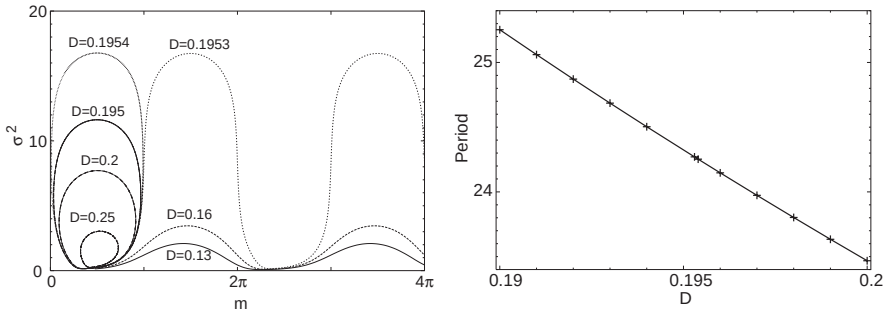

Fig. 56. Left: transition from localized oscillations to rotations. Phase portraits of Eq. (86) for $a = 1.06$, $W = 1$ and various values of D. The bifurcation value is $D_S = 0.19535209\ldots$. Right: period at the transition from localized oscillations to rotations in dependence on the noise intensity [393].

Just below the curve H of the Hopf bifurcation, the newborn periodic orbit has a small amplitude. This amplitude gradually grows for decreasing D at fixed a. On reaching another curve, denoted by S in Fig. 54, the topology of the periodic orbit changes: out of a closed trajectory (which can be continuously contracted into a point), it becomes a closed curve wrapped around the cylinder.

This means that oscillations with bounded amplitudes are replaced by full-circle rotations. In the phase space, this process is mediated by repelling the trajectory to infinity ($m = \pi, \sigma^2 = \infty$) which can be viewed as a kind of global bifurcation, as a homoclinic orbit to a fixed point at infinity. The increase and subsequent decrease of σ^2 happens rapidly, in a rather narrow parameter interval as depicted in the left of Fig. 56.

Remarkably, although the extended periodic orbit is mediated by a homoclinic trajectory, its temporal period does not diverge. The dependence of the period on D can be seen in the right panel of Fig. 56. Apparently, there is no divergence near the bifurcation value $D = 0.1953509$. This unusual behavior is due to the singular character of the bifurcation. Since the saddle point lies at infinity, both the approach along its stable and the subsequent departure along its unstable manifold happen at infinite speed. Accordingly, the slowdown typical for conventional homoclinic bifurcations is absent.

To check the above conjectures, we performed direct numerical integration of Eq. (83) with a set of $N = 10^4$ oscillators. Qualitatively, the results correspond to the predictions of the above analysis: for low intensities of noise the relatively sharply peaked distribution rotates around the circle; for intermediate intensities oscillations with small amplitude are observed; and for high values of D the system settles onto the steady broad distribution. Quantitatively, the threshold values for the transitions between those states turned out to be lower than the values predicted by the bifurcation analysis of Eqs. (86).

Phase portraits for the components of the complex order parameter c and s in the oscillating regime $a = 0.9$ are presented in Fig. 57. Noisy limit cycles characterize both the rotating and the locally oscillating distributions; in the first case, the diameter of the cycle is noticeably larger. In the case of the stable time-independent distribution, the system spirals to the attracting fixed points.

Variation of the coupling strength W appears to produce merely quantitative changes in the bifurcation diagram. With decreasing W the bifurcation values of D get smaller [Fig. 54(b)]; the region

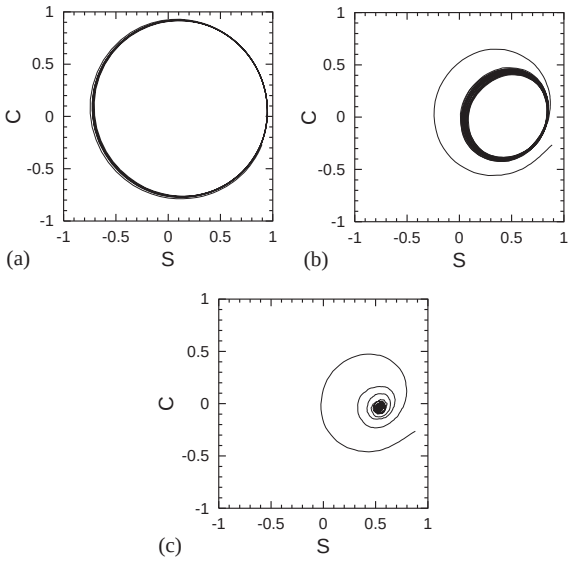

Fig. 57. Phase portraits (with transients) for the order parameter in numerically simulated Eqs. (83) at $a = 0.9$; $W = 1$. (a) Running phase at $D = 0.1$, (b) local oscillations at $D = 0.22$, (c) steady distribution at $D = 0.3$ [393].

between the two curves of the saddle-node bifurcations becomes sharper: in the deterministic limit $D \to 0$ the line s_2, irrespectively of W, begins at $(a = 1, D = 0)$, whereas the starting point of s_1 for $W \to 0$ tends to $(a = 3^{3/4}/2 = 1.13975\ldots, D = 0)$.

Now we draw the general picture of coupled excitable elements with increasing noise D. Let a slightly exceed 1. The sequence starts with a time-independent distribution being stable within a certain interval of noise intensities. On crossing the curve s_2 this state disappears, and an oscillatory rotating regime with large amplitudes is created. Further growth of noise destroys the sharpness of the oscillations resulting after crossing S in an oscillating state with small amplitude. Finally, near the Hopf bifurcation point the amplitude of oscillations collapses and beyond the curve H the other steady state acquires stability.

6.4. Noise-induced synchronization

As seen in the previous section, when noisy excitable systems are coupled, synchronization phenomena are amenable to occur. From the most general point of view, synchronization is understood as an adjustment of some relations between characteristic times, frequencies or phases of two or more dynamical systems during their interaction.

Synchronization has attracted much attention in all fields of natural sciences (see [433] for a recent and comprehensive review). For instance, applications of synchronization in engineering sciences [434,435] have achieved great practical importance and are widely employed. In the case of biophysics, several kinds of synchronization have been reported, including the cases of cultured cells [436], neurons [437,438], and biological populations [439]. Synchronization became a conceptual framework in neuroscience as a general mechanism of large-scale neural integration [440–442].

There is now an extensive literature on stochastic nonlinear dynamics of coupled noisy excitable systems. Examples are studies of synchronization of two coupled excitable neurons modeled by Morris–Lecar systems [186], the emergence of collective coherent oscillations induced by noise [116,123,145,443–446], and studies on array-enhanced coherence resonance [144,447]. In this section we will address the effect of noise-induced global coherence in terms of phase synchronization [118].

6.4.1. Noise-induced oscillations in coupled system with different thresholds

We demonstrate the effect of noise-induced global oscillations using a network of locally coupled non-identical FN oscillators. The discrete network of diffusively coupled oscillators mimics a noisy excitable media which is of high interest in biology, chemistry and physics, and which is described by the following set of stochastic differential equations:

$$\epsilon\dot{u}(t,n) = u - \frac{u^3}{3} - w + W\sum_{n'}[u(t,n') - u(t,n)] \ ,$$

$$\dot{w}(t,n) = u + a(n) + \sqrt{2D}\xi(t,n) \ , \tag{87}$$

where $u(t,n)$ and $w(t,n)$ are fast and slow variables, respectively. For the one-dimensional case these variables are defined on a chain $n = 1,\ldots,N$, while in the two-dimensional case they are defined on a square lattice. The sum over the neighbors stands for the discrete Laplace operator in one and two dimensions, modeling local interactions with coupling strength W. The stochastic forcing by Gaussian white noise ξ is statistically independent in space and with zero mean $\langle\xi(t,n)\xi(t+\tau,m)\rangle = \delta_{m,n}\delta(\tau)$, where $\delta_{m,n}$ is the Kronecker symbol. The excitability parameter $a(n)$ depends on the spatial variable n and is assumed to be a uniformly distributed random variable in the range $[1.03, 1.1]$. Thus, without coupling and noise $(W = 0; D = 0)$ each FN element of the network resides in an excitable regime [48].

The results of simulating a two-dimensional network are presented in Fig. 58. Depending on the noise strength D, for a sufficiently large value of the coupling strength three basic types of space–time behaviors can be observed. For small noise, centers of excitation are nucleated very rarely, and appear at random positions in the media, giving rise to propagating target waves. It should be noted that when two circular waves collide the resulting front shrinks, and hence no new stable spiral waves are created.

However, in the case of parametric noise the propagating fronts may locally backfire small directed spots which breaks propagating excitations and make spirals possible [446]. In this case, different cells in the media are correlated only on a short time scale in comparison with the characteristic time of wave propagation, and there is no synchronization between distant cells. For a large noise strength, the nucleation rate is very high and the media is represented by stochastically firing cells. However, for an optimal noise intensity the media becomes phase coherent: firings of different and distant cells occur almost in phase and the whole media oscillates nearly periodically (see the middle row in Fig. 58).

6.4.2. Description in terms of stochastic phase synchronization

From the mathematical point of view, the theory of synchronization of periodic self-sustained oscillators is well established [434,448,449]. If $\Phi(t)$ is the phase of a periodic oscillator and $\Psi(t)$ is

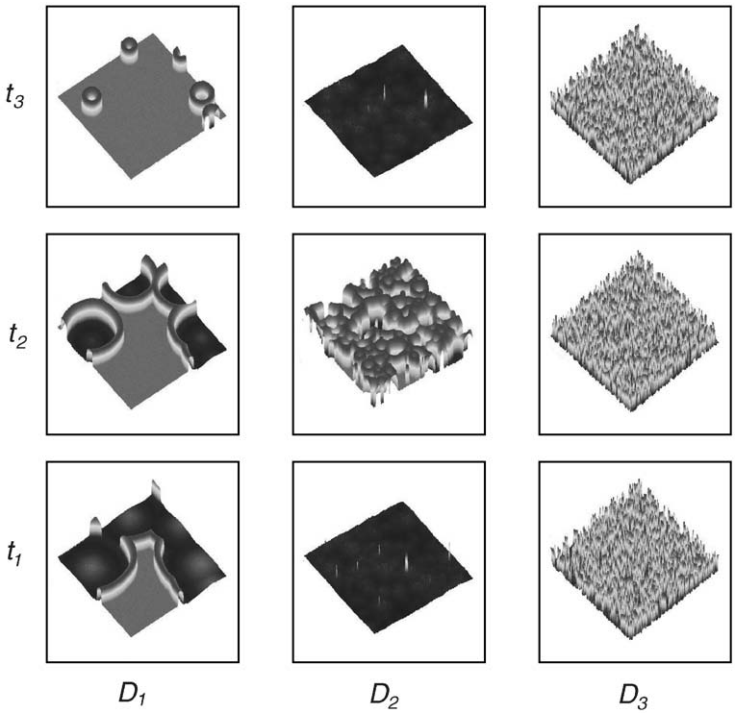

Fig. 58. Spatio-temporal evolution of the system described by Eqs. (87) on a 200×200 square lattice for different values of noise intensity $D_1 = 1.125 \times 10^{-4}$, $D_2 = 3.125 \times 10^{-4}$ and $D_3 = 5 \times 10^{-3}$. Other parameters are $\epsilon = 0.01$, $W = 0.05$ [118].

the phase of external periodic force or, otherwise, the phase of another periodic oscillator coupled with the first one, then the condition of synchronization can be formalized as

$$|m \cdot \Phi(t) - n \cdot \Psi(t)| < \text{const} \ , \tag{88}$$

where m and n are integers. This conditions defines locking of two phases $\Phi(t)$ and $\Psi(t)$, and requires that the phase difference be a bounded function of time. In other words, periodic oscillations should be in phase.

Synchronization is also defined as frequency entrainment, provided that the frequencies of the oscillator and the driving force are in a rational relation. Here we consider the simplest case of $1:1$ synchronization ($m = n = 1$). When noise is taken into account, the condition for synchronization [Eq. (88)] is never fulfilled. It is a consequence of phase diffusion induced by noise [450]. In the presence of noise, locking epochs of the phase as defined by Eq. (88) are always interrupted by abrupt jumps of the phase difference, also known as phase slips [450]. In the presence of noise, synchronization must be defined in a statistical sense by imposing restrictions on phase and frequency fluctuations [278,451–453].

Frequently, the existence of a well-expressed maximum in the probability density of the phase difference is used as an indicator of synchronization [453,454]. But the fluctuations can also be characterized in terms of the effective diffusion coefficient of the phase difference [450,278]. This

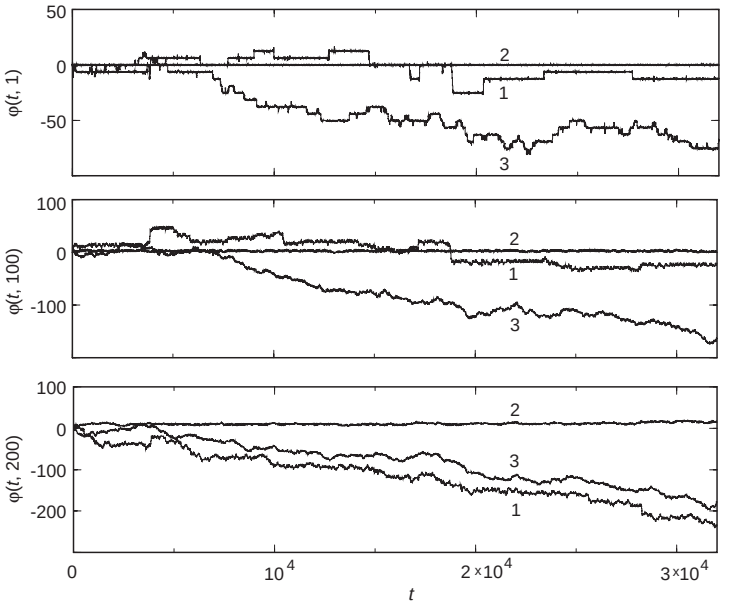

Fig. 59. Phase differences between indicated oscillators for the same values of noise intensity as in the previous figure [118].

diffusion coefficient is inversely proportional to the average length of locking epochs of the phase [279]. Hence, smaller diffusion coefficients indicate a stronger synchronization.

In Van der Pol oscillators, noise always counteracts synchronization. The effective diffusion constant grows with the increase of noise intensity. However, excitable systems may demonstrate quite opposite effects. In these systems certain time scales depends on noise due to the existence of thresholds. Noise can improve synchronization, as shown in [118,278].

To study the effect of noise-induced coherent oscillations described above, we must first define phases of elements in the network. This can be done in different ways (see Ref. [452]). Here we introduce the instantaneous phase $\Phi(t,n)$ of the nth element using the analytic signal representation [433,453,452]. The analytic signal $z(t,n)$ is defined as $z(t,n) = u(t,n) + \mathrm{i}y(t,n)$, where $y(t,n)$ is the Hilbert transform of the original variable $u(n,t)$ in the time domain: $y(t,n) = (1/\pi)\int_{-\infty}^{\infty}(u(\tau,n)/(t-\tau))\,\mathrm{d}\tau$, and $\Phi(t,n) = \arctan[y(t,n)/u(t,n)]$.

For simplicity we consider the one-dimensional version of Eqs. (87), choose the central cell ($n = N/2$) as a reference element, and then calculate the phase differences $\phi(t,k) = \Phi(t,N/2) - \Phi(t,N/2+k)$, $k = -N/2,\ldots,N/2$. The result of calculating the phase differences is shown in Fig. 59 for three values of the noise intensity. For the optimal noise level the phases of different oscillators are locked during the total computation time. In the case of large distances between oscillators the phase fluctuations do indeed grow. Nevertheless, the phase difference is still bounded during long periods of time in a certain range. For non-optimal noise intensities, a partial phase synchronization with randomly occurring phase slips can be observed only between neighboring elements (top graph). For larger distances the diffusion of the phase differences becomes very strong and synchronization breaks down.

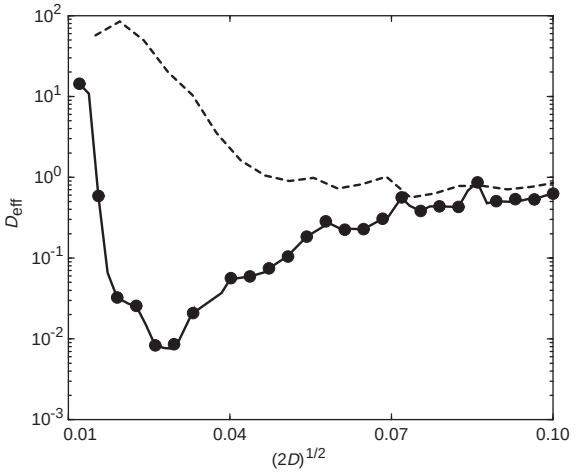

Fig. 60. The averaged effective cross-diffusion coefficient versus noise intensity. Other parameters are the same as in the previous figure. The dashed line correspond to uncoupled lattice ($W = 0$) [118].

In our case, an appropriate measure of stochastic synchronization is the cross-diffusion coefficient, defined as

$$D_{\rm eff}(k) = \frac{1}{2}\frac{\rm d}{{\rm d}t}[\langle\phi^2(t,k)\rangle - \langle\phi(t,k)\rangle^2] \ . \tag{89}$$

This quantity describes the spreading in time of an initial distribution of the phase difference between the $N/2$th and all other elements. A single measure, the spatially averaged effective diffusion coefficient, is obtained by averaging $D_{\rm eff}(k)$ over the spatial distance:

$$D_{\rm eff} = \frac{1}{N}\sum_{k=-N/2}^{N/2} D_{\rm eff}(k) \ . \tag{90}$$

The dependence of this averaged effective cross-diffusion constant on noise intensity is shown in Fig. 60, which displays a global minimum at non-zero noise level. Thus, phase synchronization can be enhanced by tuning the noise intensity.

6.4.3. *Frequency locking*

Let us now characterize synchronization in terms of frequency locking. In our case of stochastic oscillations, we must use the mean frequencies $\langle\omega(n)\rangle = \langle\dot{\Phi}(t,n)\rangle$ of the oscillators [450]. Due to the given distribution of the excitability parameter $a(n)$, the elements in the network have different randomly scattered frequencies for vanishing coupling. We have numerically determined the distribution of the mean frequencies, calculated for every element across the network, $P(\langle\omega\rangle)$, for different noise intensities.

The results are shown in Fig. 61. A remarkable effect of noise-enhanced synchronization can be seen from this figure. For the optimal noise intensity, when the phases of different oscillators are locked for long periods of time, the mean frequencies are entrained and the distribution of the mean

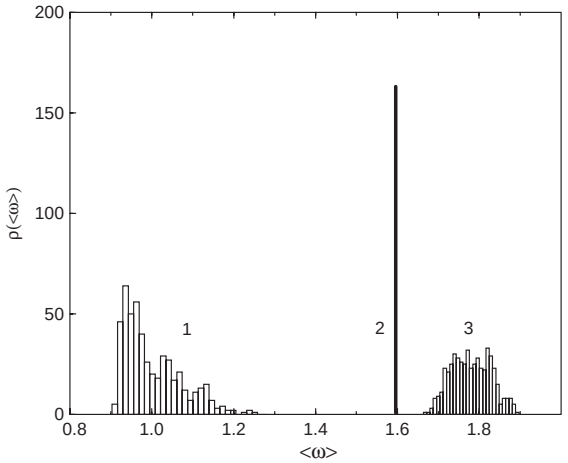

Fig. 61. Distribution of the mean frequencies of oscillators for the values of noise intensity as in Fig. 59 [118].

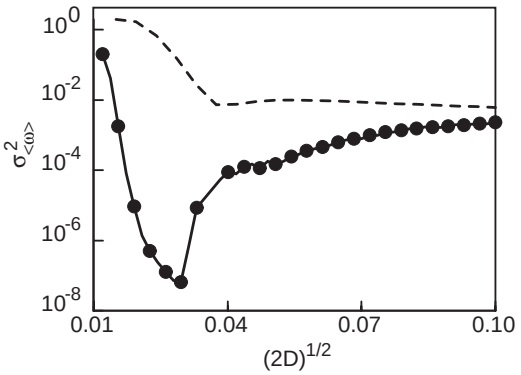

Fig. 62. Mean square deviation of the average frequencies versus noise intensity [118].

frequencies becomes extremely narrow. For non-optimal noises the mean frequencies show rather wide distributions indicating the lack of synchronization.

The last figure clearly indicates noise-induced space–time ordering in the system, based on the synchronization mechanism. This behavior can be quantified further by calculating the mean square deviation of the mean frequencies averaged over the network,

$$\sigma^2_{\langle\omega\rangle} = \frac{1}{N}\sum_{n=1}^{N}\langle\omega(n)^2\rangle - \left[\frac{1}{N}\sum_{n=1}^{N}\langle\omega(n)\rangle\right]^2 . \tag{91}$$

The dependence of the mean square deviation of the mean frequencies versus noise intensity is shown in Fig. 62, and displays vanishing frequency fluctuations at the optimal noise intensity.

The mechanism of noise-induced coherent oscillations and synchronization is rooted in the behavior of a single uncoupled element. The noise-induced oscillations in separate FN elements are most coherent at a non-zero noise intensity, and the quality factor of the noise-induced peak in the power

spectrum is maximal. In this regime, the mean frequency of the system approaches the peak frequency in the power spectrum. In the case of weak noise, the mean frequency depends exponentially on the control parameter a ($a > 1$). However, with the increase of noise the dependence of the mean frequency on a becomes very weak. That is why when noise increases from a very low level, the mismatch between the characteristic frequencies of the elements in the coupled array decreases, providing better conditions for mutual synchronization.

On the other hand, the noise-induced oscillations become more coherent. These effects will tend to facilitate synchronization among elements in the network. Large noise, alternatively, destroys again the coherence of local stochastic oscillations (the frequency and phase fluctuations grow rapidly) and also leads to destruction of spatial coherent structures. The optimal noise intensity at which synchronization is most pronounced depends on the range of the distribution of activation parameters $a(n)$: with the increase of the range of disorder the optimal noise intensity shifts towards smaller values.

7. Noise in excitable spatio-temporal structures

In the previous section we have seen that external fluctuations are able to induce collective behavior, in the form of synchronized firing, in spatially distributed excitable systems. But one of the most defining characteristics of excitable media is their ability to sustain propagation of nontrivial spatio-temporal structures, such as one-dimensional pulses, two-dimensional wavefronts and spirals, and three-dimensional scroll waves [3]. It is thus natural to investigate the effect of noise in the formation and propagation of these structures.

The influence of noise on the spatio-temporal structures exhibited by an excitable medium was first studied by means of a cellular automaton model consisting of a coupled set of LIF neurons [378]. This model exhibited excitable structures (in the form of spiral waves) of optimal shape for an intermediate noise level, in what the authors interpreted as a realization of spatio-temporal stochastic resonance [130]. One of the first experimental investigations in this area addressed the effect of time-independent spatial noise (*quenched* noise) on the propagation of excitable fronts in the photosensitive Belousov–Zhabotinsky reaction [194]. The results showed that propagation of planar pulses in two dimensions was enhanced by noise (in the form of an increase in propagation speed). Other early experimental studies involved the same type of excitable medium, now in the presence of spatio-temporal noise. It was shown that pulse propagation could be sustained by noise in subexcitable media (where no propagation could occur in the absence of noise); the effect had a resonant character, being optimal for an intermediate amount of noise [190]. Recently a noise-induced transition from the excitable to the oscillatory regime has also been observed in the same experimental system [198], and the opposite transition, namely from oscillatory to excitable behavior, has been predicted [455]. These last two situations have been explained analytically in terms of a small noise expansion that converts the stochastic dynamics in an effective deterministic dynamics [456].

From a physiological perspective, experiments have also shown that calcium waves in cultured networks of glial cells are induced by noise (as controlled by the neurotransmitter concentration) [192]. Finally, it should also be noted that the space and time correlation of the noise have been seen to be relevant in the Brownian motion of spiral waves [196] and in the lifetime of scroll rings in three-dimensional excitable media [197].

In what follows, we analyze the influence of different types of *multiplicative* random fluctuations on a FN with activator diffusion. We will see that this kind of noise induces nontrivial spatio-temporal structures in the system, by changing in an effective way the local dynamics of the medium.

It is known that multiplicative noise, in connection with moderate nonvanishing coupling, is able to originate phase transitions in extended media. Bistable behavior with respect to initial conditions or Turing structures were reported for nonlinear media which possess monostable homogeneous phases in a deterministic description. Such bifurcations were called noise-induced phase transitions [141,457–465].

Noise-induced phase transitions have their origin in strong multiplicative noise, which shakes the system out of its monostable configuration. A simple recipe might be to "heat" a previously stable state whereas other regions in the state space are "cooled" [466,467]. The noise strength has to be large enough to exceed the linear restoring force and to enhance nonlinear behavior. In zero-dimensional systems, the new states that occur as a compromise between the deterministic restoring force and the specific heating are overwhelmed by the noisy motion of the order parameter [224]. In coupled systems a new mechanism comes into play: suppression of large fluctuations of the order parameter due to coupling between elements at short time scales [468]. In this case the response of a system can be given in terms of an average trend, expressed by the evolution of the mean order parameter. In this approximation, the influence of the multiplicative noise enters the description via the Stratonovich shift [450,469]. This shift appears as an extra term in the evolution equations for the mean order parameter on top of the deterministic forces. This additional term scales with the noise intensity and occurs if white noise is taken as the limit of a colored noise with vanishing correlation time [142,450].

In coupled systems, the suppression of the noise yields highly stable noise-induced states [470]; escapes between two "stable" situations occur at large time scales only. This fact has even opened the possibility to control escapes between noise-induced phases by additional noise in order, for example, to synchronize these transitions to small periodic signals [471], and to allow propagation of signals via noise-induced bistability [472].

We will now show that multiplicative noise also has nontrivial effects in excitable spatially extended systems. To that end, we will consider a computationally efficient version of the FN introduced by Barkley [217]:

$$\frac{\partial u}{\partial t} = \frac{1}{\varepsilon}\, u(1-u)\left(u - \frac{v+b}{a}\right) + W\nabla^2 u \ ,$$

$$\frac{\partial v}{\partial t} = \gamma u - v \ , \tag{92}$$

where $u(x,t)$ and $v(x,t)$ are the concentrations of the activator and the inhibitor, respectively, with x representing a vector in d-dimensional space. We only take into account diffusion of the activator variable. As usual, the activator evolves on time scales much shorter than the inhibitor, so that $\varepsilon \ll 1$. In what follows, we analyze the effect of fluctuations in some of the parameters of Eqs. (92), when the system operates in different deterministic regimes.

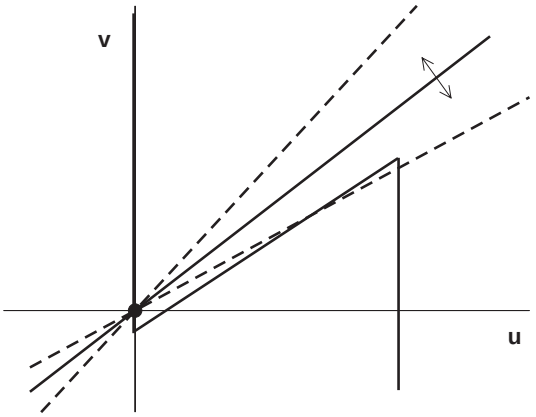

Fig. 63. Nullclines of the Barkley model [Eqs. (92)] in the excitable regime (with solid lines). Only the relevant part of the vertical u-nullclines is shown. Dashed lines show schematically the fluctuations of the v-nullcline. The solid circle denotes the only deterministic steady state of the system.

7.1. Noise-induced spiral dynamics

We first consider the behavior of Eqs. (92) in a deterministically excitable regime, in which the system possesses a single stable steady state. Even in the absence of fluctuations, this system can exhibit a self-sustained spatio-temporal structure in two dimensions in the form of a spiral wave [473]. Once formed (by suitable initial conditions, for instance), this structure becomes in fact very robust. In last years, on the other hand, great interest has been directed towards establishing the conditions under which spiral waves become unstable. Such *spiral breakup*, which has been related to the appearance of ventricular fibrillation in human hearts [474], has been observed experimentally in chemical excitable media [475–478]. Furthermore, the resulting turbulent state has become a standard example of spatio-temporal chaos [479,480].

From a theoretical viewpoint, it is well established that spiral breakup cannot occur in the standard FN. These models can only exhibit the phenomenon when generalized to take into account delayed inhibitor production [481,482], modified inhibitor dynamics [483,484], or advection [485]. Here we show that these effects are not necessary to provide a mechanism of breakup, as long as we consider the existence of a multiplicative noise term in the model. Such a term arises from assuming that the parameter γ in the inhibitor equation of Eqs. (92) fluctuates around a nonzero value, $\gamma = \gamma_0 + \eta(x,t)$, with $\eta(x,t)$ representing a Gaussian noise with zero mean and white in space and time:

$$\langle \eta(x,t)\eta(x',t')\rangle = 2D\delta(t-t')\delta(x-x') \ , \tag{93}$$

with D being the noise intensity. We choose values of the parameters for which the system operates in the excitable regime ($\varepsilon = 0.02$, $a = 0.85$, $b = 0.1$, and $\gamma_0 = 1$). For these parameter values, the nullclines of the model are the ones represented in Fig. 63. As shown in the figure, the effect of the noise is to produce local and rapidly varying fluctuations in the slope of the v-nullcline around the rest state.

In the absence of multiplicative noise, the system operates in a standard excitable regime which is only able to sustain spatio-temporal structures in the form of stable spiral waves. In this regime,

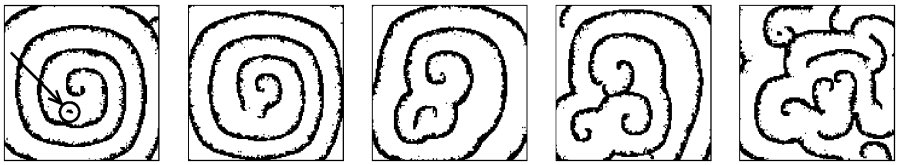

Fig. 64. Time sequence showing spiral breakup leading to complex spiral dynamics [446]. Time flows from left to right. Parameters are $D = 0.0784$ and $W = 1.12$.

excitable wavefronts propagate around the spiral core through resting medium, leaving behind a refractory region which decays to rest before the excitable wave reaches it again. To that end, the local excursion time and the spiral period need to match properly. In the presence of multiplicative noise, the system can become locally bistable at certain time instants, due to the slope fluctuations shown in Fig. 63. When this happens somewhere in the refractory tail of the propagating excitable wavefront, a small region is able to remain in the excited branch some time longer than the surrounding area, as shown by an arrow in the left-most plot of Fig. 64. This excited spot is only able to travel backwards towards the spiral core, since the area between it and the wavefront where it was created is still in the refractory state. Upon propagation, the spot collides with an inner spiral arm and breaks it (second plot from the left in Fig. 64). The resulting wave segments propagate through the structure and lead to further collisions among the different parts of the structure (third and fourth plots from the left in Fig. 64), leading finally to a self-sustained complex state resembling deterministic spiral turbulence [446] (right-most plot in Fig. 64).

Fig. 64 was obtained by integrating numerically Eqs. (92) using a semi-implicit algorithm for the activator equation [486] and an explicit algorithm for the deterministic part of the inhibitor equation. The stochastic term in that equation was introduced by means of a suitable extension of the explicit Euler method [141]. The simulation was performed in a square two-dimensional lattice with 128×128 cells with size $\Delta x = 1$. No-flux (Neumann) boundary conditions were considered, but similar results can be obtained with periodic boundary conditions.

7.1.1. Distribution of space–time clusters

In order to characterize the complexity of the noise-induced structures just described, we analyze the spatio-temporal evolution of the system in terms of coherent space–time clusters [487]. This is done by considering the system evolution in a three-dimensional space formed by the two spatial dimensions and the temporal axis. The activator dynamics is subjected to a threshold procedure that labels the state of each cell as *excited* or *quiescent*, depending on whether or not $u(x,t)$ exceeds a given reference value (here we used $u_{\mathrm{th}} = 0.5$). The evolution of this binary field is considered at discrete time intervals. A cluster is defined as a connected set of excited sites in the three-dimensional cubic grid, where connections are checked with both nearest neighbors and diagonal next-nearest neighbors. According to this definition, a perfect spiral wave in an infinite spatial domain corresponds to a single space–time cluster, whereas a spiral turbulent state exhibits a large number of clusters. This method allows a quantitative measure of the complexity of a spatially-evolving structure: the larger the number of clusters, the larger the complexity of the spatio-temporal dynamics.

We now apply the method described above to the spiral dynamical states induced by noise displayed by the Barkley model. Fig. 65(a) shows the number n_{cl} of coherent space–time clusters,

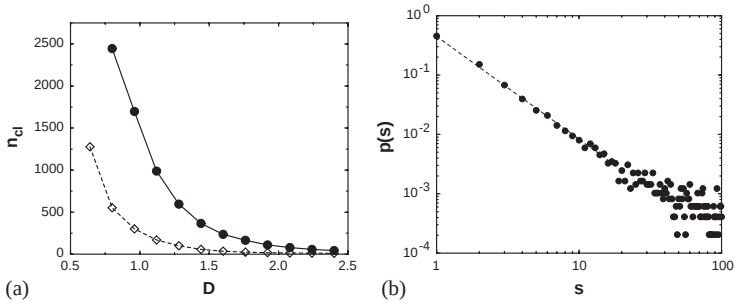

Fig. 65. Statistics of coherent space–time clusters [446]: (a) average number of clusters n_{cl} vs. coupling strength W for $D = 0.0784$ (empty diamonds) and $D = 0.16$ (solid circles); (b) cluster-size distribution for $W = 0.10$ and $D = 0.24$, the dotted line corresponds to a power-law fit with $\alpha = 1.73$ (see text).

averaged over 100 realizations, for increasing values of the coupling strength and two fixed values of the noise strength. The figure shows that n_{cl} decreases sharply as W increases, although there is no sharp transition between the regimes of stable spirals and complex spiral dynamics. In any case, the number of clusters increases with increasing noise level, as could be expected.

We have also characterized the noise-induced complex dynamics described above by means of the distribution of cluster sizes [487]. Previous works in noise-induced structures have reported distributions in the form of a power law, $p(s) \propto s^{-\alpha}$, where $p(s)$ is the distribution function, s is the space–time size of the clusters, and the exponent α has been identified to be [191] approximately between 2 and 3. In our case, the result is shown in Fig. 65(b), for parameters W and D that ensure a large number of clusters (around 5000 in all cases examined). The measured distribution fits reasonably well a power law (spanning 1.5 decades in s) with exponent $\alpha \approx 1.75 \pm 0.05$. This result is seen not to depend noticeably on neither the coupling strength nor the noise intensity, as long as these parameters provide a turbulent state.

7.2. Noise-induced pulse propagation

We have seen that sudden (and local) excursions of the excitable FN into the bistable regime due to multiplicative noise are able to produce spiral breakup in an otherwise perfectly regular excitable medium. In what follows we consider the opposite phenomenon, namely the transition from a bistable to an excitable regime due to noise.

Noise has been seen to sustain propagation of fronts in chains of electronic bistable oscillators [195], and of harmonic signals in systems of coupled double-well oscillators [488,489]. The latter kind of systems have also been seen to exhibit pulse propagation sustained by multiplicative noise under particular conditions [490]. However, in general, bistable systems are not suitable for signal transmission, since under normal conditions they only support propagation of fronts. In that situation, an external resetting mechanism is required for the transmission of information-carrying pulses. In what follows, we show that external random fluctuations naturally sustain propagation of pulses in standard models of activator-inhibitor media operating in a deterministically bistable regime, where only propagation of fronts would take place in the absence of noise under simple initial conditions (e.g., as a response to a local perturbation of a homogeneous steady state). This is accomplished

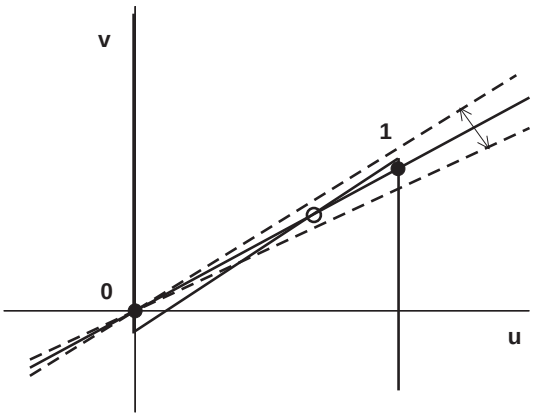

Fig. 66. Nullclines of Eqs. (92) in the bistable regime. Solid circles denote stable fixed points, and the empty circle indicates an unstable fixed point.

by means of a noise-induced transition from the bistable to an excitable regime, as mentioned above. These results could be relevant to understand signal propagation in bistable neural media, given the increasing experimental evidence showing bistable behavior in certain types of neurons, such as thalamocortical neurons [491] and mitral cells [492]. We will analyze two different types of multiplicative noise sources, which will be seen to lead to similar effects. In this way, the phenomenon is shown to be rather generic.

7.2.1. Fluctuations in the inhibitor dynamics

To begin with, we consider again the existence of spatio-temporal fluctuations superimposed to the parameter γ, i.e. $\gamma = \gamma_0 + \eta(x,t)$, with $\eta(x,t)$ representing a Gaussian white noise characterized by correlation [Eq. (93)]. In contrast to the previous section, however, we now choose the deterministic parameters of the model in such a way that the system operates in a deterministically bistable regime, such as the one shown in the phase-plane plot of Fig. 66. The parameters chosen are $\varepsilon = 0.01$, $a = 0.85$, $b = 0.1$, and $\gamma_0 = 0.7$.

In a bistable extended system resting in an homogeneous steady state, the effect of an initial local perturbation of sufficient intensity is to induce a local transition towards the other stable steady state. This transition is propagated into the neighborhood due to spatial coupling, giving rise to a propagating front. This behavior is shown in Fig. 67(a), which displays the space–time evolution of Eqs. (92) in the bistable regime in the absence of noise. When the system is initially in state 0 (as labeled in the phase-plane plot of Fig. 66, and coded in white in Fig. 67) and a perturbation is applied to the left-most site, a transition towards state 1 (coded in black in the figure) starts to propagate through the system towards the right with constant velocity. In this case, simulations are performed in a discrete 1-dimensional lattice of $N = 400$ sites with spacing $\Delta x = 0.25$ and absorbing boundary conditions.

We now consider the effect of the multiplicative noise term introduced above, caused by fluctuations in the parameter γ. We note that, as in the previous section, the effect of this noise on the local dynamics described in Fig. 66 is to introduce fluctuations in the slope of the v-nullcline.

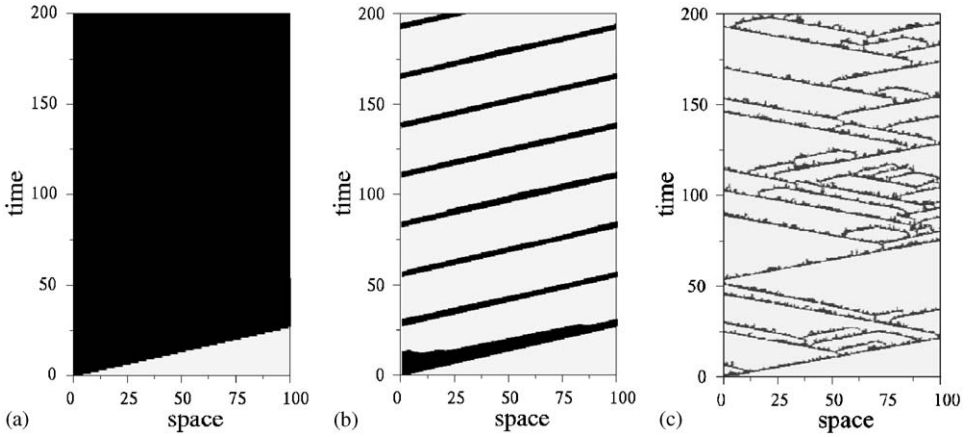

Fig. 67. Spatio-temporal evolution of Eqs. (92), with time running vertically and space horizontally, for increasing noise intensities [493]. Black coding corresponds to $u = 1$, and white to $u = 0$. Parameters used are those of Fig. 66, plus $W = 1$ and $\epsilon = 0.01$. Noise intensity is: (a) $D = 0.0$; (b) $D = 0.0015$; (c) $D = 0.02$.

In the present bistable situation, this produces sudden (and local) transitions into the excitable regime, which destabilize the front solution. The resulting spatio-temporal behavior is shown in Fig. 67(b), where in this case periodic boundary conditions have been used. As a result of the noise-induced destabilization of state 1, a single solitary pulse propagating towards the right is obtained (the symmetrical pulse traveling towards the left has been eliminated for the sake of clarity).

While destabilization of the front solution due to noise is to be expected (since, as mentioned earlier, fluctuations locally push the system away from state 1), the way in which the medium self-organizes to generate a stable traveling pulse is in principle nontrivial. We note that the mechanisms which originate the front and the rear of the pulse are very different. On one hand, the front of the pulse corresponds to the propagation of the excited state 1 into a noise-free region in the rest state 0. Therefore, this transition is basically a deterministic process. The rear jump, on the other hand, corresponds to the propagation of the rest region into a fluctuating excited region. This propagation is initiated by noise, and the corresponding rear front adjusts its speed to that of the leading front, until a stable propagating pulse is formed, similarly to what occurs in purely excitable media [3].

In order to analyze in a quantitative way the effect of the multiplicative noise on the pulse dynamics, we have computed the dependence of the pulse width w on the noise level. The results are plotted in Fig. 68 for two different values of the time-scale ratio ε. In the two cases, the noise-induced pulses become wider as noise increases, up to a certain noise level for which the tendency reverses and the width starts to decrease monotonously with noise. We can intuitively understand the initial growth of w with D by taking into account that a large noise intensity implies large inhibitor fluctuations in the excited (i.e., $u \approx 1$) region. We recall that the rear front of the pulse corresponds to a front propagating from a resting (i.e., $u \approx 0$) towards an excited region. This propagation will be hindered by the existence of large local concentrations of inhibitor in the excited region, such as those produced by intense noise in our model. Therefore, it is to be expected that the larger the noise level, the wider the pulses, as it is certainly observed.

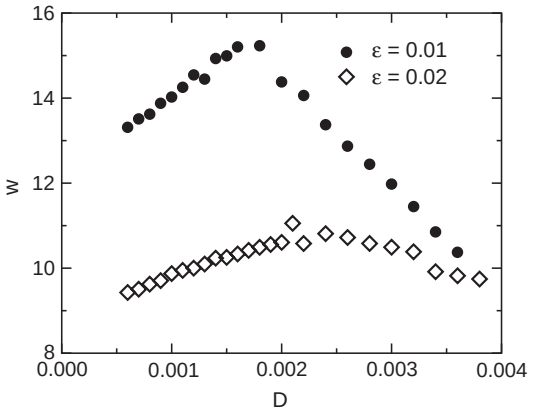

Fig. 68. Pulse width at half-maximum for increasing noise intensity [493]. Parameters are those of Fig. 67.

The monotonic increase in the pulse width with noise intensity breaks down for sufficiently large noise levels. At this point, the fluctuations are intense enough to induce a transition from the excited to the rest state in the middle of the wide pulse, breaking it in two halves. One half continues to move towards the right at the deterministically prescribed speed, whereas the other half starts to move in the opposite direction, with the same absolute velocity. This phenomenon, known as *backfiring*, is shown in the spatio-temporal plot of Fig. 67(c). The backfiring mechanism dominates the whole dynamics of the system, breaking the pulse in two before its tail can adjust its propagation velocity to that of the pulse front. The result is a decrease in the average pulse width with noise intensity.

In the situation shown in Fig. 67(c), the frequency of the backfiring events is so large that the system behavior resembles that of deterministic spatio-temporal turbulence. Both the backfiring and the associated turbulent behavior reported here are not observed in the deterministic version of simple activator–inhibitor models such as the one examined here. Similarly to what happens with spiral breakup in two-dimensional systems, backfiring requires, in the absence of fluctuations, non-standard dynamics of the inhibitor variable, leading to more that one fixed point in the excitable regime [481]. We show here again that the presence of external fluctuations allows for the existence of complex dynamics in this simpler model. In the next paragraphs we show that a similar effect is obtained, although through a different mechanism, with another type of external noise, hinting at the generic character of this noise-induced phenomenon.

7.2.2. Fluctuations in the activator dynamics

We now assume that the external fluctuations affect the parameter b of Eqs. (92), which leads to an additional random term in the activator equation of the form

$$\phi(u) = \frac{1}{a\varepsilon}\, u(u-1)\eta(x,t)\ , \tag{94}$$

where $\eta(x,t)$ is again a Gaussian white noise with zero mean and correlation given by Eq. (93). The assumption of such a multiplicative noise is reasonable, given that equations of the FN constitute

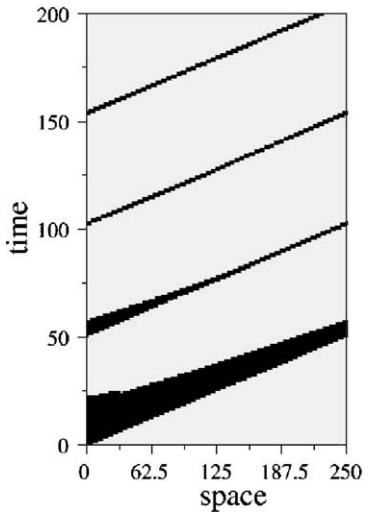

Fig. 69. Spatio-temporal dynamics of the Barkley model in the bistable regime with a fluctuating b parameter [494], for $\varepsilon = 0.01$, $a = 0.85$, $b = 0.12$, $\gamma = 0.7$, $D = 10^{-4}$ and $\Delta x = 0.25$.

a qualitative simplification of the well-known Hodgkin–Huxley model of electrical signalling in neurons, basically consisting in reducing the fast dynamics of the sodium conductance of the cell membrane [4]. In such a reduction process, additive fluctuations of this conductance would readily give rise to multiplicative noise terms in the activator equation. Our simplified choice of the noise term corresponds in fact to a fluctuating excitation threshold (since b is the offset of the tilted u-nullcline in Fig. 66). This is the approach followed in experimental studies of the photosensitive Belousov–Zhabotinsky reaction [190,198], which can be modeled directly by the Barkley equations, with b corresponding to the fluctuating illumination level [191]. We also note that the random term $\phi(u)$ vanishes identically for $u = 0$ and $u = 1$, so that the fluctuations do not perturb the system neither in the rest nor in the excited state. This is very different from an additive noise, or from the type of multiplicative noise considered in the previous section, where the fluctuations actively perturb the system in some or all of the fixed points. In particular, the noise we consider here is not able to induce a decay from one of the stable steady states towards the other.

We choose again values of the parameters for which the system operates in a deterministically bistable regime: $\varepsilon = 0.01$, $a = 0.85$, $b = 0.12$, and $\gamma = 0.7$. For these parameters, the phase-plane plot looks qualitatively equal to Fig. 66, and the corresponding spatio-temporal evolution in the absence of noise is similar to the one shown in Fig. 67(a). As the noise intensity is increased, a sharp transition is observed towards an excitable regime, in which the system behaves as shown in Fig. 69.

We note that, as mentioned above, fluctuations cannot induce in this situation a decay of the "excited" stable state (coded in black in Fig. 69), due to the form of the noise term in Eq. (94), which becomes zero for $u = 1$. Hence, the mechanism through which the transition occurs has to be different from the one leading to a similar effect in the previous section. In order to establish the role of the multiplicative noise $\eta(x,t)$ in this case, we note that the random term in Eq. (94) has

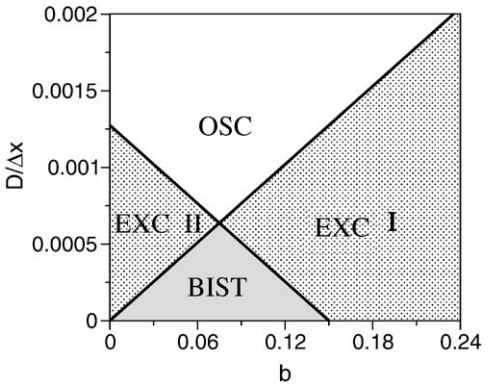

Fig. 70. Phase diagram of the Barkley model with external noise as a function of b and the noise intensity [494]. Other parameters are those of Fig. 69.

a nonzero mean equal to [141]

$$\langle \phi \rangle = \frac{D}{\varepsilon^2 a^2 \Delta x} \langle u(u-1)(2u-1) \rangle \ , \tag{95}$$

where the brackets denote averaging over the probability distribution of the multiplicative noise, which is interpreted in the Stratonovich sense. The spatial discretization Δx of the lattice needs to be considered explicitly in the calculations in order to interpret correctly the spatially extended multiplicative noise [141]; it corresponds to an effective spatial correlation length of the noise.

The random term of Eq. (95) gives rise to a systematic nonzero term contributing to the average dynamics of the system. This systematic contribution can be incorporated explicitly into the activator equation as the first-order term of a small-noise expansion [141], with the remaining stochastic contributions of the noise averaging out to zero. This leads to an effective equation for the activator dynamics with renormalized parameters:

$$\begin{aligned} a' &= a - \frac{2D}{\varepsilon a \Delta x} \ , \\ b' &= b - \frac{D}{\varepsilon a \Delta x} \ , \\ \varepsilon' &= \frac{\varepsilon}{1 - 2D/(\varepsilon a^2 \Delta x)} \ . \end{aligned} \tag{96}$$

We note that even though the random fluctuations were originated in the parameter b, they produce a renormalization of all three parameters of the activator dynamics. A similar renormalization effect as the one reported here has been recently seen to lead to symmetry enhancement in an asymmetric bistable FN, and hence to increased coherence when additive noise is also added [322]. A straightforward analysis in the present case shows how the number and type of fixed points of the local dynamics of the model depend on these parameters, and the results can be plotted in the phase diagram shown in Fig. 70. In this diagram one can see that the transition between the bistable and excitable regimes (labeled BIST and EXC, respectively, in the figure), which in the absence of noise occurs at $b = 0.15$ for the parameters chosen, is shifted in the direction of shrinking the bistable

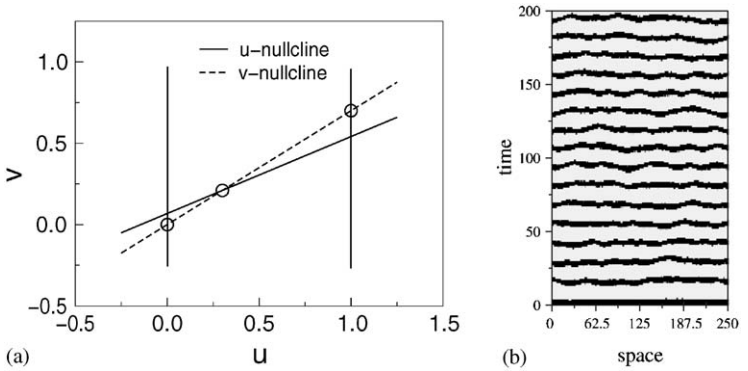

Fig. 71. Noise-induced oscillatory dynamics in the deterministic bistable regime [494]: (a) effective nullclines and (b) corresponding spatio-temporal behavior for $D = 4 \times 10^{-4}$ and $\Delta x = 0.25$.

region as the noise intensity increases. Two different excitable regimes are obtained, labeled EXC I and EXC II, which are symmetric and correspond to either $u = 0$ or $u = 1$, respectively, being the only stable fixed points of the dynamics. Deterministically, the regime EXC II arises for negative values of b. In any case, noise is seen to produce a substantial enlargement of the excitable region, in such a way that a deterministically bistable medium can become excitable for large enough intensity of the multiplicative noise. This is the situation described above in Fig. 69. We stress again that this effect cannot be merely due to a noise-induced decay from the metastable state 1, since the random term of Eq. (94) vanishes in that state. Hence, this behavior must correspond to a dynamical destabilization of state 1 due to the fluctuations, leading to a noise-induced transition denoted by the corresponding line in the phase diagram of Fig. 70. The existence of this transition is confirmed by extensive numerical simulations, which show a well-defined change from bistable to excitable behavior as the noise intensity surpasses its critical value. Below the transition line the system develops fronts systematically, independently of the noise realization, whereas above it pulses are the only stable structures of the system, and fronts cannot be obtained no matter the initial conditions considered.

The phase diagram of Fig. 70 shows another feature arising for large noise strengths. An increase in the noise intensity produces a reduction in the effective slope of the tilted u-nullcline (controlled by a). At a certain point, the reduction is so large that the two stable fixed points 0 and 1 turn unstable, and the system enters an oscillatory regime (labeled OSC in Fig. 70). The corresponding phase-plane plot is shown in Fig. 71(a). Such noise induced transition towards an oscillatory regime has been observed experimentally in deterministically excitable media [198]. The spatio-temporal behavior in this case is represented in Fig. 71(b), where random initial conditions have been chosen. We note that such an oscillatory dynamics does not exist in the deterministic system for any value of b, given the values of $a > \gamma$ chosen here. Furthermore, it can be seen that the dynamics shown in Fig. 71(b) shuts down to the rest state 0 as soon as the external noise is switched off.

7.2.3. Characterizing the noise-induced pulses

We can also use the effective model derived above to predict the characteristics of the propagating pulses, such as their speed and width. One can easily evaluate the pulse speed in an approximate

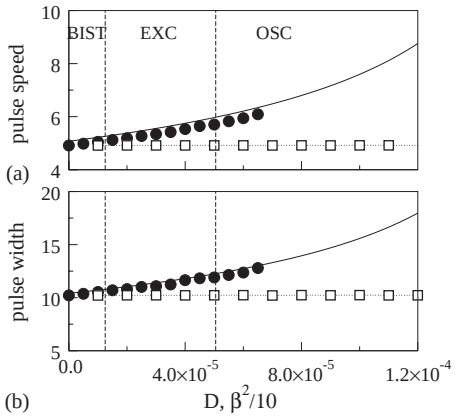

Fig. 72. Pulse speed (a) and width (b) versus noise intensity [494]. Parameters are those of Fig. 69, except $\Delta x = 0.05$. Solid lines represent the analytic results from the effective theory, and symbols numerical simulations in a lattice of 1000 sites, with full circles corresponding to multiplicative noise of intensity D, and empty squares to additive noise of intensity β^2. Vertical dashed lines denote the transitions occurring as the multiplicative noise is increased.

way by assuming a vanishingly small ε. In that approximation, the speed of the leading front of the pulse (the one going from $u = 0$ to $u = 1$), which corresponds in fact to the speed of the pulse itself, can be easily determined [3]:

$$c = \frac{1}{\sqrt{2\varepsilon'}}\left(1 - 2\frac{b'}{a'}\right) , \tag{97}$$

where the renormalized parameters a', b' and ε' are given by Eqs. (96). The result is plotted in Fig. 72(a), which compares the theoretical result in Eq. (97), represented by a solid line, with simulations shown by full circles. The pulse speed grows with increasing noise intensity, and in agreement with previous results on front propagation in one-component bistable media [495]. In the figure two transitions are observed, represented by vertical dashed lines. The first transition leads to the excitable regime, and the second one to the oscillatory regime. Pulses in the bistable regime are obtained only by special initial conditions. In the oscillatory regime a pulse train is obtained, from which the speed of a single pulse can be measured.

It is instructive to compare the effect of our multiplicative noise with that of additive noise. We add to the activator equation a Gaussian noise, white in space and time with zero mean and intensity β^2. The speed of the pulse in the presence of additive noise (but without multiplicative noise) is represented as empty squares in Fig. 72(a). Note that, even though additive noise is also able to produce excitable pulses in the bistable regime (by means of a noise-induced decay mechanism), it does not vary the speed of propagation of the pulses, and hence it does not affect the system dynamics (and does not produce the transitions indicated in the figure).

Once the pulse speed c has been obtained, one can also easily evaluate the pulse width $w = cT$, where T is the time during which the system stays at the excited branch. From the inhibitor equation

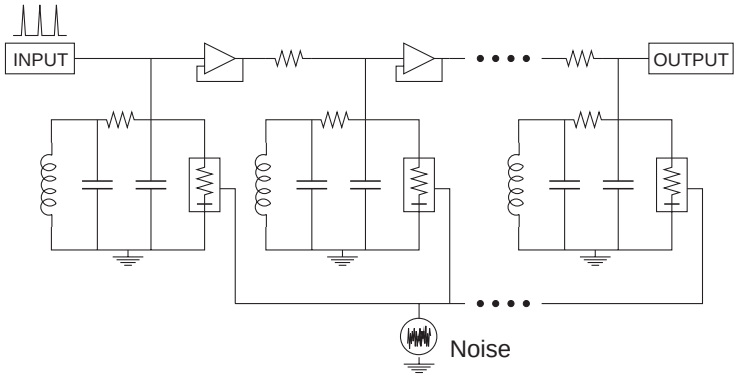

Fig. 73. Schematic representation of the nonlinear circuit array. The boxed element in each unit is the so-called Chua diode [497].

of Eqs. (92), and assuming again a vanishingly small ε, this quantity can be found to be

$$T = \int_0^{v_m} \mathrm{d}v/g(1,v) \ , \tag{98}$$

where v_m is the maximum value reached by the inhibitor v, which can be calculated by imposing that the speeds of the leading and trailing fronts of the pulse are equal [3]. The result in this case is $v_m = a' - 2b'$, which according to Eq. (96) is independent of the noise intensity. Hence T is also independent of the noise strength, and the pulse width is given by

$$w = c \ln \frac{\gamma}{\gamma + 2b - a} \ . \tag{99}$$

We can thus see that the pulse width also increases with noise intensity, as shown by the solid line in Fig. 72(b) and by the numerical simulation results represented by full circles in the figure. On the other hand, and as in the case of the pulse speed, additive noise does not modify the pulse width.

7.2.4. Experimental realization in a chain of electronic circuits

Since the first proposals of using electronic transmission lines to model neural communication [200], many electronic circuits exhibiting nonlinear dynamical behavior have been developed. A particularly fruitful example has been the so-called Chua circuit [496], which is characterized by its ability to operate in different dynamical regimes, including chaotic, oscillatory, excitable and bistable regimes. For this reason, Chua circuit is a convenient candidate to examine experimentally the noise-induced phenomena described in the previous paragraphs. We will now describe a simplified version of the Chua circuit that exhibits a transition from bistable to excitable dynamics in terms of a single control parameter. We will show that random fluctuations affecting this control parameter advance the transition towards excitability, and thus enhance the excitable behavior of the system, allowing the propagation of excitable pulses even under deterministically bistable conditions. The experimental implementation is shown schematically in Fig. 73. Twenty nonlinear electronic oscillators are coupled unidirectionally through operational amplifiers, and the first circuit is driven by a periodic train of short pulses. The output at the last circuit is analyzed when all the elements in the chain are affected globally by a controlled source of electronic noise.

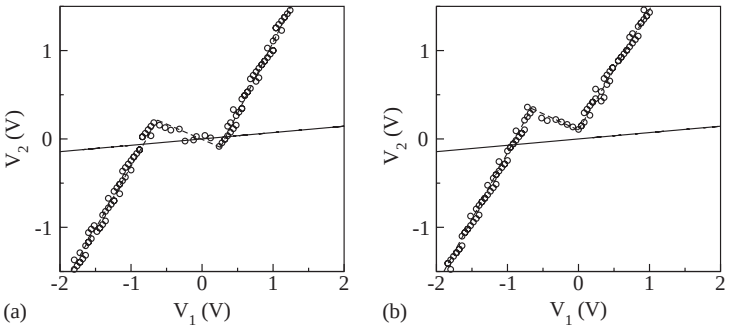

Fig. 74. Nullclines of the isolated circuit in the reduced plane V_1–V_2 for two different values of the positive supply voltage V_+: (a) $V_+ = 2$ V, bistable dynamics; (b) $V_+ = 0$ V, excitable dynamics. The solid line corresponds to the V_2-nullcline, and the circles to the V_1-nullcline [497].

The dynamics of each individual circuit of the chain is governed by the equations:

$$C_1 \frac{\mathrm{d}V_1}{\mathrm{d}t} = \frac{V_2 - V_1}{R} - g(V_1, V_+) \ , \tag{100}$$

$$C_2 \frac{\mathrm{d}V_2}{\mathrm{d}t} = \frac{V_1 - V_2}{R} + I_L \ , \tag{101}$$

$$L \frac{\mathrm{d}I_L}{\mathrm{d}t} = -V_2 - r_L I_L \ , \tag{102}$$

where V_i is the voltage drop in the capacitor i, I_L the current through the inductance, r_L its internal resistance (21 Ω in the present setup), and V_+ the positive supply voltage of the Chua diode [497]. The function $g(V_1, V_+)$ represents the characteristic curve of the nonlinear resistor, which is piecewise linear and contains a region of negative resistance.

The nullclines of the system can be drawn in the reduced plane V_1–V_2 by introducing the I_L-nullcline obtained from Eq. (102), $I_L = -V_2/r_L$, into Eqs. (100) and (101). The result is shown in Fig. 74 for two different values of the supply voltage V_+. The V_1-nullcline has been plotted making use of the experimentally measured characteristic $g(V_1, V_+)$ of the nonlinear resistor. As can be seen in the figure, the value of V_+ affects strongly the position of the breaking point where the second slope-discontinuity of that nullcline occurs. In that way, for large values of V_+ [Fig. 74(a)] two steady states exist, corresponding to the two outer crossings between the two nullclines, leading to a bistable situation. On the other hand, for small enough voltage V_+ [Fig. 74(b)] the steady state at $V_1 > 0$ disappears. In this monostable regime, the system behaves in an excitable way, going through large excursions in phase space as a response to sufficiently strong perturbations from its single steady state.

Let us now examine the bistable response of the system (for large V_+) to an external driving in the form of a periodic train of short pulses. This signal drives a solid-state switch through which the capacitor C_1 discharges for a short time (~ 5 μs, much shorter than the characteristic times of the system). This discharge produces a jump from one steady state of the system to the other, as shown in Fig. 75(a). In a biological context, a similar response to periodic trains of pulses has been

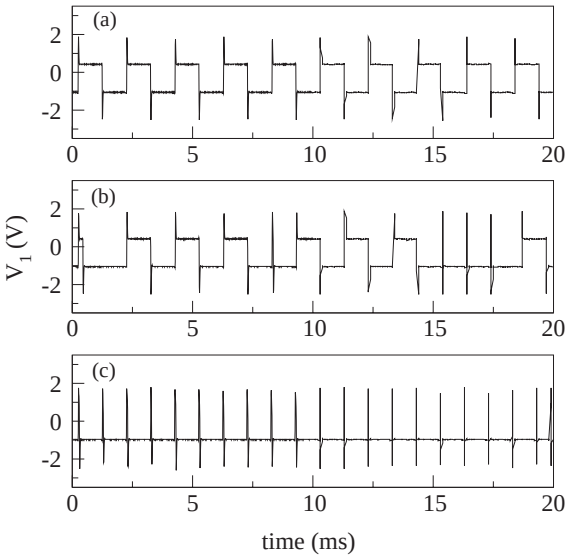

Fig. 75. Response of the last circuit in the chain to a periodic train of pulses applied to the first circuit, for increasing noise intensity [497]. The rms values of the noise time series are: (a) $V_{\text{noise}} = 0.30$ V, (b) $V_{\text{noise}} = 0.42$ V, (c) $V_{\text{noise}} = 0.65$ V.

recently observed in experiments on thalamocortical neurons of cats [491]. The time trace shown in Fig. 75(a) corresponds in fact to the signal measured at the last circuit of the chain, after each jump between steady states has propagated through the array in the form of a front (which is terminated by the next jump).

Noise is generated by amplifying the shot noise of a *pn* junction diode [195], and is introduced in the circuits through the positive supply voltage of the Chua diode [497]. We now examine the effect of this external noise on the front propagation shown in Fig. 75(a). Noise is observed to act in this system in a way similar to that described in the theoretical analysis of the previous sections, increasing the effective value of V_+. This modifies the nullcline scenario from the situation of Fig. 74(a) to that of Fig. 74(b). As a consequence, for a large enough intensity of the external noise, the steady state at $V_1 > 0$ becomes destabilized in such a way that the system starts to behave effectively in an excitable regime. This is confirmed in Figs. 75(b) and (c): for not too large noise, the positive steady state decays only at certain times (and at certain circuits), leading to a mixed train of spiked and squared pulses, as shown in Fig. 75(b). For sufficiently large noise, on the other hand, the positive steady state always decays, and a train of fully excitable pulses propagates through the medium and reaches the last circuit [Fig. 75(c)]. Hence the system behaves as an excitable medium, even though all the circuits have been set in a deterministically bistable regime. This noise-induced transition from a completely bistable to a completely excitable behavior can be characterized, for instance, in terms of the percentage of pulses that reach the last circuit of the chain in the form of a spike, in contrast with the square pulses typical of the bistable regime. Since in the spiked case each circuit is reset after the passage of a bit, one can consider that information transmission is possible in this situation, and thus that percentage represents the *efficiency* of the system as a communication channel. This efficiency parameter increases monotonously with noise intensity [497].

The time taken by the pulses to travel through the chain can be estimated by measuring the delay between the pulses at the first and the last circuits. This delay is inversely related to the propagation speed of the pulse. In contrast to the theoretical results described in the previous sections, where the propagation speed was seen to increase with noise intensity, in this case no clear systematic dependence of the pulse delay with noise strength has been observed. On the other hand, the pulse speed does depend on the coupling resistance between the circuits, decreasing with it as expected. For large enough resistance the pulse speed drops to zero, and propagation can no longer occur: it is the so-called regime of *propagation failure*. In this situation noise is seen to help to sustain propagation, similarly to experimental observations in chains of bistable electronic circuits [195]. In other words, for large enough noise signals can be transmitted even when the coupling resistance is so large that propagation fails under deterministic conditions.

Acknowledgements

We thankfully acknowledge our fruitful continuing collaboration in this topic with R. Bascones, J.M. Buldu, A. Cornell-Bell, S. Feistel, M. Kostur, J. Kurths, A. Longtin, J. Łuczka, L. Meinhold, C. Mirasso, F. Moss, D. Russell, F. Sagués, X. Sailer, J.M. Sancho, M.A. Santos, M.C. Torrent, J. Wehrmeister, A. Zaikin, and M. Zaks and for discussions with V.S. Anishchenko, W. Ebeling, J.A. Freund, P. Hänggi, R. Kawai, Yu.L. Klimontovich, M. Rozenblum, A. Pikovsky, D. Postnov, Yu.M. Romanovsky, I.M. Sokolov, and C. van den Broeck. Special thanks are going to B. Naundorf and T. Prager for providing us with unpublished common results. We acknowledge the fruitful comments of the unknown referee which helped a lot to improve the present publication.

This work was supported by DFG (Germany), under projects Sfb 555 and GK 268, by DAAD (Germany), under project 315/ab,by MCyT (Spain)-FEDER, under projects BFM2001-2159 and BFM2002-04369. A.N. acknowledges support from the NIH (R01 DC04922) and the NSF (INT-0128974). J.G.O. wishes to thank the Alexander von Humboldt-Stiftung for financial support.

References

[1] A.T. Winfree, The Geometry of Biological Time, Springer, New York, 1980.
[2] J.D. Murray, Mathematical Biology, Springer, Berlin–Heidelberg–New York, 1993.
[3] A. Mikhailov, Foundations of Synergetics I, 2nd Edition, Springer, Berlin–Heidelberg–New York, 1994.
[4] J. Keener, J. Sneyd, Mathematical Physiology, Springer, New York, 1998.
[5] E.M. Izhikevich, Int. J. Bifurc. Chaos 10 (2000) 1171.
[6] L. Glass, Nature 410 (2001) 277.
[7] E. Meron, Phys. Rep. 218 (1992) 1.
[8] C.O. Weiss, R. Vilaseca, Dynamics of Lasers, VCH, Weinheim, 1991.
[9] B. Krauskopf, K. Schneider, J. Sieber, S. Wieczorek, M. Wolfrum, Opt. Commun. 215 (2003) 367.
[10] H.J. Wünsche, O. Brox, M. Radziunas, F. Henneberger, Phys. Rev. Lett. 88 (2002) 023901.
[11] M.A. Larotonda, A. Hnilo, J.M. Mendez, A.M. Yacomotti, Phys. Rev. A 65 (2002) 033812.
[12] G.M. Shepherd, Neurobiology, Oxford University Press, New York, 1983.
[13] C. Koch, Biophysics of Computation, Oxford University Press, New York, 1999.
[14] H.A. Braun, M. Wissing, K. Schäfer, M.C. Hirsch, Nature (London) 367 (1994) 270.
[15] R. Kapral, K. Showalter (Eds.), Chemical Waves and Patterns, Kluwer Academic Publishers, Dordrecht, 1995.
[16] A. Ganopolski, S. Rahmstorf, Phys. Rev. Lett. 88 (2002) 038501.

[17] H. Haken, Rev. Mod. Phys. 47 (1975) 67.
[18] A.L. Hodgkin, A.F. Huxley, J. Physiol. (London) 117 (1952) 500.
[19] R.A. FitzHugh, Biophys. J. 1 (1961) 445.
[20] S.H. Strogatz, Nonlinear Dynamics and Chaos with Applications to Physics, Biology, Chemistry, and Engineering, Perseus Books, Cambridge, MA, 1994.
[21] E.A. Jackson, Perspectives of Nonlinear Dynamics, Cambridge University Press, Cambridge, 1989.
[22] J.J. Tyson, J.P. Keener, Physica D 32 (1988) 327.
[23] M.C. Cross, P.C. Hohenberg, Rev. Mod. Phys. 65 (1993) 851.
[24] B.S. Kerner, W.W. Osipov, Autosolitons, Kluwer, Dordrecht, 1994.
[25] F.C. Hoppensteadt, E.M. Izhikevich, Weakly Connected Neural Networks, Springer, New York, 1997.
[26] M. Braune, H. Engel, Chem. Phys. Lett. 211 (1993) 534.
[27] W. Wang, G. Perez, H.A. Cerdeira, Phys. Rev. E 47 (1993) 2893.
[28] S. Grill, V.S. Zykov, S.C. Müller, Phys. Rev. Lett. 75 (1995) 3368.
[29] M. Kim, M. Bertram, M. Pollmann, A.v. Oertzen, A.S. Mikhailov, H.H. Rotermund, G. Ertl, Science 292 (2001) 1357.
[30] G.V. Osipov, B.V. Shulgin, J.J. Collins, Phys. Rev. E 58 (1998) 6955.
[31] M. Roussel, J. Wang, J. Phys. Chem. A 104 (2000) 11751.
[32] I. Sendina-Nadal, E. Mihaliuk E, J.C. Wang, V. Perez-Munuzuri, K. Showalter, Phys. Rev. Lett. 86 (2001) 1646.
[33] T. Sakurai, E. Mihaliuk, F. Chirila, K. Showalter, Science 296 (2002) 2009.
[34] I.Z. Kiss, Y. Zhai, J.L. Hudson, Science 296 (2002) 1676.
[35] P.A. Tass, Europhys. Lett. 55 (2001) 171.
[36] P.A. Tass, Europhys. Lett. 59 (2002) 199.
[37] H. Haken, Advanced Synergetics, Springer, Berlin, Heidelberg, 1985.
[38] G. Nicolis, I. Prigogine, Self-Organization in Non-Equilibrium Systems, Wiley, New York, 1977.
[39] R. Feistel, W. Ebeling, Evolution of Complex Systems, Kluwer, Dordrecht, 1989.
[40] H. Treutlein, K. Schulten, Ber. Bunsenges. Phys. Chem. 89 (1985) 710.
[41] W. Ebeling, H. Herzel, W. Richert, L. Schimansky-Geier, Zeitschr. Angew. Mathem. Mechanik (ZAMM) 66 (1986) 161.
[42] D. Sigeti, W. Horsthemke, J. Stat. Phys. 54 (1989) 1217.
[43] C. Kurrer, K. Schulten, Physica D 50 (1991) 311.
[44] C. Kurrer, K. Schulten, Int. J. Neural Systems 7 (1996) 399.
[45] P.S. Landa, J. Commun. Techn. Electron. 47 (2002) 1323.
[46] U. Hillenbrand, Phys. Rev. E 66 (2002) 021909.
[47] H. Gang, T. Ditzinger, C.Z. Ning, H. Haken, Phys. Rev. Lett. 71 (1993) 807.
[48] A. Pikovsky, J. Kurths, Phys. Rev. Lett. 78 (1997) 775.
[49] A. Longtin, Phys. Rev. E 55 (1997) 868.
[50] A. Neiman, P.I. Saparin, L. Stone, Phys. Rev. E 56 (1997) 270.
[51] J.R. Pradines, G.V. Osipov, J.J. Collins, Phys. Rev. E 60 (1999) 6407.
[52] J.P. Baltanes, J.M. Casado, Physica D 122 (1998) 231.
[53] B. Lindner, L. Schimansky-Geier, Phys. Rev. E 60 (1999) 7270.
[54] V.A. Makarov, V.I. Nekorkin, M.G. Velarde, Phys. Rev. Lett. 86 (2001) 3431.
[55] A.M. Lacasta, F. Sagués, J.M. Sancho, Phys. Rev. E 66 (2002) 045105.
[56] K. Pakdaman, S. Tanabe, T. Shimokawa, Neural Networks 14 (2001) 895.
[57] B. Lindner, L. Schimansky-Geier, A. Longtin, Phys. Rev. E 66 (2002) 031916.
[58] M. Qian, G.-X. Wang, X.-J. Zhang, Phys. Rev. E 62 (2000) 6469.
[59] J.M. Casado, Phys. Lett. A 291 (2001) 82.
[60] S. Wu, W. Ren, K. He, Z. Huang, Phys. Lett. A 279 (2001) 347.
[61] H. Gu, M. Yang, L. Li, Z. Liu, W. Ren, NeuroReport 13 (2002) 1657.
[62] P.L. Gong, J.X. Xu, S.J. Hu, Chaos Solitons Fractals 13 (2002) 885.
[63] S.-G. Lee, A. Neiman, S. Kim, Phys. Rev. E 57 (1998) 3292.
[64] O.V. Sosnovtseva, D. Setsinsky, A. Fausboll, E. Mosekilde, Phys. Rev. E 66 (2002) 041901.
[65] Y. Yu, W. Wang, J. Wang, F. Liu, Phys. Rev. E 63 (2001) 021907.

[66] K. Pakdaman, S. Tanabe, Phys. Rev. E 64 (2001) 050902.
[67] G. Schmid, I. Goychuk, P. Hänggi, Europhys. Lett. 56 (2001) 22.
[68] F. Liu, B. Hu, W. Wang, Phys. Rev. E 63 (2001) 031907.
[69] W.C. Stacey, D.M. Durand, J. Neurophysiol. 88 (2002) 2598.
[70] J.L.A. Dubbeldam, B. Krauskopf, D. Lenstra, Phys. Rev. E 60 (1999) 6580.
[71] J.M. Buldú, J. García-Ojalvo, C.R. Mirasso, M.C. Torrent, J.M. Sancho, Phys. Rev. E 64 (2001) 051109.
[72] S. Zhong, H. Xin, Chem. Phys. Lett. 321 (2000) 309.
[73] S. Zhong, F. Qi, H. Xin, Chem. Phys. Lett. 342 (2001) 583.
[74] P. Jung, J.W. Shuai, Europhys. Lett. 56 (2001) 29.
[75] L. Meinhold, L. Schimansky-Geier, Phys. Rev. E 66 (2002) 050901.
[76] J.Q. Zhang, F. Qi, H.W. Xin, Biophys. Chem. 94 (2001) 201.
[77] R. Castro, T. Sauer, Phys. Rev. E 79 (1997) 1030.
[78] C. Palenzuela, R. Toral, C.R. Mirasso, O. Calvo, J.D. Gunton, Europhys. Lett. 56 (2001) 347.
[79] O. Calvo O, C.R. Mirasso, R. Toral, Electron. Lett. 37 (2001) 1062.
[80] L.Q. Zhu, Y.C. Lai, Z.H. Liu, A. Raghu, Phys. Rev. E 66 (1) (2002) 015204.
[81] Z. Liu, Y.-C. Lai, Phys. Rev. Lett. 86 (2001) 4737.
[82] M. Zhan, G.W. Wei, C.H. Lai, Y.-C. Lai, Z. Liu, Phys. Rev. E 66 (2002) 036201.
[83] R. Rai, H. Singh, Phys. Rev. E 62 (2000) 8804.
[84] A.F. Rozenfeld, C.J. Tessone, E. Albano, H.S. Wio, Phys. Lett. A 280 (2001) 45.
[85] J.L. Cabrera, J. Gorroñogoitia, F.J. de la Rubia, Phys. Rev. E 66 (2002) 022101.
[86] G.S. Jeon, M.Y. Choi, Phys. Rev. B 66 (2002) 064514.
[87] B.J. Kim, P. Minnhagen, H.J. Kim, M.Y. Choi, G.S. Jeon, Europhys. Lett. 56 (2001) 333.
[88] H. Rosé, H. Hempel, L. Schimansky-Geier, Physica A 206 (1994) 421.
[89] L.F. Yang, Z.H. Hou, B.J. Zhou, J. Chem. Phys. 109 (1998) 6456.
[90] O. Kortluke, V.N. Kuzovkov, W. von Niessen, Phys. Rev. Lett. 83 (1999) 3089.
[91] O. Kortluke, V.N. Kuzovkov, W. von Niessen, Phys. Rev. E 66 (2002) 036139.
[92] S. Katsev, I. L'Heureux, Phys. Rev. E 61 (2000) 4972.
[93] L.E. Christiansen, T. Lehn-Schiler, E. Mosekilde, P. Grnsy, H. Matsushita, Math. Comput. Simul. 58 (2002) 385.
[94] F. Baras, Phys. Rev. Lett. 77 (1996) 1398.
[95] J. Dethier, F. Baras, M.M. Mansour, Europhys. Lett. 42 (1998) 19.
[96] Y.J. Jiang, H.W. Xin, Phys. Rev. E 62 (2000) 1846.
[97] M.M. Mansour, J. Dethier, F. Baras, J. Chem. Phys. 114 (2001) 9265.
[98] H. Hong, M.Y. Choi, K. Park, B.-G. Yoon, K.-S. Soh, Phys. Rev. E 60 (1999) 4014.
[99] I.Z. Kiss, J.L. Hudson, G.J. Escalera Santos, P. Parmananda, Phys. Rev. E 67 (2003) 035201(R).
[100] J.M. Casado, Phys. Lett. A 235 (1997) 489.
[101] J.P. Baltanas, J.M. Casado, Phys. Rev. E 65 (2002) 041915.
[102] B. McNamara, K. Wiesenfeld, Phys. Rev. A 39 (1989) 4854.
[103] P. Jung, Phys. Rev. E 50 (1994) 2513.
[104] A. Longtin, J. Stat. Phys. 70 (1993) 309.
[105] K. Wiesenfeld, D. Pierson E. Pantazelou, C. Dames, F. Moss, Phys. Rev. Lett. 72 (1994) 2125.
[106] J.J. Collins, C.C. Chow, Th.T. Imhoff, Phys. Rev. E 52 (1995) R3321.
[107] D. Nozaki, Y. Yamamoto, Phys. Lett. A 243 (1998) 281.
[108] D.R. Chialvo, O. Calvo, D.L. Gonzalez, O. Piro, G.V. Sabino, Phys. Rev. E 65 (2002) 050902(R).
[109] L. Gammaitoni, P. Hänggi, P. Jung, F. Marchesoni, Rev. Mod. Phys. 70 (1998) 223.
[110] B. Lindner, L. Schimansky-Geier, Phys. Rev. E 61 (2000) 6103.
[111] S. Ripoll Massanés, C.P. Pérez Vicente, Phys. Rev. E 59 (1999) 4490.
[112] B. Lindner, L. Schimansky-Geier, Phys. Rev. Lett. 86 (2001) 2934.
[113] H.E. Plesser, T. Geisel, Phys. Rev. E 59 (1999) 7008.
[114] S. Shinomoto, Y. Kuramoto, Progr. Theor. Phys. 75 (1988) 1105.
[115] H. Sakaguchi, S. Shinomoto, Y. Kuramoto, Progr. Theor. Phys. 79 (1988) 600.
[116] Ch. Kurrer, K. Schulten, Phys. Rev. E 51 (1995) 6213.
[117] S. Kim, S.H. Park, H.B. Pyo, Phys. Rev. Lett. 82 (1999) 1620.

[118] A. Neiman, L. Schimansky-Geier, A. Cornell-Bell, F. Moss, Phys. Rev. Lett. 83 (1999) 4896.
[119] C.S. Zhou, J. Kurths, B. Hu, Phys. Rev. Lett. 87 (2001) 098101.
[120] H. Busch, M.T. Hütt, F. Kaiser, Phys. Rev. E 64 (2001) 021105.
[121] C.D.E. Boschi, E. Louis, G. Ortega, Phys. Rev. E 65 (2002) 012901.
[122] Y. Shinohara, T. Kanamaru, H. Suzuki, T. Horita, K. Aihara, Phys. Rev. E 65 (2002) 051906.
[123] J. Pham, K. Pakdaman, J.-F. Vibetr, Phys. Rev. E 58 (1998) 3610.
[124] E. Moro, A. Sánchez, Europhys. Lett. 44 (1998) 409.
[125] S. Tanabe, T. Shimokawa, S. Sato, K. Pakdaman, Phys. Rev. E 60 (1999) 2182.
[126] R.F. Fox, Y. Lu, Phys. Rev. E 49 (1994) 3431.
[127] N. Cohen, Y. Soen, E. Braun, Physica A 249 (1998) 600.
[128] P. Babinec, M. Babincova, Biolelectrochemistry 56 (2002) 167.
[129] R.R. Poznanski, J. Bell, Math. Biosci. 166 (2000) 123.
[130] P. Jung, G. Mayer-Kress, Phys. Rev. Lett. 74 (1995) 2134.
[131] Z.H. Hou, L.F. Yang, X.B Zuo, X. Houwen, Phys. Rev. Lett. 81 (1998) 2854.
[132] H. Busch, F. Kaiser, Acta Phys. Pol. B 31 (2000) 1143.
[133] Y. Zhou, P. Jung, Europhys. Lett. 49 (2000) 695.
[134] I. Sendiña-Nadal, D. Roncaglia, D. Vives, V. Pérez-Muñuzuri, M. Gómez-Gesteira, V. Pérez-Villar, J. Echave, J. Casademunt, L. Ramírez-Piscina L., F. Sagués, Phys. Rev. E 58 (1998) R1183.
[135] D.R. Chialvo, G.A. Cecchi, M.O. Magnasco, Phys. Rev. E 61 (2000) 5654.
[136] G. Balazsi, L.B. Kish, F.E. Moss, Chaos 11 (2001) 563.
[137] M.T. Hutt, R. Neff, H. Busch, F. Kaiser, Phys. Rev. E 66 (2002) 026117.
[138] C.R. Laing, A. Longtin, Physica D 160 (2001) 149.
[139] O.V. Sosnovtseva, A.I. Fomin, D.E. Postnov, A.V. Anishchenko, Phys. Rev. E 64 (2001) 026204.
[140] M.A. Santos, C. Zülicke, L. Schimansky-Geier, Phys. Lett. A 290 (2001) 270.
[141] J. García-Ojalvo, J.M. Sancho, Noise in Spatially Extended Systems, Springer, New York, 1999.
[142] V. Anishchenko, V.V. Astakhov, A.B. Neiman, T. Vadivasova, L. Schimansky-Geier, Nonlinear Dynamics of Chaotic and Stochastic Systems, Springer, Berlin–Heidelberg–New York, 2002.
[143] H. Hempel, L. Schimansky-Geier, J. García-Ojalvo, Phys. Rev. Lett. 82 (1999) 3713.
[144] B. Hu, C.S. Zhou, Phys. Rev. E 61 (2000) R1001.
[145] Y. Wang, D.T.W. Chik, Z.D. Wang, Phys. Rev. E 61 (2000) 740.
[146] E.I. Volkov, D.V. Volkov, Phys. Rev. E 65 (2002) 046232.
[147] O. Carrillo, M.A. Santos, J. García-Ojalvo, J.M. Sancho, Europhys. Lett. (2004), in press.
[148] L. I, J.-M. Liu, Phys. Rev. Lett. 74 (1995) 3161.
[149] D.E. Postnov, S.K. Han, T.G. Yim, O.V. Sosnovtseva, Phys. Rev. E 59 (1999) R3791.
[150] Y. Horikawa, Phys. Rev. E 64 (2001) 031905.
[151] D.E. Postnov, O.V. Sosnovtseva, S.K. Han, W.S. Kim, Phys. Rev. E 66 (2002) 016203.
[152] A.P. Nikitin, Tech. Phys. Lett. 27 (2001) 908.
[153] G. Giacomelli, M. Giudici, S. Balle, J.R. Tredicce, Phys. Rev. Lett. 84 (2000) 3298.
[154] S. Barbay, G. Giacomelli, F. Marin, Phys. Rev. Lett. 85 (2000) 4652.
[155] F. Marino, M. Giudici, S. Barland, S. Balle, Phys. Rev. Lett. 88 (2002) 040601.
[156] A.M. Yacomotti, G.B. Mindlin, M. Giudici, S. Balle, S. Barland, J. Tredicce, Phys. Rev. E 66 (2002) 036227.
[157] Z. Hou, H. Xin, J. Phys. Chem. A 103 (1999) 6181.
[158] S. Zhong, H. Xin, J. Phys. Chem. A 104 (2000) 297.
[159] Y. Jiang, Shi Zhong, H. Xin, J. Phys. Chem. A 104 (2000) 8521.
[160] Q.S. Li, R. Zhu, J. Chem. Phys. 115 (2001) 6590.
[161] K. Miyakawa, H. Isikawa, Phys. Rev. E 66 (2002) 046204.
[162] K. Miyakawa, T. Tanaka, H. Isikawa, Phys. Rev. E 67 (2003) 066206.
[163] S. Zhong, H.W. Xin, Chem. Phys. Lett. 333 (2001) 133.
[164] L.Q. Zhou, X. Jia, Q. Ouyang, Phys. Rev. Lett. 88 (2002) 138301.
[165] D. Wilkowski, J. Ringot, D. Hennequin, J.C. Garreau, Phys. Rev. Lett. 85 (2000) 1839.
[166] E. Manjarrez, J.G. Rojas-Piloni, I. Méndez, L. Martínez, D. Vélez D, Neurosci. Lett. 326 (2002) 93.
[167] J.K. Douglass, L. Wilkens, E. Pantazelou, F. Moss, Nature 365 (1993) 337.

[168] S. Bahar, A. Neiman, L.A. Wilkens, F. Moss, Phys. Rev. E 65 (2002) 050901(R).
[169] J.E. Levin, J.P. Miller, Nature 380 (1996) 165.
[170] J.J. Collins, T.T. Imhoff, P. Grigg, J. Neurophysiol. 79 (1998) 1879.
[171] F. Jaramillo, K. Wiesenfeld, Nat. Neurosci. 1 (1998) 384.
[172] M. Rudolph, A. Destexhe, J. Comput. Neurosci. 11 (2001) 19.
[173] F. Moss, Int. J. Psychophysiol. 45 (2002) 61.
[174] B.J. Gluckman, T.I. Netoff, E.J. Neel, W.L. Ditto, M.L. Spano, S.J. Schiff, Phys. Rev. Lett. 77 (1996) 4098.
[175] T. Mori, S. Kai, Phys. Rev. Lett. 88 (2002) 218101.
[176] A. Guderian, G. Dechert, K.P. Zeyer, F.W. Schneider, J. Phys. Chem. 100 (1996) 4437.
[177] A. Förster, M. Merget, F.W. Schneider, J. Phys. Chem. 100 (1996) 4442.
[178] W. Hohmann, J. Müller, F.W. Schneider, J. Phys. Chem. 100 (1996) 5388.
[179] T. Ameniya, T. Ohmori, M. Nakaiwa, T. Yamguchi, J. Phys. Chem. A 102 (1998) 4537.
[180] T. Ameniya, T. Ohmori, T. Yamamoto, T. Yamguchi, J. Phys. Chem A 103 (1999) 3451.
[181] S.M. Bezrukov, I. Vodyanoy, Nature 378 (1995) 362.
[182] D.F. Russell, L.A. Wilkens, F. Moss, Nature 402 (1999) 291.
[183] J.A. Freund, J. Kienert, L. Schimansky-Geier, B. Beisner, A. Neiman, D.F. Russell, T. Yakusheva, F. Moss, Phys. Rev. E 63 (2001) 031910.
[184] D.F. Russell, A. Tucker, B.A. Wettring, A. Neiman, L. Wilkens, F. Moss, Fluctuation Noise Lett. 2 (2001) L71.
[185] A. Neiman, D.F. Russell, Phys. Rev. Lett. 88 (2002) 138103.
[186] S.K. Han, T.G. Yim, D.E. Postnov, O.V. Sosnovtseva, Phys. Rev. Lett. 83 (1999) 1771.
[187] S. Zhong, H. Xin, J. Phys. Chem. A 105 (2001) 410.
[188] C.S. Zhou, J. Kurths, I.Z. Kiss, J.L. Hudson, Phys. Rev. Lett. 89 (2002) 014101.
[189] K. Miyakawa, H. Isikawa, Phys. Rev. E 65 (2002) 056206.
[190] S. Kádár, J. Wang, K. Showalter, Nature 391 (1998) 770.
[191] J. Wang, S. Kádár, P. Jung, K. Showalter, Phys. Rev. Lett. 82 (1999) 855.
[192] P. Jung, A. Cornell-Bell, K. Madden, F. Moss, J. Neurophysiol. 79 (1998) 1098.
[193] P. Jung, A. Cornell-Bell, F. Moss, S. Kadar, J. Wang J, K. Showalter, Chaos 8 (1998) 567.
[194] I. Sendiña-Nadal, A. Muñuzuri, D. Vives, V. Pérez-Muñuzuri, J. Casademunt, L. Ramírez-Piscina, J.M. Sancho, F. Sagués, Phys. Rev. Lett. 80 (1998) 5437.
[195] M. Löcher, D. Cigna, E.R. Hunt, Phys. Rev. Lett. 80 (1998) 5212.
[196] I. Sendiña-Nadal, S. Alonso, V. Pérez-Muñuzuri, M. Gómez-Gesteira, V. Pérez-Villar, L. Ramírez-Piscina, J. Casademunt, J.M. Sancho, F. Sagués, Phys. Rev. Lett. 84 (2000) 2734.
[197] V. Pérez-Muñuzuri, F. Sagués, J.M. Sancho, Phys. Rev. E 62 (2000) 94.
[198] S. Alonso, I. Sendiña-Nadal, V. Pérez-Muñuzuri, J.M. Sancho, F. Sagués, Phys. Rev. Lett. 87 (2001) 078302.
[199] S. Alonso, F. Sagués, Phys. Rev. E 63 (2001) 046205.
[200] J. Nagumo, S. Arimoto, S. Yoshitzawa, Proc. IRE 50 (1962) 2061.
[201] C. Morris, H. Lecar, Biophys. J. 35 (1981) 193.
[202] A. Hodgkin, J. Physiol. 107 (1948) 165.
[203] B. van der Pol, Phil. Mag. 2 (1928) 978.
[204] K.F. Bonhoefer, J. Gen. Physiol. 32 (1948) 69.
[205] K.F. Bonhoefer, Naturwissenschaft 40 (1953) 301.
[206] A.C. Scott, Rev. Mod. Phys. 47 (1975) 487.
[207] V.A. Vasiliev, Yu.M. Romanovsky, V.A. Yakhno, Physics-Uspekhi 22 (1979) 615.
[208] X. Pei, K. Bachmann, F. Moss, Phys. Lett. A 206 (1995) 61.
[209] A. Longtin, Nuovo Cimento D 17 (1995) 835.
[210] A. Longtin, Chaos 5 (1995) 209.
[211] J.J. Collins, C.C. Chow, Th.T. Imhoff, Nature 376 (1995) 236.
[212] M.H. Chou, Y.T. Lin, Comput. Math. Appl. 32 (1996) 109.
[213] A. Longtin, D.R. Chialvo, Phys. Rev. Lett. 81 (1998) 4012.
[214] M.N. Kuperman, H.S. Wio, G. Izús, R. Deza, Phys. Rev. E 57 (1998) 5122.
[215] H.S. Wio, M.N. Kuperman, F. Castelpoggi, G. Izús, R. Deza, Physica A 257 (1998) 275.
[216] G.G. Izús, R.R. Deza, H.S. Wio, Phys. Rev. E 58 (1998) 93.

[217] D. Barkley, M. Kness, L.S. Tuckerman, Phys. Rev. A 42 (1990) 2489.
[218] J. Rinzel, J.B. Keller, Biophys. J. 13 (1973) 1313.
[219] A.S. Mikhailov, V.I. Krinsky, Physica D 9 (1983) 346.
[220] A. Di Garbo, M. Barbi, S. Chillemi, Int. J. Bifur. Chaos 11 (2001) 2549.
[221] P. Hänggi, H. Thomas, Phys. Rep. 88 (1982) 207.
[222] N.G. van Kampen, Stochastic Processes in Physics and Chemistry, North-Holland, Amsterdam, 1997.
[223] H. Malchow, L. Schimansky-Geier, Noise and Diffusion in Nonequilibrium Bistable Systems, Teubner, Leipzig, 1986.
[224] W. Horsthemke, R. Lefever, Noise Induced Transitions, Theory and Applications in Physics, Chemistry and Biology, Springer, Berlin, 1983.
[225] F. Moss, P.V.E. McClintock (Eds.), Noise in Nonlinear Dynamical Systems, Vol. 1–3, Cambridge University Press, Cambridge, 1989.
[226] P. Jung, P. Hänggi, Adv. in Chem. Phys. 89 (1995) 239.
[227] K. Lekkas, L. Schimansky-Geier, H. Engel-Herbert, Z. Phys. B—Condens. Matter 70 (1988) 517.
[228] L. Schimansky-Geier, F. Moss, G. Schmera, in: W. Ebeling, H. Ulbricht (Eds.), Irreversible Processes and Selforganization, Teubner Verlag, Leipzig, 1989.
[229] M. Kostur, X. Sailer, L. Schimansky-Geier, Fluct. Noise Lett. 3 (2003) L155.
[230] M. Kostur, L. Schimansky-Geier, Phys. Lett. A 265 (2000) 337.
[231] K. Martinez, A. Lin, R. Kharrazian, X. Sailer, H.L. Swinney, Physica D 168 (2002) 1.
[232] B.W. Knight, J. Gen. Physiol. 59 (1972) 734.
[233] H.C. Tuckwell, Introduction to Theoretical Neurobiology, Vol. 2, (Cambridge) Cambridge University Press, Cambridge, 1988.
[234] H.-U. Bauer, K. Pawelzik, Physica D 69 (1993) 380.
[235] P. Lánský, J.P. Rospars, Biol. Cybernet. 72 (1995) 397.
[236] M. Stemmler, Network 7 (1996) 687.
[237] A.R. Bulsara, T.C. Elston, C.R. Doering, S.B. Lowen, K. Lindenberg, Phys. Rev. E 53 (1996) 3958.
[238] R. Rodriguez, P. Lansky, Phys. Rev. E 62 (2000) 8427.
[239] H.E. Plesser, W. Gerstner, Neurocomputing 32/33 (2000) 219.
[240] H.E. Plesser, T. Geisel, Phys. Rev. E 63 (2001) 031916.
[241] T. Shimokawa, K. Pakdaman, S. Sato, Phys. Rev. E 59 (1999) 3427.
[242] T. Shimokawa, A. Rogel, K. Pakdaman, S. Sato, Phys. Rev. E 59 (1999) 3461.
[243] N. Brunel, F.S. Chance, N. Fourcaud, L.F. Abbott, Phys. Rev. Lett. 86 (2001) 2186.
[244] B. Lindner, Coherence and Stochastic Resonance in Nonlinear Dynamical Systems, Logos-Verlag, Berlin, 2002.
[245] N. Fourcaud, N. Brunel, Neural Comput. 14 (2002) 2057.
[246] P.H.E. Tiesinga, Phys. Rev. E 60 (2002) 041913.
[247] M. Barbi, S. Chillemi, A. Di Garbo, Chaos Solitons Fractals 11 (2000) 1849.
[248] P. Lansky, L. Sacerdote, Phys. Lett. A 285 (2001) 132.
[249] L. Sacerdote, P. Lansky, Biosystems 67 (2002) 213.
[250] N. Brunel, S. Sergi, J. Theor. Biol. 195 (1998) 87.
[251] P.E. Latham, B.J. Richmond, P.G. Nelson, S. Nirenberg, J. Neurophysiol. 83 (2000) 808.
[252] J. Feng, D. Brown, Bul. Math. Biol. 62 (2000) 467.
[253] D. Hansel, G. Mato, Phys. Rev. Lett. 86 (2001) 4175.
[254] B. Lindner, A. Longtin, A. Bulsara, Neural Comput. 15 (2003) 1761.
[255] M.J. Chacron, A. Longtin, M. St-Hilaire, L. Maler, Phys. Rev. Lett. 85 (2000) 1576.
[256] G.D. Smith, C.L. Cox, S.W. Sherman, J. Rinzel, J. Neurophysiol. 83 (2000) 588.
[257] E.M. Izhikevich, Neural Networks 14 (2001) 883.
[258] M.J.E. Richardson, N. Brunel, V. Hakim, J. Neurophysiol. 89 (2003) 2538.
[259] J.W. Middleton, M. Chacron, B. Lindner, A. Longtin, Phys. Rev. E 68 (2003) 021920.
[260] B.S. Gutkin, G.B. Ermentrout, Neural Comput. 10 (1998) 1047.
[261] R. Adler, Proc. IRE 34 (1946) 351.
[262] G.B. Ermentrout, Neural Comput. 8 (1996) 979.
[263] B. Lindner, M. Kostur, L. Schimansky-Geier, Fluctuation Noise Lett. 1 (2001) R25.

[264] H. Risken, The Fokker–Planck Equation, Methods of Solution and Applications, 2nd Edition, Springer, Berlin, 1989.
[265] Z. Hou, H. Xin, Phys. Rev. E 60 (1999) 6329.
[266] T. Ditzinger, C.Z. Ning, G. Hu, Phys. Rev. E 50 (1994) 3508.
[267] A. Bulsara, L. Gammaitoni, Phys. Today 49 (1996) 36.
[268] V.S. Anishchenko, A.B. Neiman, F. Moss, L. Schimansky-Geier, Physics-Uspekhi 42 (1999) 7.
[269] D.R. Chialvo, A. Longtin, J. Müller-Gerking, Phys. Rev. E 55 (1997) 1798.
[270] D.R. Cox, Renewal Theory, Methuen, London, 1962.
[271] R.L. Stratonovich, Topics in the Theory of Random Noise, Vol. I, Gordon and Breach, London, 1962.
[272] P. Jung, P. Hänggi, Phys. Rev. A 44 (1991) 8032.
[273] T. Zhou, F. Moss, P. Jung, Phys. Rev. A 42 (1990) 1061.
[274] L. Gammaitoni, F. Marchesoni, S. Santucci, Phys. Rev. Lett. 74 (1995) 1052.
[275] K. Aihara, I. Tokuda, Phys. Rev. E 66 (2002) 026212.
[276] A. Longtin, A. Bulsara, F. Moss, Phys. Rev. Lett. 67 (1991) 656.
[277] B. Shulgin, A. Neiman, V. Anishchenko, Phys. Rev. Lett. 75 (1995) 4157.
[278] A. Neiman, A. Silchenko, V. Anishchenko, L. Schimansky-Geier, Phys. Rev. E 58 (1998) 7118.
[279] J.A. Freund, A. Neiman, L. Schimansky-Geier, Europhys. Lett. 50 (2000) 8.
[280] R. Rozenfeld, J.A. Freund, A. Neiman, L. Schimansky-Geier, Phys. Rev. E 64 (2001) 051107.
[281] B.B. Hu, C.S. Zhou, Phys. Rev. E 63 (2001) 026201.
[282] L. Callenbach L, P. Hänggi, S.J. Linz, J.A. Freund, L. Schimansky-Geier, Phys. Rev. E 65 (2002) 051110.
[283] A.G. Balanov, N.B. Janson, D.E. Postnov, P.V.E. McClintock, Phys. Rev. E 65 (2002) 041105.
[284] A. Neiman, L. Schimansky-Geier, F. Moss, B. Shulgin, J.J. Collins, Phys. Rev. E 60 (1999) 284.
[285] A. Neiman, L. Schimansky-Geier, Phys. Lett. A 197 (1995) 379.
[286] A. Neiman, L. Schimansky-Geier, F. Moss, Phys. Rev. E 56 (1997) R9.
[287] R. Rozenfeld, A. Neiman, L. Schimansky-Geier, Phys. Rev. E 62 (2000) R3031.
[288] C. Heneghan, C.C. Chow, J.J. Collins, T.T. Imhoff, S.B. Lowen, M.C. Teich, Phys. Rev. E 54 (1996) R2228.
[289] A. Neiman, B. Shulgin, V.S. Anishchenko, W. Ebeling, L. Schimansky-Geier, J. Freund, Phys. Rev. Lett. 76 (1996) 4922.
[290] A. Bulsara, A. Zador, Phys. Rev. E 54 (1996) R2185.
[291] G. Deco, B. Schürmann, Phys. Rev. Lett. 79 (1997) 4697.
[292] L. Schimansky-Geier, J. Freund, A. Neiman, B. Shulgin, Int. J. Bifurc. Chaos 8 (1998) 869.
[293] I. Goychuk, P. Hänggi, Phys. Rev. E 61 (2000) 4272.
[294] M.C. Eguia, M.I. Rabinovich, H.D.I. Abarbanel, Phys. Rev. E 62 (2000) 7111.
[295] I. Goychuk, Phys. Rev. E 64 (2001) 021909.
[296] J.W.C. Robinson, J. Rung, A.R. Bulsara, M.E. Inchiosa, Phys. Rev. E 63 (2001) 011107.
[297] R. Steuer, W. Ebeling, D.F. Russell, S. Bahar, A. Neiman, F. Moss, Phys. Rev. E 64 (2001) 061911.
[298] H. Hasegawa, Phys. Rev. E 66 (2002) 021902.
[299] V.I. Melnikov, Phys. Rev. E 48 (1993) 2481.
[300] J. Grasman, Asymptotic Methods for Relaxation Oscillations and Applications, Springer, Berlin, 1989.
[301] H.C. Tuckwell, F.Y.M. Wan, R. Rodriguez, Neurocomputing 48 (2002) 1003.
[302] C.W. Gardiner, Handbook of Stochastic Methods, Springer, Berlin, 1985.
[303] L.F. Abbott, Th.B. Kepler, in: L. Garrido (Ed.), Statistical Mechanics of Neural Networks, Springer, Berlin, 1990, p. 5.
[304] M. Abramowitz, I.A. Stegun, Handbook of Mathematical Functions, Dover, New York, 1970.
[305] L.M. Ricciardi, Diffusion Processes and Related Topics on Biology, Springer, Berlin, 1977.
[306] P. Reimann, C. Van den Broeck, H. Linke, P. Hänggi, M. Rubi, A. Perez-Madrid, Phys. Rev. Lett. 87 (2001) 010602.
[307] D. Dan, A.M. Jayannavar, Phys. Rev. E 66 (2002) 041106.
[308] P. Reimann, C. Van den Broeck, P. Hänggi, H. Linke, J.M. Rubi, A. Pérez-Madrid, Phys. Rev. E 65 (2002) 031104.
[309] B. Lindner, L. Schimansky-Geier, Phys. Rev. Lett. 89 (2002) 230602.
[310] J.W. Shuai, S. Zeng, P. Jung, Fluctuation Noise Lett. 2 (2002) L137.
[311] P.A. Tass, Europhys. Lett. 53 (2001) 15.

[312] P.A. Tass, Europhys. Lett. 57 (2002) 164.
[313] A. Longtin, Chaos, Solitons Fractals 11 (2000) 1835.
[314] P. Jung, P. Hänggi, Phys. Rev. A 41 (1990) 2977.
[315] M. Bethge, G. Silberberg, H. Markram, M. Tsodyks, K. Pawelzik, Proceedings of the Fourth Meeting of the German Neuroscience Society, 2001, p. 249.
[316] Y. Yoshida, S. Imai, Jpn. J. Pharmacol. 74 (1997) 125.
[317] I. Goychuk, P. Hänggi, Proc. Natl. Acad. Sci. USA 99 (2002) 3552.
[318] J.A. White, J.T. Rubinstein, A.R. Kay, Trends Neurosci. 23 (2000) 131.
[319] J.W. Shuai, P. Jung, Phys. Rev. Lett. 88 (2002) 068102.
[320] A. Pikovksy, A. Zaikin, M.A. de la Casa, Phys. Rev. Lett. 88 (2002) 050601.
[321] R. Toral R, C.R. Mirasso, J.D. Gunton, Europhys. Lett. 61 (2003) 162.
[322] A. Zaikin, J. García-Ojalvo, R. Báscones, E. Ullner, J. Kurths, Phys. Rev. Lett. 90 (2003) 030601.
[323] R.F. Fox, Biophys. J. 72 (1997) 2068.
[324] M. Falcke, L. Tsimring, H. Levine, Phys. Rev. E 62 (2000) 2636.
[325] M. Bär, M. Falcke H. Levine, L.S. Tsimring, Phys. Rev. Lett. 84 (2000) 5664.
[326] J.W. Shuai, P. Jung, Phys. Rev. E 67 (2003) 031905.
[327] S. Coombes, Y. Timofeeva, Phys. Rev. E 68 (2003) 021915.
[328] M. Falcke, Biophys. J. 84 (2003) 28.
[329] M. Falcke, Biophys. J. 84 (2003) 42.
[330] J.W. Shuai, P. Jung, Proc. Natl. Acad. Sci. USA 100 (2003) 506.
[331] I. Bezprozvanny, J. Watras, B.E. Ehrlich, Nature 351 (1991) 751.
[332] G.W. De Young, J. Keizer, Proc. Natl. Acad. Sci. USA 89 (1992) 9895.
[333] G.W. De Young, J. Keizer, J. Theor. Biol. 166 (1994) 431.
[334] Y.X. Li, J. Rinzel, J. Theor. Biol. 166 (1994) 461.
[335] J. Watras, I. Bezprozvanny, B.E. Ehrlich, J. Neurosci. 11 (1991) 3239.
[336] J.W. Shuai, P. Jung, Biophys. J. 83 (2002) 87.
[337] M. Marhl, T. Haberichter, M. Brumen, R. Heinrich, Biosystems 57 (2000) 75.
[338] Numeric model parameter: $K_1 = 0.0785$ μM; $K_2 = 1.049$ μM; $K_3 = 0.312$ μM; $K_4 = 0.26393$ μM; $K_5 = 0.0823$ μM; $k_1 = 400.0$ (μM s)$^{-1}$; $k_2 = 0.3$ (μM s)$^{-1}$; $k_3 = 400$ (μM s)$^{-1}$; $k_4 = 0.3$ (μM s)$^{-1}$; $k_5 = 80$ (μM s)$^{-1}$; $r_1 = 0.4$ s^{-1}; $r_2 = 0.02$ s^{-1}; $r_3 = 2.1$ (μM s)$^{-1}$; $K_p = 0.08$ μM; $C_0 = 2.0$ μM; $p = 1.15$ μM; $\alpha = 0.185$.
[339] H. Yoneshima, A. Miyawaki, T. Michikawa, T. Furuichi, K. Mikoshiba, Biochem. J. 322 (1997) 591.
[340] N. Callamaras, J.S. Marchant, X.-P. Sun, I. Parker, J. Physiol. (London) 509 (1998) 81.
[341] N. Callamaras, X.-P. Sun, I. Ivorra, I. Parker, J. Physiol. (London) 511 (1998) 395.
[342] S. Swillens, G. Dupont, L. Combettes, P. Champeil, Proc. Natl. Acad. Sci. USA 96 (1999) 13750.
[343] B. McNamara, K. Wiesenfeld, R. Roy, Phys. Rev. Lett. 60 (1988) 2626.
[344] F. Plaza, M.G. Velarde, F.T. Arecchi, S. Boccaletti, M. Ciofini, Europhys. Lett. 38 (1997) 85.
[345] J.L.A. Dubbeldam, B. Krauskopf, Opt. Commun. 159 (1999) 325.
[346] W. Lu, D. Yu, R.G. Harrison, Phys. Rev. A 58 (1998) R809.
[347] P. Coullet, D. Daboussy, J.R. Tredicce, Phys. Rev. E 58 (1998) 5347.
[348] I. Fischer, G.H.M. van Tartwijk, A.M. Levine, W. Elsäßer, E. Göbel, D. Lenstra, Phys. Rev. Lett. 76 (1996) 220.
[349] G.H.M. van Tartwijk, G.P. Agrawal, Prog. Quantum Electron. 22 (1998) 43.
[350] M. Giudici, C. Green, G. Giacomelli, U. Nespolo, J.R. Tredicce, Phys. Rev. E 55 (1997) 6414.
[351] J. Mulet, C.R. Mirasso, Phys. Rev. E 59 (1999) 5400.
[352] A.M. Levine, G.H.M. van Tartwijk, D. Lenstra, T. Erneux, Phys. Rev. A 52 (1995) R3436.
[353] P. Hänggi, P. Talkner, M. Borkovec, Rev. Mod. Phys. 62 (1990) 251.
[354] T. Sano, Phys. Rev. A 50 (1994) 2719.
[355] J.M. Buldú, J. García-Ojalvo, C.R. Mirasso, M.C. Torrent, Phys. Rev. E 66 (2002) 021106.
[356] A.T. Winfree, J. Theor. Biol. 28 (1970) 327.
[357] Y. Kuramoto, in: H. Araki (Ed.), International Symposium on Mathematica Problems in Theoretical Physics, Lecture Notes in Physics, Vol. 39, Springer, New York, 1975.
[358] S.H. Strogatz, Physica D 143 (2000) 1.
[359] Y. Kuramoto, Chemical Oscillations, Waves and Turbulence, Springer, New York, 1984.

[360] S.K. Han, W.S. Kim, H. Kook, Phys. Rev. E 58 (1998) 2325.
[361] U. Ernst, K. Pawelzik, T. Geisel, Phys. Rev. E 57 (1998) 2150.
[362] P.C. Bressloff, Phys. Rev. E 60 (1999) 2160.
[363] N. Brunel, V. Hakim, Neural Comput. 11 (1999) 1621.
[364] N. Brunel, J. Comput. Neurosci. 8 (2000) 183.
[365] W. Vance, J. Ross, Phys. Rev. E 62 (2000) 3303.
[366] M. Yoshioka, M. Shiino, Phys. Rev. E 61 (2000) 4732.
[367] M. Mattia, P. Del Giudice, Phys. Rev. E 66 (2002) 051917.
[368] H. Hong, M.Y. Choi, Phys. Rev. E 62 (2000) 6462.
[369] L. Rubchinsky, M. Sushchik, Phys. Rev. E 62 (2000) 6440.
[370] W. Gerstner, Neural Comput. 12 (2000) 43.
[371] N. Masuda, K. Aihara, Phys. Rev. E 64 (2001) 051906.
[372] M. Qian, X.-J. Zhang, Phys. Rev. E 65 (2002) 031110.
[373] Y. Shim, H. Hong, M.Y. Choi, Phys. Rev. E 65 (2002) 036114.
[374] H. Sakaguchi, Phys. Rev. E 66 (2002) 056129.
[375] L.G. Morelli, D.H. Zanette, Phys. Rev. E 58 (1998) R8.
[376] W. Gerstner, J.L. van Hemmen, Phys. Rev. Lett. 71 (1993) 312.
[377] W.M. Kistler, R. Seitz, J.L. van Hemmen, Physica D 114 (1998) 273.
[378] P. Jung, G. Mayer-Kress, Chaos 5 (1995) 458.
[379] H. Hempel, T. Fricke, L. Schimansky-Geier, in: J. Parisi, S.C. Müller, W. Zimmermann (Eds.), Nonlinear Physics of Complex Systems, Springer, Berlin, 1996, p. 309.
[380] M. Kostur, L. Schimansky-Geier, Acta Phys. Pol. A 88 (2001).
[381] Z. Hou, H. Xin, Phys. Rev. Lett. 89 (2002) 280601.
[382] P. Jung, P.C. Galey, Ann. Phys. 9 (2000) 697.
[383] B. Naundorf, T. Prager, L. Schimansky-Geier, submitted for publication.
[384] T. Prager, B. Naundorf, L. Schimansky-Geier, Physica A 325 (2003) 176.
[385] A. Nikitin, Z. Néda, T. Vicsek, Phys. Rev. Lett. 87 (2001) 024101.
[386] L. Gómez, R. Budelli, K. Pakdaman, Phys. Rev. E 64 (2001) 061910.
[387] D.J. Watts, S.H. Strogatz, Nature (London) 393 (1998) 440.
[388] K. Sun, Q. Ouyang, Phys. Rev. E 64 (2001) 026111.
[389] D. He, G. Hu, M. Zhan, W. Ren, Z. Gao, Phys. Rev. E 65 (2002) 055204(R).
[390] O. Kwon, H.T. Moon, Phys. Lett. A 298 (2002) 319.
[391] H. Hong, B.J. Kim, M.Y. Choi, Phys. Rev. E 66 (2002) 011107.
[392] Z. Gao, B.B. Hu, G. Hu, Phys. Rev. E 65 (2002) 016209.
[393] M.A. Zaks, A.B. Neiman, S. Feistel, L. Schimansky-Geier, Phys. Rev. E 68 (2003) 066206.
[394] A.S. Pikovsky, in: L. Schimansky-Geier, T. Pöschel (Eds.), Stochastic Dynamics, Lecture Notes on Physics, Vol. 484, Springer, Berlin, 1997, p. 210.
[395] J.A. Acebron, R. Spigler, Physica D 141 (2000) 65.
[396] R. Rodriguez, H.C. Tuckwell, Phys. Rev. E 54 (1996) 5585.
[397] H.C. Tuckwell, R. Rodriguez, J. Comput. Neurosci. 5 (1998) 91.
[398] R. Rodriguez, H.C. Tuckwell, Biosystems 48 (1998) 187.
[399] T. Kanamaru, T. Horita, Y. Okabe, Phys. Rev. E 64 (2001) 031908.
[400] S. Tanabe, K. Pakdaman, Phys. Rev. E 61 (2001) 031911.
[401] A.N. Malakhov, Cumulant Analysis of Random Non-Gaussian Processes, Sov. Radio, Moscow, 1978 (in Russian).
[402] A. Neiman, V.S. Anishchenko, J. Kurths, Phys. Rev. E 49 (1994) 3801.
[403] A. Neiman, U. Feudel, J. Kurths, J. Phys. A: Math. Gen. 28 (1995) 2471.
[404] V.S. Anishchenko, A. Neiman, Int. J. Bifurcation Chaos 2 (1992) 979.
[405] R.C. Desai, R. Zwanzig, J. Stat. Phys. 19 (1978) 1.
[406] A. Pikovsky, S. Ruffo, Phys. Rev. E 59 (1999) 1633.
[407] Y. Kuramoto, I. Nishikawa, J. Stat. Phys. 49 (1987) 569.
[408] I.I. Bonilla, J.M. Casado, M. Morillo, J. Stat. Phys. 48 (1987) 571.
[409] K. Wiesenfeld, P. Hadley, Phys. Rev. Lett. 62 (1989) 1335.

[410] I.I. Bonilla, J.C. Neu, R. Spigler, J. Stat. Phys. 67 (1992) 313.
[411] H. Daido, Phys. Rev. Lett. 73 (1994) 760.
[412] J.D. Crawford, J. Stat Phys. 74 (1994) 1047.
[413] C.J. Perez, F. Ritort, J. Phys. A 30 (1997) 8095.
[414] S.H. Strogatz, R.E. Mirollo, J. Stat. Phys. 63 (1991) 613.
[415] A. Arenas, C. Vicente, Phys. Rev. E 50 (1994) 949.
[416] J.D. Crawford, K.T.R. Davies, Physica D 125 (1999) 1–46.
[417] Z. Kiu, Y.C. Lai, F.C. Hoppenstedt, Phys. Rev. E 63 (2000) 0555201.
[418] J.T. Airaratman, S.H. Strogatz, Phys. Rev. Lett. 86 (2001) 4278.
[419] S. Kim, M.Y. Choi, Phys. Rev. B 48 (1993) 322.
[420] M. Kostur, J. Luczka, L. Schimansky-Geier, Phys. Rev. E 65 (2002) 051115.
[421] P.A. Tass, Phase Resetting in Medicine and Biology-Stochastic Modelling and Data Analysis, Springer, Berlin, 1999.
[422] G. Giacomelli, F. Marin, I. Rabbiosi, Phys. Rev. Lett. 82 (1999) 675.
[423] S. Barbay, G. Giacomelli, F. Marin, Phys. Rev. E 61 (2000) 157.
[424] S. Barbay, G. Giacomelli, F. Marin, Phys. Rev. E 63 (2001) 051110.
[425] P. Reimann, C. Van den Broeck, R. Kawai, Phys. Rev. E 60 (1999) 6402.
[426] S.H. Park, S. Kim, Phys. Rev. E 53 (1996) 3425.
[427] S.H. Park, S. Kim, C.S. Ryu, Phys. Lett. A 225 (1997) 245.
[428] P. Reimann, Phys. Rep. 361 (2002) 57.
[429] P. Reimann, R. Kawai, C. Van den Broeck, P. Hänggi, Europhys. Lett. 45 (1999) 545.
[430] J. Buceta, J.M. Parrondo, C. Van den Broeck, F.J. de la Rubia, Phys. Rev. E 61 (2000) 6287.
[431] S.E. Mangioni, R.R. Deza, H.S. Wio, Phys. Rev. E 63 (2001) 041115.
[432] R. Häussler, R. Bartussek, P. Hänggi, in: J.B. Kadtke, A. Bulsara (Eds.), Applied Nonlinear Dynamics and Stochastic Systems Near the Millennium, AIP Conference Proceedings, Vol. 411, AIP, New York, 1997, p. 243.
[433] A. Pikovsky, M. Rosenblum, J. Kurths, Synchronization: A Universal Concept in Nonlinear Sciences, Cambridge University Press, Cambridge, 2001.
[434] I. Blekhman, Synchronization of Dynamical Systems, Nauka, Moscow, 1971 (in Russian).
[435] I. Blekhman, Synchronization in Science and Technology, Nauka, Moscow, 1981 (in Russian; English translation: ASME Press, New York, 1988).
[436] R. Segev, Y. Shapira, M. Benveniste, E. Ben-Jacob, Phys. Rev. E 64 (2001) 011920.
[437] A. Neiman, X. Pei, D. Russell, W. Wojtenek, L. Wilkens, F. Moss, H. Braun, M. Huber, K. Voigt, Phys. Rev. Lett. 82 (1999) 660.
[438] R.C. Elson, A.I. Selverston, R. Huerta, N.F. Rulkov, M.I. Rabinovich, H.D.I. Abarbanel, Phys. Rev. Lett. 81 (1998) 5692.
[439] A.T. Winfree, J. Theor. Biol. 16 (1988) 15; J. Buck, Q. Rev. Biol. 63 (1988) 265.
[440] W. Singer, Neuron 24 (1999) 49.
[441] R. Ritz, T.J. Sejnowski, Curr. Opin. Neurobiol. 7 (1997) 536.
[442] F. Varela, J.-P. Lachaux, E. Rodriguez, J. Matinerie, Nat. Rev. Neurosci. 2 (2001) 229.
[443] C. Fohlmeister, R. Ritz, W. Gerstner, J.L. van Hemmen, Neural Comput. 7 (1995) 905.
[444] W. Gerstner, Phys. Rev. E 51 (1995) 738.
[445] W.-J. Rappel, A. Karma, Phys. Rev. Lett. 77 (1996) 3256.
[446] J. Garcia-Ojalvo, L. Schimansky-Geier, Europhys. Lett. 47 (1999) 298.
[447] C.S. Zhou, J. Kurths, B. Hu, Phys. Rev. Lett. 87 (2001) 098101.
[448] A. Andronov, A. Vitt, S. Khaykin, Theory of Oscillations, Pergamon Press, Oxford, 1966.
[449] C. Hayashi, Nonlinear Oscillations in Physical Systems, McGraw-Hill, New York, 1964.
[450] R.L. Stratonovich, Topics in the Theory of Random Noise, Vol. II, Gordon and Breach, London, 1967.
[451] A.N. Malakhov, Fluctuations in Auto-oscillation Systems, Nauka, Moscow, 1968 (in Russian).
[452] L. Schimansky-Geier, V. Anishchenko, A. Neiman, in: S. Gielen, F. Moss (Eds.), Neuro-informatics, Handbook of Biological Physics, Vol. 4, Elsevier, Amsterdam, 2001, p. 23.
[453] M. Rosenblum, A. Pikovsky, J. Kurths, C. Schäfer, P.A. Tass, in: S. Gielen, F. Moss (Eds.), Neuro-informatics, Handbook of Biological Physics, Vol. 4, Elsevier, Amsterdam, 2001, p. 279.

[454] P.A. Tass, M. Rosenblum, J. Weule, J. Kurths, A. Pikovsky, J. Volkmann, A. Schnitzler, H. Freund, Phys. Rev. Lett. 81 (1998) 3291.
[455] E. Ullner, A. Zaikin, J. García-Ojalvo, J. Kurths, Phys. Rev. Lett. (2003).
[456] S. Alonso, F. Sagués, J.M. Sancho, Phys. Rev. E 65 (2002) 066107.
[457] A.S. Mikhailov, Phys. Lett. A 73 (1979) 143.
[458] A.S. Mikhailov, Z. Phys. B: Condens. Matter 41 (1981) 277.
[459] J. García-Ojalvo, J.M. Sancho, L. Ramirez-Piscina, Phys. Lett. A 168 (1992) 35.
[460] J. García-Ojalvo, A. Hernández-Machado, J.M. Sancho, Phys. Rev. Lett. 71 (1993) 1542.
[461] C. Van den Broeck, J.M.R. Parrondo, J. Amero, A. Hernández-Machado, Phys. Rev. E 49 (1994) 2639.
[462] C. Van den Broeck, J.M.R. Parrondo, R. Toral, Phys. Rev. Lett. 73 (1994) 3395.
[463] A. Becker, L. Kramer, Phys. Rev. Lett. 73 (1994) 955.
[464] A.A. Zaikin, L. Schimansky-Geier, Phys. Rev. E 58 (1998) 4355.
[465] R. Kawai, X. Sailer, L. Schimansky-Geier, SPIE Proc. 5114 (2003) 173.
[466] N.G. van Kampen, IBM J. Res. Dev. 32 (1988) 107.
[467] R. Landauer, J. Stat. Phys. 53 (1988) 233.
[468] C. van den Broeck, in: L. Schimansky-Geier, T. Pöschel (Eds.), Stochastic Dynamics, Lecture Notes on Physics, Vol. 484, Springer, Berlin, 1997, p. 7.
[469] Recently a mechanism leading to noise-induced phase transition has been reported that does not require a Stratonovich shift, see for instance, M. Ibañes, J. García-Ojalvo, R. Toral, J.M. Sancho, Phys. Rev. Lett. 87 (2001) 020601.
[470] R. Müller, K. Lippert, A. Kühnel, U. Behn, Phys. Rev. E 56 (1997) 2658.
[471] A. Zaikin, J. Kurths, L. Schimansky-Geier, Phys. Rev. Lett. 85 (2000) 227.
[472] A. Zaikin, J. García-Ojalvo, L. Schimansky-Geier, J. Kurths, Phys. Rev. Lett. 88 (2002) 010601.
[473] A.T. Winfree, Chaos 1 (1991) 303.
[474] See, for instance, the focus issue on; Fibrillation in Normal Ventricular Myocardium, Chaos 8 (1998) 1.
[475] J.J. Taboada, A.P. Muñuzuri, V. Pérez-Muñuzuri, M. Gómez-Gesteira, V. Pérez-Villar, Chaos 4 (1994) 519.
[476] M. Markus, G. Kloss, I. Kusch, Nature 371 (1994) 402.
[477] Z. Nagy-Ungvarai, S. Müller, Int. J. Bifurc. Chaos 4 (1994) 1257.
[478] Q. Ouyang, J.-M. Flesselles, Nature 379 (1996) 143.
[479] M. Hildebrand, M. Bär, M. Eiswirth, Phys. Rev. Lett. 75 (1995) 1503.
[480] M.C. Strain, H.S. Greenside, Phys. Rev. Lett. 80 (1998) 2306.
[481] M. Bär, M. Eiswirth, Phys. Rev. E 48 (1993) 1635.
[482] M. Bär, M. Or-Guil, Phys. Rev. Lett. 82 (1999) 1160.
[483] A.V. Panfilov, P. Hogeweg, Phys. Lett. A 176 (1993) 295.
[484] A.F.M. Marée, A.V. Panfilov, Phys. Rev. Lett. 78 (1997) 1819.
[485] V.N. Biktashev, A.V. Holden, M.A. Tsyganov, J. Brindley, N.A. Hill, Phys. Rev. Lett. 81 (1998) 2815.
[486] D. Barkley, Physica D 49 (1991) 61.
[487] P. Jung, Phys. Rev. Lett. 78 (1997) 1723.
[488] Y. Zhang, G. Hu, L. Gammaitoni, Phys. Rev. E 58 (1998) 2952.
[489] J.F. Lindner, S. Chandramouli, A.R. Bulsara, M. Löcher, W.L. Ditto, Phys. Rev. Lett. 81 (1998) 5048.
[490] J. García-Ojalvo, A.M. Lacasta, F. Sagués, J.M. Sancho, Europhys. Lett. 50 (2000) 427.
[491] S.W. Hughes, D.W. Cope, T.I. Tóth, S.R. Williams, V. Crunelli, J. Physiol. 517 (1999) 805.
[492] P. Heyward, M. Ennis, A. Keller, M.T. Shipley, J. Neurosci. 21 (2001) 5311.
[493] J. García-Ojalvo, L. Schimansky-Geier, J. Stat. Phys. 101 (2000) 473.
[494] J. García-Ojalvo, F. Sagués, J.M. Sancho, L. Schimansky-Geier, Phys. Rev. E 65 (2002) 011105.
[495] J. Armero, J.M. Sancho, J. Casademunt, A.M. Lacasta, L. Ramírez-Piscina, F. Sagués, Phys. Rev. Lett. 76 (1996) 3045.
[496] R.N. Madan, Chua's Circuit: A Paradigm for Chaos, World Scientific, Singapore, 1993.
[497] R. Báscones, J. García-Ojalvo, J.M. Sancho, Phys. Rev. E 65 (2002) 061108.